FACULTY OF MECHATRONICS,
INFORMATICS AND INTERDISCIPLINARY
STUDIES TUL



Dissertation

Development of Techniques for a Straight-Line Alignment System Based on Pseudo-Nondiffracting Structured and Layer Laser Beams

Study program: P0788D270007 – Applied Sciences in Engineering
Author: **Ing. Martin Dušek**
Supervisor: doc. RNDr. Miroslav Šulc, Ph.D.
CERN Supervisor: Jean-Christophe Gayde

Liberec 2025

Declaration

I hereby certify, I, myself, have written my dissertation as an original and primary work using the literature listed below and consulting it with my thesis supervisor and my thesis counsellor.
I acknowledge that my dissertation is fully governed by Act No. 121/2000 Coll., the Copyright Act, in particular Article 60 – School Work.
I acknowledge that the Technical University of Liberec does not infringe my copyrights by using my dissertation for internal purposes of the Technical University of Liberec.
I am aware of my obligation to inform the Technical University of Liberec on having used or granted license to use the results of my dissertation; in such a case the Technical University of Liberec may require reimbursement of the costs incurred for creating the result up to their actual amount.
At the same time, I honestly declare that the text of the printed version of my dissertation is identical with the text of the electronic version uploaded into the IS STAG.
I acknowledge that the Technical University of Liberec will make my dissertation public in accordance with paragraph 47b of Act No. 111/1998 Coll., on Higher Education Institutions and on Amendment to Other Acts (the Higher Education Act), as amended.
I am aware of the consequences which may under the Higher Education Act result from a breach of this declaration.

19. 1. 2026 Ing. Martin Dušek

Development of Techniques for a Straight-Line Alignment System Based on Pseudo-Nondiffracting Structured and Layer Laser Beams

Abstract

This thesis develops solutions based on pseudo-nondiffracting Structured Laser Beams (SLBs) and Layer Beams (LBs) for alignment systems based on a straight-line reference. The thesis is organized into a theoretical part, followed by six thematically interconnected publications. The first publication describes the generating wavefront reconstruction method using a convolutional neural network and least-squares fitting to estimate defocus and spherical aberrations from a single transversal intensity distribution, which achieved the root-mean-square error (RMSE) of the reconstruction 0.09λ relative to Shack–Hartmann sensor measurements. The second publication investigates how atmospheric effects influence the quality of the alignment reference. The third publication builds on this work by presenting, together with the second, an analysis of centroiding algorithms applied to SLBs and Hollow SLBs. On simulated datasets, the algorithms introduced absolute detection errors in the range of 10^{-4} pixel (px) to 10^{-2} px, while the experimental validation of precision demonstrated a standard deviation of 1.3 µm. The fourth publication describes experimental generation of LBs up to 140 m and presents an algorithm for alignment reference plane detection, which introduced a standard deviation error equal to 0.7 µm for the experimental validation of precision. The fifth publication describes the generation principle of LBs in detail. The last publication presents an LB-based alignment system prototype, comparing it to state-of-the-art measurements. The results showed a repeatability and reproducibility of the alignment reference with an RMSE below 30.0 µm. The relative alignment precision was validated as 4.3 µm over a 2 m distance. The last paper also describes a conceptual idea for a fiber matrix-based radiation-hard sensor. The proof-of-concept yielded a root mean squared error of the detection of the reference below 1.3 µm. This error was induced by the fiber matrix. The results highlight the potential for using straight-line reference systems based on SLBs and LBs for the alignment of particle accelerators at CERN.

Keywords: Non-Diffracting Beams, Structured Laser Beams, Layer Beams, Alignment

Vývoj technik pro justážní systém na bázi Strukturovaných a Vrstvených laserových svazků

Abstrakt

Tato disertační práce rozvíjí a experimentálně ověřuje metody využívající pseudo-nedifrakční Strukturované laserové svazky (Structured Laser Beams, SLBs) a Vrstvené svazky (Layer Beams, LBs) pro justážní systémy založené na referenční linii. Práce je členěna na teoretickou část, po které následuje šest tématicky propojených publikací. První publikace popisuje metodu rekonstrukce generující vlnoplochy pomocí konvoluční neuronové sítě a metody nejmenších čtverců pro odhad defokusu a sférických aberací z jediného příčného rozložení intenzity. Výsledná kvadratická střední chyba (RMSE) rekonstrukce byla 0,09λ vzhledem k měřením Shack–Hartmannovým senzorem. Druhá publikace popisuje vliv atmosféry na kvalitu justážní reference a společně se třetí publikací se také zabývá algoritmy pro detekci středu SLBs a Hollow SLBs. Ty dosáhly absolutních chyb v rozsahu 10^{-4} pixelu (px) až 10^{-2} px na simulovaných datech, a směrodatné odchylky 1,3 µm při experimentálním ověření přesnosti. Čtvrtá publikace popisuje experiment šíření LBs na vzdálenost až 140 m a také předsavuje algoritmus pro detekci referenční roviny pro justáž, který dosáhl směrodatné odchylky chyby 0,7 µm při experimentální validaci přesnosti. Pátá publikace pak detailně popisuje princip generování LBs. Poslední publikace představuje prototyp justážního systému založeného na LBs. Tento systém byl porovnán se state-of-the-art měřeními a dosáhl opakovatelnosti a reprodukovatelnosti při tvorbě referenční roviny s kvadratickou střední chybou pod 30,0 µm. Relativní přesnost justáže byla experimentálně ověřena s přesností 4,3 µm na vzdálenosti 2 m. Dále je v článku popsán koncept senzoru odolného vůči radiaci založeného na matrici optických vláken. Ověření konceptu vedlo ke kvadratické střední chybě detekce referenční roviny menší než 1,3 µm. Tuto chybu způsobilo vložení vláknové matrice. Výsledky této práce podtrhují potenciál využití SLBs a LBs pro justážní systémy určené pro urychlovače částic v laboratoři CERN.

Klíčová slova: Nedifrakční svazky, Strukturované svazky, Vrstvené svazky, Justáž

Acknowledgements

I would like to express my deep gratitude to my supervisors, Miroslav Šulc and Jean-Christophe Gayde, for guiding my direction and for the opportunity to work on such an interesting topic. I am also really thankful to Kryštof Polák, Sebastian Figura, Witold Niewiem, Jakub Michal Polak, Solomon William Kamugasa, Eva Roiková, Dirk Mergelkuhl, and Štěpán Kunc. The same goes for the other members of the teams that I was part of, both at CERN and at the Technical University of Liberec. Thank you for all the valuable advice you gave me during my research, and also for the good company. Additionally, I would like to express my gratitude to the institutions CERN, the Ministry of Education, Youth and Sports of the Czech Republic, and the Technical University of Liberec for providing the funding and conditions that allowed me to conduct my research.

I would also like to thank my girlfriend, family, and friends for their support throughout my PhD. Whether things were going well or not, I have always been able to rely on you. Your encouragement and understanding, when I was stressed chasing deadlines, have made a real difference for me. I appreciate everything you have done for me. I am grateful for having you in my life. Thank You! Díky!

Contents

List of Abbreviations . . . 8

1 Introduction **14**
1.1 Motivation and Aims . . . 15

2 Thesis Outline **17**

3 Particle Accelerator Alignment **19**
3.1 Introduction to Geodetic Metrology for Particle Accelerator Alignment 19
3.1.1 Coordinate Reference Systems and Frames . . . 19
3.1.2 Absolute and Relative Accelerator Alignment . . . 21
3.1.3 Fiducialization . . . 22
3.1.4 Software . . . 22
3.2 State-of-the-Art Metrology Methods and Tools . . . 22
3.2.1 Coordinate Measuring Machines . . . 23
3.2.2 Inclinometers . . . 23
3.2.3 Laser Trackers . . . 23
3.2.4 Straight-Line Reference Systems . . . 24

4 Foundations of Electromagnetic, Scalar and Ray Optics **27**
4.1 Maxwell Equations . . . 27
4.1.1 Gauss's Laws . . . 27
4.1.2 Faraday's Law . . . 28
4.1.3 Ampère-Maxwell's Law . . . 28
4.1.4 Differential Form of Maxwell's Equations . . . 28
4.2 Wave and Helmholtz Equations . . . 29
4.2.1 Wave Equation . . . 29
4.2.2 Helmholtz Equation . . . 29
4.2.3 Paraxial Helmholtz Equation . . . 30
4.3 Polarization of Electromagnetic Waves . . . 30
4.4 Scalar Diffraction Theory . . . 31
4.4.1 Fourier Optics . . . 31
4.4.2 Diffraction Integral . . . 32
4.5 Ray optics . . . 33
4.5.1 Eikonal Equation . . . 34
4.5.2 Snell's Law . . . 34

5 Introduction to Optical Beams **36**
5.1 Gaussian Beams . . . 36
5.2 Non-Diffracting Beams . . . 37
5.2.1 Airy Beams . . . 38
5.2.2 Bessel Beams . . . 39
5.2.3 Pin Beams . . . 40

6 Structured Laser Beams and Layer Beams **41**
6.1 Generating Principle and Beam Properties . . . 41
6.2 Numerical Modeling . . . 45
6.3 Structured Laser Beams and Layer Beams in the Context of Alignment 46

7 Collection of Papers **49**
7.1 Wavefront Reconstruction of a Non-Diffracting Structured Laser Beam 50
7.2 Detection of Structured Laser Beam Centroid and Its Use For Alignment . . . 63
7.3 Analysis of Centroiding Algorithms for Non-Diffracting Structured and Hollow Structured Laser Beams . . . 69
7.4 Generation of Symmetrical Optical Caustic Beams for Precise Alignment . . . 83
7.5 Generation of Pseudo-Nondiffracting Symmetrical Layer Beams Using Cylindrical Lenses . . . 88
7.6 First Steps Toward the Development of a Straight-Line Reference Alignment System for Future Accelerators at CERN Using Pseudo-Nondiffracting Layer Beams . . . 104

8 Conclusion **119**

Bibliography **122**

List of Author's Publications **134**

List of Abbreviations

$a(x, y, z)$	Scalar optical field
a	Aperture radius
$a(\bar{x}, \bar{y})$	Complex field amplitude at aperture plane coordinates
$Ai(x)$	Airy function
A	Aperture surface
b	Control parameter (catastrophe theory)
$\mathbf{B}$	Magnetic field vector
b_j	Control parameters (catastrophe theory)
c	Speed of light in vacuum
$C_n(b)$	Diffraction catastrophe integral of order n
$C_3(b)$	Airy integral (fold catastrophe, $n = 3$)
E_x, E_y	Cartesian electric-field components
$\mathbf{E}_0$	Electric field amplitude vector
F_n	Fresnel number
f_x, f_y	Spatial frequency coordinates
G_0, S_0	Complex field amplitude
$\mathbf{J}$	Current density vector
J_0	Zeroth-order Bessel function
$K(\chi)$	Inclination factor
K_1	Defocus aberration coefficient
K_{m+1}	Higher-order spherical aberration coefficients
k	Scalar wavenumber
$\mathbf{k}$	Wavevector
k_T	Transverse wavevector component
k_z	Longitudinal wavevector component
L_{PL}	Distance between facing surfaces of Phase lens and Projection lens
L_{PLMIN}, L_{PLMAX}	Values defining the interval of L_{PL} distances
L_{Ph}	Phase-lens to Fourier-plane distance
$d\mathbf{l}$	Differential path length
M	Matrix size
n_1, n_2	Refractive indices of two media

O	Point spherical wave source in front of the aperture
P	Observation point behind the aperture
$P_n(b, s)$	Potential function (Catastrophe theory)
Q	Electric charge
R	Aperture point on the original wavefront
$R(z)$	Radius of wavefront curvature
R^2	Coefficient of determination
r	Radial cylindrical coordinate
r_0	Distance from point O to R
r_1	Distance from point R to P
$\mathbf{r}$	Position vector
$S(x, y, z)$	Eikonal function
$\mathbf{S}$	Area vector
S_c	Template size (pixels)
s	State variable (catastrophe theory)
t	Thresholding parameter
$u(x, y, z)$	Paraxial Helmholtz equation solution
$U(x, y, z)$	Slowly varying envelope
U_0	Field amplitude in Gaussian beam equation
$U(R)$	Complex field at the point R
$V(P)$	Complex field at the observation point P
$V(x, y, z)$	Complex field in three spatial dimensions
V_0	Field amplitude in Bessel beam equation
$v(r, \alpha, z)$	Cylindrical scalar field
$W(x, y), W(r, \alpha)$	Generating wavefront
$w(z)$	Gaussian beam radius at z
w_0	Minimum Gaussian beam waist
x, y	Spatial coordinates
x_0, y_0	Coordinates in the initial plane behind projection lens
z_0	Rayleigh range parameter in Gouy phase
z_R	Rayleigh length
Δk	Frequency-domain sampling step
Δx	Spatial sampling step
$\mathcal{A}(f_x, f_y)$	Fourier transform of the aperture plane complex field
$\mathcal{E}_1$	Incident plane wave

$\mathcal{E}_1'$	Reflected plane wave
$\mathcal{E}_2$	Refracted plane wave
$\mathcal{H}(f_x, f_y, z)$	Free-space transfer function
$\mathcal{FT}\{\cdot\}$	Fourier transform operator
∇_T^2	Transverse Laplacian
α	Azimuthal angle
β_1, β_2	Angles of incidence and refraction
δ	Phase difference between the transverse electric field components
ε_0	Vacuum permittivity
λ	Wavelength
n	Refractive index
$\hat{\mathbf{n}}$	Unit surface normal
μ_0	Vacuum permeability
ω	Angular frequency
Φ	Phase
ρ	Charge density
θ	Gaussian beam divergence
θ_0	Plane wave angle to propagation axis (Bessel beam)
$\zeta(z)$	Gouy phase
φ	Phase constant

AiB	Airy Beam
APS	Advanced Photon Source
BB	Bessel Beam
CAB	Circular Airy Beam
CCD	Charge-Coupled Device
CERN	European Organization for Nuclear Research
CLIC	Compact Linear Collider
CMM	Coordinate Measuring Machine
CMOS	Complementary Metal-Oxide-Semiconductor
CRF	Coordinate Reference Frame
CRS	Coordinate Reference System
CSNS	China Spallation Neutron Source
CSS	CERN Coordinate System

DAB	Dual Airy Beam
DESY	Deutsches Elektronen-Synchrotron
FCC	Future Circular Collider
FFT	Fast Fourier Transformation
FSI	Frequency-Scanning Interferometry
FT	Fourier Transform
GB	Gaussian Beam
HL-LHC	High-Luminosity LHC
HLS	Hydrostatic Leveling System
HSLB	Hollow Structured Laser Beam
KEK	Japanese High-Energy Accelerator Research Organization
LB	Layer Beam
LGC2	Logiciel Général de Compensation
LHC	Large Hadron Collider
PB	Pin Beam
PS	Proton Synchrotron
px	Pixel
RMSE	Root Mean Square Error
SAB	Symmetric Airy Beam
SLAC	Stanford Linear Accelerator Center
SLB	Structured Laser Beam
SLM	Spatial Light Modulator
SPS	Super Proton Synchrotron
WPS	Wire Positioning System

Paper 7.1

c_j	j-th Zernike coefficient
G_0, S_0	Complex field amplitude
$g(x_0, y_0, 0)$	Complex field with additional SLB aberrations
L_{PLMIN}, L_{PLMAX}	Values defining the interval of L_{PL} distances
S	Sum in least-squares minimization
$s(x_0, y_0, 0)$	Complex field of non-aberrated SLB
$U(x, y, z)$	Reconstructed complex field at distance z
x_0, y_0	Coordinates in initial plane behind projection lens
Z_j	j-th Zernike polynomial

AI	Artificial Intelligence
CNN	Convolutional Neural Network
MSE	Mean Squared Error
PV	Peak-to-Valley
$\mathbf{RMSE_{wf}}$	Wavefront RMSE
SHS	Shack-Hartmann Sensor

Paper 7.2

γ	Gamma parameter
t	Thresholding parameter
$I(x, y)$	Pixel intensity
$I_{\mathbf{max}}$	Maximum pixel intensity
$\bar{x}, \bar{y}$	Centroid coordinates
AC	Air Conditioning
AE	Absolute Error
BFA	Best-Fit Algorithm
CoG	Center-of-Gravity
GCoG	Gamma-Corrected CoG Algorithm
ROI	Region of Interest (pixels)
SNR	Signal-to-Noise Ratio
STDe	Standard Deviation of Error
STDp	Standard Deviation of Position
TCoG	Threshold CoG Algorithm

Paper 7.3

$C(u, v)$	Normalized 2-D correlation function
$G_{corr}(x, y)$	Gamma-corrected intensity
$g_t(x, y)$	Gaussian template function (erratum)
$I_{u,v}$	Mean intensity in region under template
p_1, p_2	Linear-fit coefficients
$p_{\mathbf{lines}}$	Number of polarization lines fitted
R^2	Coefficient of determination
S_c	Template size (pixels)
S_0, S_1, S_2, S_3	Stokes parameters
$T(x, y)$	Thresholding function

$t(x, y)$	Gaussian template function (original paper)
$\bar{t}$	Mean of template intensity
u, v	Correlation coordinates
$\mathrm{var}_{\mathrm{noise}}$	Gaussian noise variance
$x_{\max}, y_{\max}$	Array limits in CoG sums
ψ	Polarization ellipse angle
CORR	Correlation Template Matching Algorithm
MAE	Mean Absolute Error
POL	Polarization-Based Centroid Algorithm
STD$_\mathbf{c}$	Gaussian-Template Width
WCoG	Weighted CoG Algorithm

Paper 7.4

F_{PL}	Projection-lens focal length
OCB	Optical Caustic Beams
PhL	Phase Lens
PL	Projection Lens

Paper 7.5

L_{Ph}	Phase-lens to Fourier-plane distance

Paper 7.6

I_{max}	Maximum pixel intensity of the normalized grayscale image
σ	Standard deviation of the Gaussian noise
PSNR	Peak Signal-to-Noise Ratio
USMN	Unified Spatial Metrology Network

1 Introduction

Particle accelerators are complex machines designed to accelerate confined beams of particles to velocities close to the speed of light. The alignment of hardware components of the accelerator is defined as the process of adjusting the position of accelerator parts to their defined position. It is a critical aspect of particle accelerator operation, directly impacting the performance, efficiency, and ultimately the scientific output of these machines [1]. To achieve the desired precision in particle trajectories using the beam-based alignment methods [2], the components of the accelerator must be first aligned with millimeter to sub-millimeter accuracy over distances that can span kilometers. This step, which is sometimes referred to as a pre-alignment, relies fundamentally on geodetic metrology and advanced surveying techniques [3].

The Large Hadron Collider (LHC) [4] at the European Council for Nuclear Research (CERN) [5] is a perfect example of the challenges and achievements of the accelerator alignment field. With a circumference of 27 km, the LHC requires the absolute alignment and placement of accelerator components with accuracy on the order of millimeters. The relative alignment of LHC components must ensure that their positions deviate no more than 0.15 mm (1-sigma) from the alignment reference within any 150 m long segment, to maintain beam stability and achieve collision energies at the TeV scale [6]. These requirements represent a significant tightening of alignment tolerances compared to earlier accelerators at CERN, such as the Proton Synchrotron (PS) and the Super Proton Synchrotron (SPS) [7]. The relative alignment precision in the PS and SPS was typically on the order of several hundred micrometers to about 1 mm over similar segment lengths [8].

This reflects the increasing demands on alignment tolerances as accelerator energies and complexities grow. These tolerances were allowed to be met by the evolution of modern techniques in geodetic metrology, which leverage advances in various fields such as geodesy, surveying, metrology, optics, and computational modeling, complementing traditional surveying methods like theodolite observations with advanced instruments such as laser trackers and photogrammetry [3]. An additional complementary measurement technique is a straight-line reference system. It is used to measure the offsets of individually aligned components relative to a common reference line over distances of hundreds of meters. The straight-line reference systems are a vital measurement technique in the accelerator alignment field, because the accuracy of angular measurement devices, such as laser trackers, decreases with distance and does not provide the required precision for measurements spanning hundreds of meters [9].

1.1 Motivation and Aims

The continuous advancement of particle physics relies heavily on the development of increasingly powerful and precise particle accelerators like the Future Circular Collider (FCC) with its 100 km circumference [10], and Compact Linear Collider (CLIC) [11]. These next-generation machines could require alignment tolerances that can be even orders of magnitude tighter than LHC [1, 12]. Automation in particle accelerator alignment systems is also becoming increasingly crucial for maintaining precise component positioning in high-radiation environments, increasing efficiency, enabling real-time adjustments without human intervention, and improving overall safety [13]. To address these challenges, the R&D initiatives in the alignment domain at CERN include, for example:

- **Frequency Scanning Interferometry (FSI):** Development of high-precision distance measurement systems based on absolute interferometry for continuous monitoring of particle accelerator component positions [14] and monitoring of machine detector interfaces [15].
- **Full Remote Alignment System:** Integration of various alignment technologies into a comprehensive system for real-time monitoring and adjustment of particle accelerator components [13, 14, 16, 17].
- **Wire Positioning System:** A Wire Positioning System (WPS) is a straight-line alignment system that measures radial and vertical offsets of particle accelerator components relative to a stretched reference wire. The research focuses on the improvement of WPS capacitive sensors for improved accuracy and reliability in harsh radiation environments and solutions for wire installation automation [16].
- **Hydrostatic Leveling System:** A Hydrostatic Leveling System (HLS) is a measurement system that determines height differences between points by measuring their position with respect to the water level. This provides precise vertical alignment linked to a reference given by gravity. Development is focused on next-generation interferometric HLS sensors [16].

Maintaining the same level of performance of the straight line reference systems, such as the WPS, while extending the length of the reference line, poses a substantial challenge. Put simply, there is an increased risk of cumulative errors and mechanical limitations, making the development of scalable, high-precision reference systems a critical research focus. The detailed limitations of different types of straight-line reference systems are discussed in detail in the following chapters.

In recent years, nondiffracting optical beams have gained attention and been explored as tools in various applications due to their unique properties, including self-regeneration after encountering an obstacle [18], or the ability to propagate along curved trajectories [19]. They also exhibit increased robustness against diffraction compared to well-known Gaussian beams (GBs) [20]. The low divergence could

make the use of pseudo-nondiffracting optical beams a viable option for straight-line reference systems, as the beams could propagate over long distances without significantly increasing in size. This would mean that the vital part of the beam can fit easily on a CMOS or CCD chip, which is used for the detection of the alignment reference line given by the laser.

This dissertation thesis focuses on the development and implementation of pseudo-nondiffracting beam technology, namely Structured laser beams (SLBs) and Layer beams (LBs), for particle accelerator alignment. The thesis aims to bridge the gap between research advancements in the field of non-diffracting beams, also known as caustic beams or structured light [21–25], and their practical application in particle accelerator alignment or in other facilities requiring similar alignment requirements. The work is motivated by the need to address current limitations of the straight-line alignment systems and to explore the potential use of structured light in particle accelerator environments.

The presented research builds on existing frameworks while introducing novel theoretical investigations and experimental implementations. The main focus is on beam generation, characterization, and practical application in straight-line reference systems in order to produce beams with tailored intensity profiles and propagation characteristics, enabling precise control over their use as an alignment reference.

The results of this research aim to explore and demonstrate the feasibility of using pseudo-nondiffracting beams for particle accelerator alignment and provide tools that could help in the future development of alignment systems. They should provide a foundation for future developments in high-precision metrology and contribute to the development of a new class of alignment tools.

2 Thesis Outline

The theoretical part of this thesis is dedicated to providing a comprehensive foundation in the theory of accelerator alignment and optics to facilitate the reader's understanding of the research topic by systematically introducing the principles, terminology, and limitations of the related technologies. It also connects the information presented in the publications within the context of the research as a whole.

The results are presented in a series of thematically interconnected papers, each published in peer-reviewed journals or in proceedings of international conferences:

- The first paper investigates generating wavefront measurement techniques for SLBs, based on a single transversal intensity distribution. This technique can be employed in challenging measurement conditions where traditional wavefront sensors can be challenging to use.
- The second conference paper discusses problems caused by the refractive index gradient and fluctuations in the propagation medium. Additionally, it presents the first experimental and simulation results of the development of detection methods of the alignment reference coordinates given by SLBs.
- The third paper further deepens the analysis of the developed detection methods of the alignment reference coordinates given by SLBs and Hollow SLBs. The results are presented on simulated data.
- The fourth conference paper presents the basic principle behind the generation of LBs. Additionally, it shows simulated and experimental data of LBs propagating over 140 m. The means of precisely detecting the alignment reference plane are presented on experimental data.
- The fifth paper explores the optimization of LB's parameters, such as propagation distance and beam size. This work demonstrates how these beams can be tailored to meet the specific demands of accelerator alignment, offering greater flexibility and understanding of the beam generation principle.
- The sixth paper presents practical alignment experiments using LBs, including the development and optimization of specialized sensors and a comparison with state-of-the-art alignment methods.

By addressing detection, characterization, optimization, and application, these publications collectively establish a robust foundation for the use of SLBs and LBs

in accelerator alignment. They also present and discuss the challenges that need to be addressed for the successful development of a future alignment system.

3 Particle Accelerator Alignment

3.1 Introduction to Geodetic Metrology for Particle Accelerator Alignment

The Earth's crust is in constant, uneven motion, which directly impacts the alignment stability of CERN's accelerator infrastructure. Variations in ground stability are particularly evident in certain areas of the 27 km long LHC tunnel, where an annual vertical displacement of up to 1.5 mm is observed. Beyond geological factors, mechanical forces, such as those arising from vacuum-induced stresses, and temperature change, can contribute to component misalignment. These factors can cause misalignment over time and lead to degradation in the accelerator's performance.

Geodetic metrology, integrating disciplines like geodesy, surveying, optics, and mechatronics, plays a crucial role in the accelerator alignment field, guaranteeing the geometrical accuracy of all accelerator components during all project stages. During the project design part, a clear alignment strategy is defined with absolute and relative alignment requirements, error budgets, and the instrumentation and tools that will be used in achieving these goals. After this, regular monitoring and maintenance, including re-measurement and re-alignment during technical stops of the accelerator, are essential to preserve the required geometry of the accelerator components. These components are aligned in six degrees of freedom: translational adjustments along the longitudinal, vertical, and horizontal axes, and rotational corrections for pitch, yaw, and roll [3].

In the following chapter, terminology, concepts, and techniques used to achieve all of the aforementioned are presented. The reader should get the basic knowledge of the accelerator alignment workflow, facilitating the understanding in the broader context. Terms, directly connected to the thesis, are presented in greater detail. Note that for definitions of terms connected specifically to metrology, such as accuracy, precision, repeatability, or reproducibility, please refer to publications "ISO Guide to the Expression of Uncertainty in Measurement" [26] or "International Vocabulary of Metrology – Basic and General Concepts and Associated Terms" [27].

3.1.1 Coordinate Reference Systems and Frames

A Coordinate Reference System (CRS) is the conceptual framework used to assign spatial coordinates to points in specific locations. It is defined by a set of rules that describe how coordinates are measured and expressed, including the choice

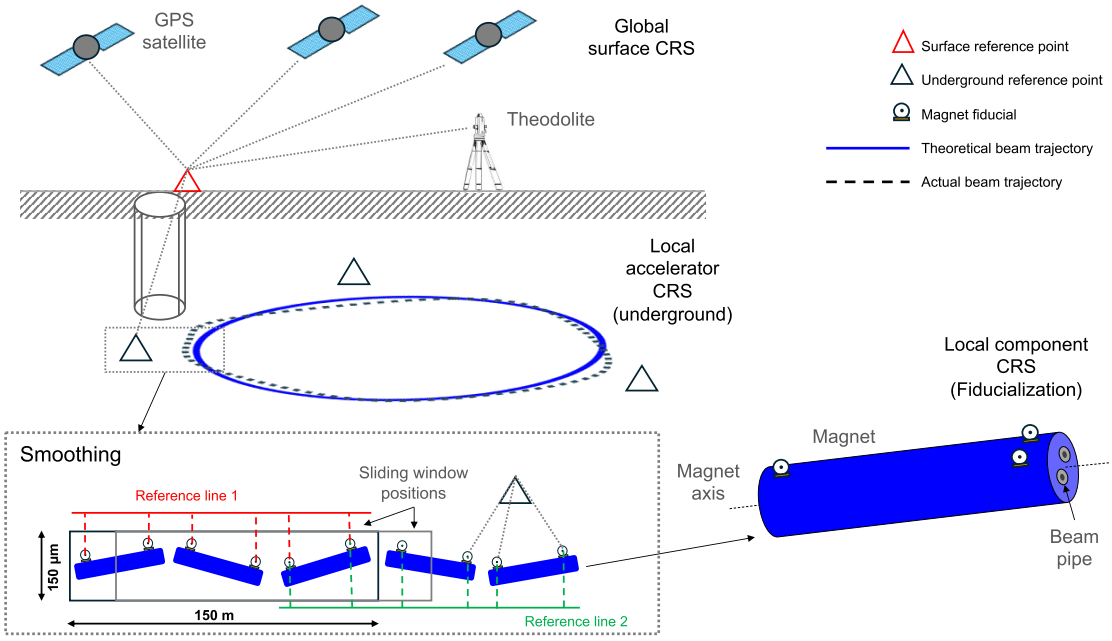


Figure 3.1: Illustration of the accelerator alignment workflow and principles.

of axes, units, and coordinate geometry. Additionally, it is defined by a so-called datum, which specifies the scale, location, and orientation of the coordinate system on Earth.

A Coordinate Reference Frame (CRF) is the realization of a given CRS, meaning the physical network of reference points whose coordinates have been determined in accordance with that CRS definition through observation. In other words, the CRS is the theoretical definition, and the CRF is its materialization in the form of known points and their measured coordinates. In the following text, when referring to the absolute or local geodetic reference of the accelerator, one must keep in mind this distinction between the CRS and its physical realization, CRF.

The vertical alignment of components of a large particle accelerator in a given CRS must take into account the variations of the direction of the vertical reference. A vertical reference surface is based on the geoid, which is defined as an equipotential surface of Earth's gravity field. For relatively small accelerators like the SPS, the geoid can be approximated as a sphere or ellipsoid. For the large accelerators such as the LHC or FCC, the local variations in Earth's mass distribution must be taken into account as they cause the gravity field non-uniformity.

Once the CRS is defined, the initial step in accelerator alignment involves determining the positions of the reference points within the surface network. This is done through a combination of satellite navigation, astronomical observations, trigonometry, and leveling. The positions of these reference points are established on the surface of the accelerator site in a well-defined global surface CRS (Fig. 3.1) [3, 28–30].

For underground accelerators, the geodetic reference must be transferred from the surface to the tunnel. At CERN, the absolute spatial reference is defined by the CERN Coordinate System (CCS). Absolute positions are then transferred from

the surface to the underground using access shafts. This transfer of geometry is performed using a variety of geodetic techniques. Knowledge of the quality and parameters of transformations between different CRSs is essential. It is directly linked to uncertainty or error, which directly affects the accuracy of all subsequent position measurements and component placements [3, 31].

Note that additional local system CRSs can be established as illustrated in Fig. 3.1. These local CRSs can be established for a single component or among multiple components. The local CRS can serve as a foundation for the measurements performed using, for example, a straight-line reference system.

3.1.2 Absolute and Relative Accelerator Alignment

One of the main goals in the accelerator alignment field is to maintain a smooth particle beam trajectory. For this purpose, a theoretical smooth curve is defined, which serves as an idealized, continuous reference trajectory, representing the large-scale geometric configuration that all aligned components should follow.

As a first step, the absolute alignment procedure places each accelerator component in its theoretical position within the CCS. It is important to recognize that, in practice, the actual trajectory followed by the particle beam can deviate from the ideal theoretical design (Fig. 3.1). Such deviations arise because errors accumulate at several stages: when transferring coordinates from the surface to the underground, during subsequent geometry transfers within the tunnel, and through multiple smoothing adjustments. The result is that the global absolute positioning of accelerator components in the CCS is typically done with an accuracy of a few millimeters. This absolute accuracy is sufficient as long as local relative alignment precision and smoothness are ensured.

The relative alignment procedure ensures that neighboring accelerator components are precisely positioned with respect to each other, hence preserving the smoothness of the overall beam trajectory even if the global absolute accuracy is lower. The relative alignment techniques used at LHC achieve the 1 sigma deviation of actual component positions from the smooth reference curve to no more than 0.15 mm within any 150 m long segment [6, 32]. This segment is a so-called sliding window defined with its own local CRS. The sliding window is systematically shifted following the theoretical smooth curve, ensuring the smoothness and particle beam stability along the entire 27 km circumference. This process is known as smoothing.

During the real alignment scenario at LHC, multiple, partially overlapping straight-line reference alignment systems must be used, instead of relying on a single long global reference line. Using a single, uninterrupted reference line could, in principle, simplify coordinate transformations and reduce cumulative errors associated with imperfect CRS conversions between the overlapping straight lines. However, there are limitations to the reference line length of the WPS as discussed in the chapter 3.2.4 [3].

3.1.3 Fiducialization

Fiducialization is a technique used for defining and precisely measuring the spatial relationship between an object's functional features and external reference points, using various metrological instruments. For example, in the case of a magnet, although the magnet axis and the beam pipe are not physically accessible once the magnet is assembled and mounted, fiducialization enables the precise determination of their position relative to external physical reference marks, such as laser tracker targets, which are placed on the magnet housing. These physical reference marks are known as fiducials. This technique allows for measuring and positioning the fiducialized component in space while knowing the position of the actual functional features that affect the particle beam trajectory.

The fiducialization is performed within the local component CRS as illustrated in Fig. 3.1. Note that the fiducialization process can introduce systematic errors due to environmental factors such as temperature changes, as well as due to measurement uncertainties associated with the metrological instruments used during this process [3, 29].

3.1.4 Software

Efficient accelerator alignment relies heavily on advanced software solutions specialized for different tasks. The data acquisition software is used to capture data from various measurement instruments. It also incorporates advanced error-checking algorithms to minimize inaccuracies. The data acquisition software can also be used to perform coordinate transformations and present results in a chosen CRS [3]. Tsunami is the main software used and developed at CERN for in-field data acquisition and alignment tasks, providing a unified platform for measurement campaigns and integration with the alignment CERN database [33].

The acquired data are later analyzed using a specialized software such as the least squares adjustment software LGC2 (Logiciel Général de Compensation). This software, also developed at CERN, is used for geodetic computations and position estimation based on measured data while considering the shape of the geoid in the calculations [34].

An example of a commercially available software is the Spatial Analyzer. This software package can be used both for acquiring measurements from a wide range of metrology instruments and for advanced analysis, including coordinate transformations, uncertainty calculations, and network adjustments [35].

3.2 State-of-the-Art Metrology Methods and Tools

This chapter describes various state-of-the-art metrology techniques used in accelerator alignment. A detailed examination of the underlying principles behind each technique provides a theoretical understanding, helping to establish a solid knowledge foundation for the reader. Some of these alignment measurement techniques were used as a basis for comparison of the results from the pseudo-nondiffracting

beam-based straight-line reference system presented as a part of this thesis. Note that some well-established alignment measurement methods, like photogrammetry, are not described in the following chapter due to their limited relevance to the context of the thesis.

3.2.1 Coordinate Measuring Machines

Coordinate Measuring Machines (CMMs) are used for the determination of spatial coordinates of the measured object. The core function of a CMM is to measure the physical geometrical characteristics of an object by sensing discrete points on the surface of the object with a probe. As the probe contacts or scans the object, the machine records the X, Y, and Z coordinates of each point. This process creates a three-dimensional map of the object in a Cartesian coordinate system. The probe can be a mechanical touch-trigger, optical, or laser-based, depending on the specific application and required precision.

Note that there are certain limitations to the object size given by the range of the motion of the specific CMM. Additionally, the measurements need to be performed in a dedicated laboratory with precisely controlled metrological conditions, such as temperature [36, 37]. In the context of accelerator alignment, CMMs can be used for the fiducialization, linking the geometry of the object to the fiducials [38].

3.2.2 Inclinometers

Roll angle measurement involves adjusting the rotation of accelerator components around the beam axis. The roll angle is typically measured using an inclinometer placed on a designated roll surface [3].

The principle of inclinometer measurements relies on detecting changes in the inclination of a measured object. In capacitive inclinometers, a conductive fluid partially fills a sealed chamber containing electrodes. As the inclinometer tilts, the fluid shifts, altering the capacitance between the electrodes. This change in capacitance is measured and converted into an angular measurement. Mechanical pendulum-based inclinometers use the motion of a suspended mass to detect tilt. The measurement accuracy can vary from the order of microradians to milliradians [6, 13].

3.2.3 Laser Trackers

Laser trackers are used for high precision three-dimensional position measurements of designated targets by combining angular observations with distance measurements. A laser tracker emits a laser beam directed at a target. This target is a retro-reflector, an optical element designed to reflect the laser light back to its source, returning incoming rays approximately parallel to their original direction regardless of the angle of incidence. Absolute distance is measured either by analyzing phase shifts of the reflected light relative to the local reference or by the time-of-flight principle. Simultaneously, the laser tracker measures the horizontal

and vertical angles relative to its internal coordinate system using highly sensitive angular encoders.

By combining these observations, the laser tracker calculates the three-dimensional position of the retro-reflector with an accuracy that can reach below 10 µm for distances up to a few meters. The accuracy of the measurement decreases with the distance from the laser tracker to the retro-reflector due to atmospheric disturbances and cumulative errors in angular measurements. For distances around 100 m, the accuracy reached is around 500 µm. Note that laser trackers can be linked to gravity via an integrated inclinometer [3, 39].

3.2.4 Straight-Line Reference Systems

Straight-line reference alignment systems measure deviations of accelerator components from a defined reference line. This is illustrated in Fig. 3.1. These systems consist of three core elements: the alignment reference (e.g., stretched wire), fiducials placed on the aligned components, and sensors measuring offsets from the reference. The spatial relationship between the sensors and fiducials is established through a fiducialization.

Wire Positioning and Hydrostatic Leveling Systems

The WPS is a state-of-the-art straight-line reference system used at accelerator facilities around the world, including Fermilab [40, 41], Stanford Linear Accelerator Center (SLAC) [42] and CERN [32]. The WPS utilizes a conductive wire as the reference line. The capacitive or optical sensors measure a horizontal and vertical offset relative to the wire. The three-ball-mount interface is one of the kinematic mount designs used at CERN as a support for the sensors, such as the ones used for WPS [3, 43]. This interface consists of three precision spheres with known diameters, typically made of hardened steel or ceramic, arranged in an equilateral triangle pattern. This pattern creates a highly repeatable and stable connection while constraining all six degrees of freedom. This design allows for precise repositioning after removing and returning the sensor with repeatability in the micrometer range [44].

The HLS utilizes interconnected vessels filled with water. Capacitive, ultrasonic, or optical sensors are used to measure the distance to the water surface, providing vertical reference measurements linked to gravity. The HLS is not a straight-line reference method, however, it complements WPS by enabling precise wire catenary modeling relative to the geoid for vertical offset measurements [13, 16].

Modern accelerators require the straight-line reference systems to achieve accuracy and repeatability on the level of hundreds to tens of micrometers over sliding windows spanning hundreds of meters [3, 45]. Combined, the WPS and HLS achieve 5 µm accuracy in the local CRS [32]. Despite their accuracy, these systems face some limitations. The fragile reference wire is prone to mechanical damage and can have only a certain length due to breaking under its own weight. HLS measurements remain strictly vertical, requiring integration with WPS data for multi-axis positioning. Both of the systems are also affected by gravity. While this can be lever-

aged in some applications, an idealized straight reference line defined geometrically rather than by gravity is preferred to enforce local smoothness of particle accelerator components. This arises because particle accelerators are typically designed with components aligned to a theoretical geometric plane or a line, rather than to a curve dictated by gravity.

Optical-Based Straight-Line Reference Systems

Optical straight-line reference systems present a promising solution to overcome the problems of fragile wire and the alignment reference length limitation. They are also independent of gravity. The underlying principles of these systems typically involve using an optical reference line and different detection principles to measure offsets from this line. Various optical methods have been developed in accelerator facilities around the world:

- **Gaussian beam based:** Gaussian beam, as one of the fundamental laser modes, has been considered for creating an alignment reference. The use of Gaussian beams for alignment was explored at CERN, where it was shown that the measurement accuracy and precision are mainly limited by atmospheric fluctuations, causing refractive index variations along the beam path. The study also emphasizes the importance of precise beam collimation to reduce divergence, facilitating alignment reference detection [9]. Additionally, a LAMBDA sensor was developed for the proposed linear accelerator CLIC at CERN. This system projects a GB through a vacuum onto a movable plate, with the beam center detected using image processing techniques. Note that the LAMBDA sensor was never deployed as part of a complete alignment system [46].

- **Rasnik system:** The Rasnik system is based on projecting a diffraction pattern onto a CCD detector. The relative displacement of the projected image provides sensitivity to transverse shifts of the system's components. Different variants were developed for particle physics experiments: the 4QD-Rasnik for LEP [47], the CCD-Rasnik for ATLAS [48], and later Rasdif [49], which replaces the lens with a diffraction plate and the mask with a monochromatic divergent light source, making alignment feasible over long distances of hundreds of meters without requiring impractically large optics.

- **Airy diffraction pattern based:** When a light travels through a circular aperture, diffraction effects lead to the creation of an Airy diffraction pattern, leading to a well-defined pattern that can serve as an alignment reference and is relatively simple to analyze. SPring-8 [50] and KEK [51, 52] employed an iris diaphragm laser alignment system based on this principle. This technique requires precise aperture geometry and alignment to produce a symmetrical pattern.

- **Fresnel zone plates:** Utilizing slits as diffraction elements to focus the laser beam onto a specific point can reduce the divergence. For instance, the SLAC

laboratory employed Fresnel plates for accelerator alignment [53]. Similarly, the High Energy Accelerator Research Organization in Japan (KEK) [54] and China Spallation Neutron Source (CSNS) [55] implemented similar systems. However, focusing the beam necessitates precise alignment of the optical elements. Sensitivity to the longitudinal misalignment can affect the sharpness and shape of the spot, hence the accuracy of the reference detection.

- **Poisson spot:** When a plane wave illuminates a sphere, the spherical obstruction causes diffraction effects that result in a characteristic Poisson spot, a bright diffraction point with an intensity profile described by a Bessel function. This spot arises from the symmetry of the sphere, causing all diffracted light waves to interfere constructively at the optical axis. The Poisson spot can be used as a stable optical reference with a predictably narrow diameter that scales with propagation distance and sphere size. This method was used at Advanced Photon Source (APS) [56], SLAC [57], and Deutsches Elektronen-Synchrotron (DESY) [58, 59]. This approach allows for monitoring multiple objects simultaneously with a single detector, enhancing efficiency.

While optical straight-line reference systems offer many advantages, they also face significant challenges. The first drawback is divergence of the optical reference, which becomes increasingly problematic over long distances. As the light propagates, it naturally spreads out due to diffraction, leading to a loss of precision in position measurements. This is particularly evident in systems using GBs such as the LAMBDA sensor, where the spot size can grow significantly over hundreds of meters, leading to a low-intensity variation in the pattern and difficulty in detecting the reference with high enough precision. Furthermore, the LAMBDA sensor needs to operate as a shutter system. This means that the mechanical shutter needs to cover the GB and prevent it from propagating further, to be able to measure the reference position. Due to this reason, only one sensor at a time can measure the beam, because the signal is covered by the sensors at a greater distance from the laser source. This leads to a drawback, that any small movement of the reference line, while measurements are being taken, can affect the accuracy, as measurements cannot be captured instantaneously [46, 60]. These challenges could be solved using pseudo-nondiffracting beams, more specifically LBs, as will become evident in the following chapters.

Another major challenge is the susceptibility of the optical reference to refractive index gradient and fluctuation due to the instability of the propagation medium. Even small variations in air temperature or pressure can cause the optical reference to deviate from a straight path [9, 49, 60–62]. This effect becomes more pronounced over longer distances and can introduce significant errors in alignment measurements. To mitigate this, a beam can propagate in a vacuum pipe, but this adds complexity and cost to the setup [49, 51, 52, 60]. Reflections inside the vacuum pipe may cause interference effects, resulting in a reduced signal-to-noise ratio of the optical pattern, which can compromise the detection of the alignment reference. To reduce this effect, apertures that block reflections along with a non-reflective coating of the pipe can be employed [49, 63].

4 Foundations of Electromagnetic, Scalar and Ray Optics

The following chapter introduces key concepts from electromagnetic theory and optics, which are necessary for the understanding of terms and principles used while describing optical phenomena in this thesis. These foundations provide the essential connection between electromagnetism, scalar diffraction theory, and ray optics, creating a coherent framework that allows the reader to understand the underlying principles that are used to describe SLBs and LBs.

4.1 Maxwell Equations

Maxwell's equations form the foundation of electromagnetism and optics. These equations provide a mathematical model for describing how electric and magnetic fields are generated and interact with each other, as well as with electric charges and currents. They can be expressed in either integral or differential mathematically equivalent form [64, 65].

4.1.1 Gauss's Laws

Gauss's law for electricity states that the total electric flux through a closed surface depends only on the net charge enclosed. Electric field lines are defined to point away from positive charges and toward negative charges. Hence, there can be a net positive or negative charge, implying that electric monopoles do exist. On the other hand, magnetic field lines in their definition always form closed loops, and every line that enters a surface must also exit it. In other words, it describes the fact that isolated magnetic monopoles do not exist. The integral forms are given as:

$$\oint_S \mathbf{E} \cdot \mathrm{d}\mathbf{S} = \frac{Q}{\epsilon_0}, \tag{4.1}$$

$$\oint_S \mathbf{B} \cdot \mathrm{d}\mathbf{S} = 0. \tag{4.2}$$

In the equations $\mathbf{E}$ is the electric field, $\mathbf{S}$ is the area vector, Q is the enclosed electric charge within S, ϵ_0 is the vacuum permittivity, and $\mathbf{B}$ is the magnetic field [64, 65].

4.1.2 Faraday's Law

If a coil of wire is connected to a galvanometer, the needle of the galvanometer is deflected when a magnet is moved back and forth from the coil, indicating an induced current. The direction and magnitude of the current depend on the direction and speed of the magnet's motion.

In other words, Faraday's law describes how a time-varying magnetic field induces an electric field. The integral form is given as:

$$\oint_l \mathbf{E} \cdot \mathrm{d}\mathbf{l} = -\frac{\partial}{\partial t} \int_S \mathbf{B} \cdot \mathrm{d}\mathbf{S}, \tag{4.3}$$

where $\mathrm{d}\mathbf{l}$ is the length element along the closed curve and t is time [64, 65].

4.1.3 Ampère-Maxwell's Law

If a current passes through a straight vertical wire, magnets placed around the wire align tangentially in a circular pattern centered on the wire. This demonstrates that there is a magnetic field created by the current.

This illustrates the core principle of Ampère's law, which relates the magnetic field around the wire to the electric current passing through it. The integral form is given as:

$$\oint_C \mathbf{B} \cdot \mathrm{d}\mathbf{l} = \int_S (\mu_0 \mathbf{J} + \mu_0 \epsilon_0 \frac{\partial \mathbf{E}}{\partial t}) d\mathbf{S} \tag{4.4}$$

where μ_0 is the vacuum permeability, and $\mathbf{J}$ is the current density [64, 65].

4.1.4 Differential Form of Maxwell's Equations

Maxwell's equations are often written in differential forms using vector calculus. These can be derived from their integral forms using the divergence theorem and Stokes' theorem:

$$\nabla \cdot \mathbf{E} = \frac{\rho}{\varepsilon_0}, \qquad \text{(Gauss's law for electricity)} \tag{4.5}$$

$$\nabla \cdot \mathbf{B} = 0, \qquad \text{(Gauss's law for magnetism)} \tag{4.6}$$

$$\nabla \times \mathbf{E} = -\frac{\partial \mathbf{B}}{\partial t}, \qquad \text{(Faraday's law)} \tag{4.7}$$

$$\nabla \times \mathbf{B} = \mu_0 \mathbf{J} + \mu_0 \varepsilon_0 \frac{\partial \mathbf{E}}{\partial t}. \qquad \text{(Ampère-Maxwell law)} \tag{4.8}$$

In the equations, ρ is defined as the electric charge density [64, 65].

4.2 Wave and Helmholtz Equations

4.2.1 Wave Equation

The wave equation is a second-order linear partial differential equation that describes how waves move through space and time. The wave equation can be derived from Maxwell's equations for electromagnetic waves propagating in a linear, homogeneous, isotropic, and non-dispersive medium with no free currents and charges ($\mathbf{J} = 0$, $\rho = 0$). Taking the curl of Faraday's law and substituting $\nabla \times \mathbf{B}$ from Ampère-Maxwell's law yields:

$$\nabla \times (\nabla \times \mathbf{E}) = -\frac{\partial}{\partial t}(\nabla \times \mathbf{B}) = \mu_0 \varepsilon_0 \frac{\partial^2 \mathbf{E}}{\partial t^2}. \tag{4.9}$$

Using the vector identity $\nabla \times (\nabla \times \mathbf{E}) = \nabla(\nabla \cdot \mathbf{E}) - \nabla^2 \mathbf{E}$, while substituting $\nabla \cdot \mathbf{E} = 0$, a wave equation can be derived as:

$$\nabla^2 \mathbf{E} - \mu_0 \varepsilon_0 \frac{\partial^2 \mathbf{E}}{\partial t^2} = 0. \tag{4.10}$$

A plane wave, infinite in space and time, represents a monochromatic wave with a uniform phase front and is one of the fundamental solutions of the wave equation:

$$\mathbf{E}(\mathbf{r}, t) = \mathbf{E}_0 e^{i(\mathbf{k}\cdot\mathbf{r} - \omega t + \varphi)}. \tag{4.11}$$

In this expression, the term $\Phi = \mathbf{k} \cdot \mathbf{r} - \omega t + \varphi$ represents the phase of the wave, where $|\mathbf{k}| = \frac{2\pi}{\lambda}$ is the wave vector, λ is the wavelength, $\mathbf{r}$ is the position vector, ω is the angular frequency and φ is the phase constant. Wavefront is defined as a surface of a constant phase. The plane wave is propagating in the direction of $\mathbf{k}$, with $\mathbf{E}_0$ as its amplitude [64, 65].

4.2.2 Helmholtz Equation

The Helmholtz equation is a second-order partial differential equation that describes how waves propagate in space. We can assume a harmonic time dependence of the electric field:

$$\mathbf{E}(\mathbf{r}, t) = \mathbf{E}(\mathbf{r}) e^{i\omega t}, \tag{4.12}$$

where $\mathbf{E}(\mathbf{r})$ represents the spatial variation of the field, and $e^{-i\omega t}$ captures the harmonic behavior in time. Substituting the time-harmonic field $\mathbf{E}(\mathbf{r}, t) = \mathbf{E}(\mathbf{r}) e^{i\omega t}$ into the wave equation (Eq. 4.10) gives the Helmholtz equation:

$$\nabla^2 \mathbf{E}(\mathbf{r}) + k^2 \mathbf{E}(\mathbf{r}) = 0, \tag{4.13}$$

with wavenumber $k = \frac{\omega}{c}$, where c is the speed of light. A similar equation holds for the magnetic field. This approach simplifies solving for spatial field distributions without explicitly dealing with time dependence. If we assume a solution of the

Helmholtz equation for a specific case of a plane electromagnetic wave propagating in a direction given by the vector $\mathbf{k}$ we obtain:

$$\begin{aligned} \mathbf{k} \times \mathbf{E} &= \omega \mathbf{B}, \\ \mathbf{k} \times \mathbf{B} &= -\epsilon_0 \mu_0 \omega \mathbf{E}. \end{aligned} \tag{4.14}$$

The equations demonstrate that the vectors $\mathbf{E}$, $\mathbf{H}$, and $\mathbf{k}$ form a right-handed system, which is a fundamental property of electromagnetic waves. In this configuration, the electric and magnetic fields are mutually perpendicular to each other and to the direction of wave propagation. The mutual induction of electric and magnetic fields described by Maxwell's equations allows electromagnetic waves to propagate. The changing fields continuously regenerate each other while maintaining their transverse nature relative to the propagation direction, meaning the wave is self-sustaining as it propagates [64, 65].

4.2.3 Paraxial Helmholtz Equation

The paraxial approximation assumes that the wave field primarily propagates nearly parallel to the optical axis. It can be used for further simplification of the Helmholtz equation. The vector components of the $\mathbf{E}$ field are a mutually uncoupled system, and each of these components is a solution to a scalar Helmholtz equation. Hence, the solution can be represented by a scalar function $u(x, y, z)$, and the scalar Helmholtz equation takes the form:

$$\nabla^2 u - k^2 u = 0. \tag{4.15}$$

We assume the solution that takes the form of a spatially confined scalar wave propagating in the z-direction $u(x, y, z) = U(x, y, z)e^{-ikz}$, where the field amplitude varies slowly along the propagation direction, hence $\frac{\partial^2 U}{\partial z^2} << 2k\frac{\partial U}{\partial z}$. By substituting into Eq. 4.15 we get the paraxial Helmholtz equation:

$$\nabla_T^2 U - 2ik\frac{\partial U}{\partial z} = 0, \tag{4.16}$$

where ∇_T^2 is the transverse Laplacian. This approximation holds for angles close to the optical axis, ensuring small beam divergence and wavefront curvature [64, 65].

4.3 Polarization of Electromagnetic Waves

Polarization describes the orientation of the electric field vector as the wave propagates. While the general concept of polarization applies to any transverse wave, in optics it is conventional to define polarization specifically in terms of the electric field vector $\mathbf{E}$. The vector field can be described in the orthogonal coordinate system using its transversal components. When we assume that these components can have a different value of phase, we can write:

$$\begin{aligned} E_x &= E_{x0}\cos(\Phi), \\ E_y &= E_{y0}\cos(\Phi+\delta), \end{aligned} \tag{4.17}$$

where δ is the phase difference between the x and y components. The polarization state of the electric field vector is determined by the amplitudes E_{x0}, E_{y0}, and the phase difference δ. The tip of the electric field vector traces an ellipse in the transverse plane that can be described using the equation:

$$\left(\frac{E_x}{E_{x0}}\right)^2 - 2\frac{E_x}{E_{x0}}\frac{E_y}{E_{y0}}\cos\delta + \left(\frac{E_y}{E_{y0}}\right)^2 = \sin^2\delta. \tag{4.18}$$

The equation describes different polarization states. If $\delta = 0, \pi$, the polarization is linear. For the situation of $E_{x0} = E_{y0}$ and $\delta = \pm\pi/2$ the polarization is circular. All other cases result in the most general case, which is the elliptical polarization [64, 65].

4.4 Scalar Diffraction Theory

Scalar diffraction theory is used to analyze light propagation phenomena while simplifying the problem by treating electromagnetic waves as scalar fields. Therefore, it does not account for the vector nature of light and neglects polarization, electromagnetic field interactions, and effects that arise in materials or structures with dimensions comparable to the wavelength. However, it accounts for the wave nature of light.

Scalar theory can be used to describe how light behaves when it travels through an aperture. However, with several additional simplifying conditions. The region outside the aperture is assumed to be perfectly opaque and infinitely thin, so the field is set to zero everywhere on the screen except at the aperture. Due to the non-homogeneity of the propagation medium on the edges of the aperture, the aperture size must be significantly larger than the wavelength of the light. Also, the diffraction pattern behind the aperture needs to be observed at a distance which is significantly longer than the wavelength [64, 65].

4.4.1 Fourier Optics

Fourier optics describes wave propagation through space using the principles of Fourier analysis, the theory of linear systems, and the principle of superposition. The principle of superposition states that any linear combination of solutions to a linear equation is also a solution. The wave and Helmholtz equations are linear, which means that a complicated optical field can be broken down into a set of plane waves, each with a different phase, amplitude, and direction. This allows one to find the solution for the propagation of this field, for example, in space, by simply solving the propagation for each of the plane waves individually and later combining them. This approach can be useful for solving complex problems.

The Fourier transformation is first used to decompose a scalar field $a(x, y, z)$, which is a solution to a scalar Helmholtz equation, into its harmonic components. Mathematically, it is given by:

$$\mathcal{FT}\{a(x, y, z)\} = \mathcal{A}(f_x, f_y, z) = \int\int_{-\infty}^{\infty} a(x, y, z) e^{2\pi i(f_x x + f_y y)} \, \mathrm{d}x \, \mathrm{d}y, \tag{4.19}$$

where $f_x = \frac{x}{\lambda z}$ and $f_y = \frac{y}{\lambda z}$ are the spatial frequencies in the x and y directions, respectively.

The impulse response refers to the output of a system when presented with an impulse, such as a point source in the case of an optical system, as the input. It fully characterizes the system's behavior, allowing the propagation of any arbitrary input field to be determined through convolution with this impulse response. To find the form of the field $a(x, y, z)$ that propagates in free space from the zero plane to a plane in the given distance z, we need to know the impulse response of the free space. Assuming that the system is spatially invariant, this process can be mathematically described in the frequency domain using the equation:

$$\mathcal{A}(f_x, f_y, z) = \mathcal{A}(f_x, f_y, 0)\mathcal{H}(f_x, f_y, z), \tag{4.20}$$

where $\mathcal{H}(f_x, f_y, z)$ is a so-called free-space transfer function and takes the form:

$$\mathcal{H}(f_x, f_y, z) \approx e^{-ikz\sqrt{1-\lambda^2 f_x^2 - \lambda^2 f_y^2}}. \tag{4.21}$$

Note that the condition $\sqrt{f_x^2 + f_y^2} < \frac{1}{\lambda}$ must be fulfilled [64, 65].

4.4.2 Diffraction Integral

The Huygens principle forms the conceptual basis for the diffraction integral, which is used to calculate how a complex field propagates in space. The Huygens principle states that every point on a wavefront acts as a source of secondary spherical waves. The superposition of these secondary waves forms the new wavefront. To formulate the diffraction integral, imagine a situation where a point source O is emitting a spherical wavefront incident upon an aperture. The complex field $V(P)$ at an observation point P, located beyond the aperture, is then given by the superposition of all secondary waves emanating from each point of the aperture. It can be expressed as a superposition integral over the aperture A:

$$V(P) = \iint_A K(\chi) \frac{e^{ik(r_0 + r)}}{r_0 r_1} U(R) dA, \tag{4.22}$$

where $U(R)$ is the complex amplitude at a point R, which is located in the aperture plane and lies on the original wavefront, which was emitted by point source O, r_0 represents the distances from the point source O to the point R, r_1 represents the distance from R to the observation point P, and $K(\chi)$ is the inclination factor. The inclination factor accounts for the angular dependence of the secondary

spherical wave's amplitude and plays a critical role in the accurate description of the diffraction behavior.

The diffraction integral was derived using different mathematical principles by Fresnel, Kirchhoff, Sommerfeld, and others. Each of these derivations leads to a different form of the inclination factor. Under paraxial approximation, spherical wavefronts can be approximated as parabolic wavefronts, simplifying the analysis near the optical axis. In this case, the inclination factor can be approximated as unity. This approximation is known as the Fresnel approximation and applies to a so-called near-zone. The diffraction integral can then be written as:

$$a(x,y,z) \approx \frac{i}{\lambda z} e^{-i\frac{\pi}{\lambda z}(x^2+y^2)} \iint_{-\infty}^{\infty} a(\bar{x},\bar{y},0)\, e^{-i\frac{\pi}{\lambda z}(\bar{x}^2+\bar{y}^2)} e^{2\pi i\left(\bar{x}\frac{x}{\lambda z}+\bar{y}\frac{y}{\lambda z}\right)} d\bar{x}d\bar{y}. \tag{4.23}$$

When the propagation distance becomes much larger, all secondary spherical waves can be approximated by plane waves. This arises because the wavefront curvature in the paraxial area becomes negligible. This leads to a so-called Fraunhofer approximation, which holds for the so-called far-zone. The distinction between the Fresnel and Fraunhofer diffraction zones is defined by the Fresnel number $F_n = \frac{a^2}{\lambda z}$, with a being the aperture radius. The distinction holds for $F_n < 0.5$ as the quadratic phase term in Eq. 4.23 becomes $e^{-i\frac{\pi}{\lambda z}(\bar{x}^2+\bar{y}^2)} \approx 1$. The diffraction integral simplifies as:

$$a(x,y,z) \approx \frac{i}{\lambda z} e^{-i\frac{\pi}{\lambda z}(x^2+y^2)} \iint_{-\infty}^{\infty} a(\bar{x},\bar{y},0)\, e^{2\pi i\left(\bar{x}\frac{x}{\lambda z}+\bar{y}\frac{y}{\lambda z}\right)} d\bar{x}d\bar{y}, \tag{4.24}$$

where the integral is a two-dimensional Fourier transformation:

$$\mathcal{A}(f_x,f_y) = \mathcal{FT}\{a(\bar{x},\bar{y})\} = \iint a(\bar{x},\bar{y}) e^{2\pi i(k_x\bar{x}+k_y\bar{y})} d\bar{x}d\bar{y}, \tag{4.25}$$

and therefore:

$$a(x,y,z) \approx \frac{i}{\lambda z} e^{-i\frac{\pi}{\lambda z}(x^2+y^2)} \mathcal{A}\left(\frac{x}{\lambda z}, \frac{y}{\lambda z}\right). \tag{4.26}$$

This form demonstrates that the observed field distribution in the far-field is given by the Fourier transformation of the initial aperture field [64, 65].

4.5 Ray optics

Ray optics, also known as geometrical optics, is a simplification of wave optics that models light as rays traveling in straight lines, representing the direction of energy flow. This approximation is valid when the wavelength of light is much smaller than the dimensions of the structures it interacts with, allowing complex wave phenomena like diffraction and interference to be neglected. By treating light as rays, the analysis of optical systems becomes more intuitive, focusing primarily on refraction, reflection, and propagation paths through different media.

4.5.1 Eikonal Equation

Eikonal equation provides the link between wave and ray optics. We assume a non-homogeneous medium, where the permittivity, hence the refractive index, is a function of space. Assuming that the permittivity changes slowly in space ($|\nabla\epsilon|\lambda << 1$), we can apply the scalar Helmholtz equation to describe a wave traveling in this medium with the solution written as:

$$u(x, y, z) = V(x, y, z)e^{iS(x,y,z)}, \tag{4.27}$$

where $S(x, y, z)$ is the so-called Eikonal describing the spatial distribution of phase. Assuming the wavelength approaches zero (short-wavelength limit), the solution yields the Eikonal equation:

$$|\nabla S|^2 = n^2. \tag{4.28}$$

The short-wavelength limit implies that diffraction effects are negligible, as the light is assumed to travel in straight lines and is fully blocked by obstacles. This approximation leads to ray optics.

The gradient of the Eikonal (∇S) represents the direction of the steepest change of the phase. The steepest change of the phase is by definition in the direction of the propagation, which is represented by rays. Wavefront is a surface with a constant phase, therefore, the direction of the steepest change implies the perpendicularity of the rays to the wavefront [64, 65].

4.5.2 Snell's Law

Snell's law governs the refraction of light at the interface between two media with different refractive indices n_1 and n_2. It can be derived by analyzing the boundary conditions imposed by Maxwell's equations on electromagnetic waves crossing the interface. These conditions ensure the continuity of the tangential components of the electric and magnetic fields along the interface between two media, therefore:

$$\begin{aligned}(\mathbf{E}_2 - \mathbf{E}_1) \times \hat{\mathbf{n}} &= 0,\\ (\mathbf{H}_2 - \mathbf{H}_1) \times \hat{\mathbf{n}} &= \mathbf{J},\end{aligned} \tag{4.29}$$

where $\hat{\mathbf{n}}$ is the unit normal vector to the interface. Assume a plane wave $\mathcal{E}_1$ incident on the interface together with reflected plane wave $\mathcal{E}_1'$ and refracted plane wave $\mathcal{E}_2$. The continuity of the tangential component of $\mathbf{E}$ and $\mathbf{H}$ directly implies phase continuity. Hence, at the boundary, the tangential components of the wave vectors of these plane waves must be continuous. This means that Snell's law can be written as:

$$\begin{aligned}(\mathbf{k}_2 - \mathbf{k}_1) \times \hat{\mathbf{n}} &= 0,\\ (\mathbf{k'}_1 - \mathbf{k}_1) \times \hat{\mathbf{n}} &= 0.\end{aligned} \tag{4.30}$$

Snell's law can also be written in the form of:

$$n_1 \sin \beta_1 = n_2 \sin \beta_2, \tag{4.31}$$

where β_1 and β_2 are corresponding angles of incidence and refraction. Snell's law can be effectively used for tracing rays through optical elements [64, 65].

5 Introduction to Optical Beams

Optical beams are spatially localized solutions of the wave or Helmholtz equation that propagate with a well-defined spatial profile. By tailoring their amplitude, phase, or polarization, beams can be engineered to exhibit unique properties such as low divergence, self-healing, or curved trajectories. This chapter introduces the concept of Gaussian and various types of non-diffracting beams.

5.1 Gaussian Beams

GBs are one of the most well-known solutions of the paraxial Helmholtz equation:

$$u(x,y,z) = U_0 \frac{w_0}{w(z)} e^{-\frac{x^2+y^2}{w^2(z)}} e^{-i\left(kz + \frac{k(x^2+y^2)}{2R(z)} - \zeta(z)\right)}, \tag{5.1}$$

where $w(z)$ is the beam waist radius, describing the beam's width as a function of distance z, w_0 is the minimum beam waist located at the beam focus, $R(z)$ is the radius of wavefront curvature and $\zeta(z) = atan(\frac{z}{z_0})$ is the Gouy phase, representing an additional phase shift induced as the beam propagates. GBs are characterized by their Gaussian intensity profile. The evolution of the beam waist radius $w(z)$ is described by the equation:

$$w(z) = w_0 \sqrt{1 + \left(\frac{z}{z_R}\right)^2}. \tag{5.2}$$

where $z_R = \frac{\pi w_0^2}{\lambda}$ is the Rayleigh length. The divergence angle is governed by the equation:

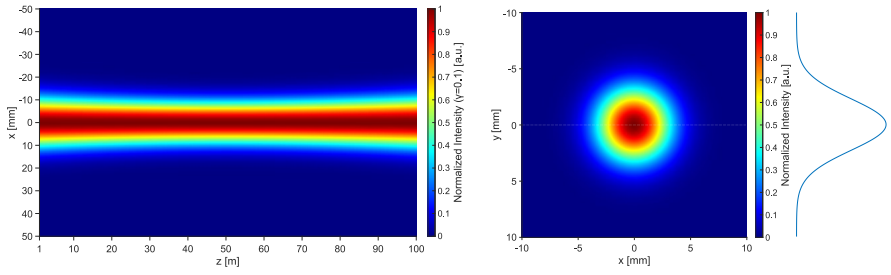


Figure 5.1: GB's longitudinal profile, together with the transversal profile taken in 4 m accompanied by a diametral line intensity profile.

$$\theta = \frac{\lambda}{\pi w_0}. \tag{5.3}$$

The beam waist $w(z_R) = \sqrt{2}(w_0)$. Hence, the beam remains relatively collimated with a negligible divergence for distances shorter than z_R. For longer distances, the beam diverges linearly, reducing the intensity quadratically. This causes a significant drawback for long-distance alignment applications, caused by the reduction in intensity contrast due to the divergence of the beam waist, which can cause complications when detecting the alignment reference position [46]. The beam divergence can be reduced by increasing the size of the beam waist. A focused GB with a $w_0 = 4$ mm located in 50 m can be seen in Fig. 5.1 [64, 65].

5.2 Non-Diffracting Beams

Non-Diffracting beams [24], or in other words, caustic beams [23], or structured light [22], are a class of optical beams that exhibit unique propagation properties. Unlike GBs, caustic beams are defined by regions of overlapping rays that form areas with high intensity and low intensity caused by interference. The regions with high intensity are known as caustics. When experimentally realized, these beams maintain their intensity profiles over extended propagation distances, showing pseudo-nondiffracting behavior and self-healing capabilities.

The theoretical foundation of caustics lies in catastrophe theory, which describes singularities in systems governed by nonlinear potential functions. The potential function $P_n(b, s)$ is expressed as [66, 67]:

$$P_n(b, s) = s^n + \sum_{j=1}^{n-2} \frac{b_j s^j}{b_{0j}}. \tag{5.4}$$

where s represents the state variable, and b_j are control parameters that influence the system's behavior and b_{0j} is the normalization factor. Different orders of catastrophes correspond to specific types of optical beams:

- $n = 3$, corresponds to fold-type catastrophe and is associated with Airy beams [68, 69],
- $n = 4$, cusp-type catastrophes arise, giving rise to Pearcey beams [70],
- $n = 5$ and higher orders lead to more complex structures like Swallowtail beams [71].

Ray theory predicts the infinite intensities at caustics. Hence, the diffraction catastrophe integral must be used to describe the interference effects that occur in the ray overlapping regions. The diffraction catastrophe integral is a solution to the paraxial Helmholtz equation. It incorporates interference effects by adding contributions from all possible ray paths. It involves expressing the complex field

as an integral over a potential function. The principle of the stationary phase is applied to approximate contributions from stationary points of P_n, corresponding to ray paths. This leads to an integral form [66, 67]:

$$C_n(b) = \int_{-\infty}^{\infty} \exp\left[iP_n(b,s)\right]\, ds, \tag{5.5}$$

Catastrophe theory predicts that caustics arise at points where P_n is stationary in s, hence where $\partial P_n/\partial s = 0$, manifesting as high-intensity regions of the optical field [23].

For the context of this thesis, it is essential to note that wavefronts can be interpreted as generating functions for light rays. The geometry of a wavefront determines how rays propagate and overlap to form caustics.

One of the most common ways of generating caustic beams is to encode their angular spectrum onto a spatial light modulator (SLM) [69–73]. The encoded spectrum is placed in the front focal plane of a convex lens. This lens performs a Fourier transformation of the spectrum, reconstructing the spatial profile of the beam in the back focal plane. Other means of generation can utilize specialized components such as phase plates or diffraction elements [74–83].

5.2.1 Airy Beams

Airy beams (AiBs) were one of the first experimentally realized caustic beams that opened the doors for future research in this field [68]. AiBs exhibit unique properties such as a parabolic trajectory and resilience to diffraction. The Airy function is related to the catastrophe diffraction integral and potential function with n = 3. The Airy integral can be defined as [23, 66, 67]:

$$C_3(b) = Ai(x) = \int_{-\infty}^{\infty} \exp\left(i\left(s^3 + xs\right)\right) ds, \tag{5.6}$$

The angular spectrum of the AiB at the initial state of propagation is characterized by the cubic phase term. For the experimental realization of the AiB, its angular spectrum must be modified to include a Gaussian amplitude, resulting in what is commonly referred to as an Airy-Gaussian beam. This modification ensures that the beam has finite energy, as the ideal AiB has infinite energy, which is physically unrealizable [69].

Dual Airy beams (DABs) extend the traditional AiB concept, offering enhanced control over beam propagation and novel properties. DABs are composed of two symmetrical AiBs that accelerate mutually in opposite directions, exhibiting a reflectional symmetry of the transverse intensity pattern [84]. Similar to the DABs, Symmetric Airy beams (SABs) arise from symmetrizing the spectral cubic phase of an AiB, creating two AiBs with opposite accelerating directions [72]. DABs and SABs initially propagate with a single central lobe that autofocuses and then collapses as the beam propagates further.

Radially symmetric AiBs, known also as Circular Airy beams (CABs), represent a cylindrically symmetric AiBs that exhibit abrupt autofocusing properties. These

beams are generated by extending the one-dimensional Airy function to cylindrical coordinates, resulting in a circularly symmetric intensity pattern with a bright core and concentric rings [85–88]. The key characteristic of CABs is their ability to concentrate energy into a small, high-intensity focal spot that forms after a certain propagation distance, while the intensity remains low up to that point. This makes them ideal for applications like ablation [86], or manipulation of small particles [89].

5.2.2 Bessel Beams

Bessel beams (BBs) are a class of optical beams whose transversal intensity profile consists of a bright central core surrounded by concentric rings, as in the case of CABs. However, the intensity profile of a BB does not spread out or change as the beam propagates. BBs are the solution to the non-paraxial scalar Helmholtz equation in cylindrical coordinates, where $x = rcos(\alpha), y = rsin(\alpha)$. The solution for a zero-order BB can be expressed as [25]:

$$v(r, \alpha, z) = V_0 J_0(k_T r) e^{-ik_z z}, \tag{5.7}$$

where $J_0(k_T r)$ is the zeroth-order Bessel function of the first kind, describing the radial intensity distribution. The $k_T = ksin(\theta_0)$ and $k_z = kcos(\theta_0)$ are the wavevector components. The properties of the beam arise from the constructive interference of plane waves traveling at an angle θ_0 to the z-axis (the beam propagation axis). The number and spacing of the concentric rings surrounding the central core are directly related to the transverse wavevector k_T. A larger k_T results in a smaller central core diameter and more closely spaced rings, while a smaller k_T produces a broader central core and fewer, more widely spaced rings.

BBs can be experimentally realized using axicons (conical lenses) [90]. This means of generation intuitively leads to the connection to caustics by considering the fact that the different parts of the beam overlap to generate the beam, due to the conical shape of the axicon. Note that there are also several other ways of generating BBs, using, for example, diffractive optical elements [91], or SLMs [92].

BBs offer some advantages for alignment applications and have been used for alignment [93–96]. Unlike GBs, the central core of a BB remains narrow and well-defined. This minimizes errors caused by beam spreading, which can lead to lower precision in the detection of the reference position.

Despite these advantages, the main drawback of BBs is a problematic experimental realization over propagation distances of hundreds of meters. Ideal BBs would require infinite spatial dimensions and are therefore not physically realizable. The experimentally generated ones propagate without significant spreading only over a limited range. Note that there have been several proposals for long-distance BBs propagation that, to our best knowledge, have not been experimentally verified [97–99].

5.2.3 Pin Beams

In recent years, so-called Pin beams (PBs) are getting a lot of attention, as they represent a distinctive class of pseudo-nondiffracting beams characterized by their ability to maintain structural profile over propagation distances of kilometers [100].

The generation principle of PBs is similar to that of CABs. It relies on assembling multiple AiBs in a circular configuration, individually engineered to accelerate along a trajectory that bends toward the common central axis, where each pair bends toward the center from opposite directions [100]. The unique geometric arrangement creates an autofocusing effect that enables the beam to exhibit pseudo-nondiffractive properties over long distances through the cancellation of transverse wavevectors.

PBs were experimentally generated using a single transparent phase mask [100] and by programming an SLM to imprint the required angular phase profile on a collimated laser beam [101]. The phase mask is designed so that the outgoing wavefront mimics the composite of cubic-phase Airy segments distributed around a circle.

The primary advantages of the PBs include their robust propagation through atmospheric turbulence over kilometer distances, significantly outperforming conventional Gaussian beams in terms of shape preservation and resistance to diffraction, making them particularly valuable for free-space optical communication [100, 102].

6 Structured Laser Beams and Layer Beams

SLBs and LBs are part of the class of pseudo-nondiffracting beams. They can, in theory, propagate indefinitely while preserving their structured intensity patterns and exhibiting very low divergence of certain parts of the beam, overcoming the limitation of BBs. Specifically, in the context of SLBs, the divergence of the inner core for a specific generator configuration is equal to 10 µrad [45, 61, 62]. This property, which results in a confined inner core and structured pattern over the whole propagating distance, greatly facilitates the detection of the alignment reference, overcoming the detection problems caused by the divergence of GBs. This can be clearly seen by comparing Figs. 5.1 and 6.2c, as the inner core of the SLB can be significantly smaller along the whole propagation path of the beam.

6.1 Generating Principle and Beam Properties

Careful manipulation of optical aberrations allows one to induce a specific phase delay and to engineer a generating wavefront, which enables the production of various types of caustic beams. The nature of the beams is determined by the shape of the generating wavefront [103–109]. This technique introduces the underlying principle behind the generation of SLBs and LBs, which can provide a cost-effective means of beam generation using, for example, inexpensive off-the-shelf lenses. This would be particularly beneficial for the optical-based straight-line alignment systems, when a large number of these systems need to be deployed in the vast area of a particle accelerator such as the FCC.

An SLB generator can be constructed using two plano-convex lenses placed one after the other. The first lens, the so-called phase lens, is followed by a second lens, referred to as the projection lens (Fig. 6.1). To generate an SLB that propagates to infinity, the distance between the lens-facing surfaces L_{PL} must fall within a specific interval of distances which depends on the generator parameters. When this condition is met and the generator is illuminated by linearly polarized laser light, the generating wavefront takes a distinctive "Sombrero-like" shape and has the diametral line-profile of the generating wavefront with two local minima and one local maximum. This leads to the formation of an SLB with an intense inner core, surrounded by concentric rings and ending with an outer ring (Figs. 6.2a, 6.2b, and 6.2c). The generating wavefront has rotational symmetry and is described by [45, 110]:

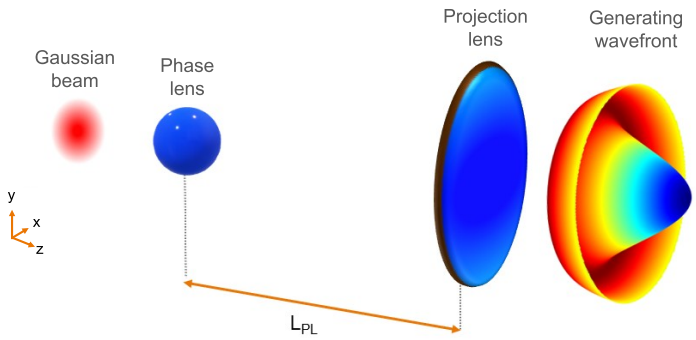


Figure 6.1: Optical setup of an SLB generator consisting of phase and projection lenses.

$$W(r,\alpha) = W(r) = K_1 r^2 + \sum_{m=1}^{\infty} K_{(m+1)} r^{2(m+1)}, \tag{6.1}$$

where r is the radial coordinate, α is the azimuthal angle, the term with the squared power K_1 relates to defocus, and higher-order even terms correspond to different orders of spherical aberration.

So-called Hollow SLB (HSLB) can be generated by illuminating an SLB generator using beams exhibiting non-classical polarization states. When using radially polarized input beams, the resulting HSLB contains a dark central core with longitudinal electric field components and vanishing magnetic fields. The HLSB generated using the radially polarized light is shown in Fig. 6.2d. Conversely, azimuthal polarization of an input beam produces HSLBs with dominant longitudinal magnetic fields in the dark core region. Intermediate spiral polarization states create HSLBs with mixed longitudinal electric and magnetic field components in the central dark region based on the proximity of the input spiral beam to the azimuthal or radial polarization. This polarization-dependent generation mechanism arises from the interaction between the beam's angular momentum and the optical aberrations introduced by the generator's phase elements, producing destructive interference in the beam's central region [111–113].

In the case of LBs, cylindrical lenses can be used to generate the beam. This modifies the symmetry of the wavefront as illustrated in Fig. 1 of the paper in the chapter 7.5 [114]. The resulting beam has no inner core or concentric rings. However, the beam manifests as parallel lines in the transverse intensity profile, while changing the shape of the outer ring to the outer line (Fig. 6.2e). The generating wavefront of LBs remains consistent along one axis (e.g., y-axis), with its profile given by [114]:

$$W(x,y) = W(x) = K_1 x^2 + \sum_{m=1}^{\infty} K_{(m+1)} x^{2(m+1)}, \tag{6.2}$$

where x is the transverse coordinate. This equation ensures uniformity along y, resulting in parallel lines in the transverse intensity distribution. Note that additional lenses can be added to prolong the lines in the transversal intensity profile

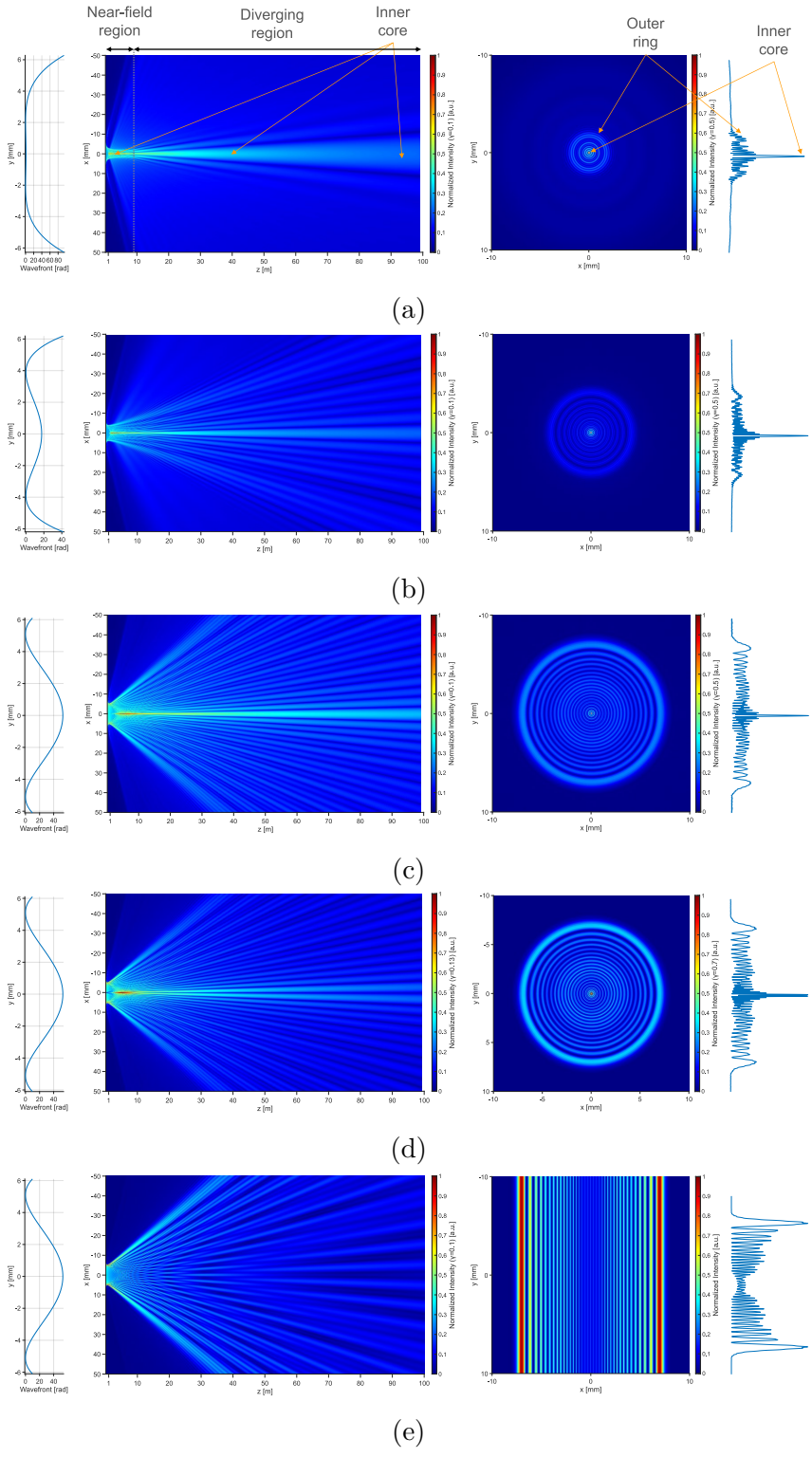


Figure 6.2: Each figure follows the same layout, from left: Generating wavefront diametral line-profile, longitudinal intensity profile, transversal intensity profile at 3 m away from the generator (gamma enhanced for better visibility), diametral intensity line-profile. (a) SLB (L_{PL} = 74 mm), (b) SLB (L_{PL} = 73 mm), (c) SLB (L_{PL} = 72 mm), (d) HSLB (L_{PL} = 72 mm), and (e) LB (L_{PL} = 72 mm).

along the y-axis or to create two-dimensional beams (see Figs. 2, 3, 12 and 18 of the publication in the chapter 7.5 [114]).

A change of the distance between the lens facing surfaces L_{PL} influences mainly the amount of the defocus in the optical system, which causes the generating wavefront to change shape causing the beam to have different properties such as different number of rings or lines, or the size of the inner core of the SLB [111]. This is illustrated in Fig. 6.2. The beams in Fig. 6.2 were simulated using a generator consisting of two plano-convex lenses with a round symmetry for the SLBs and HSLB. The generator of the LB consisted of two plano-convex cylindrical lenses. For all the generators, the phase lens had a focal length of 15 mm and an aperture size of 12.7 mm. The projection lens had a focal length equal to 60 mm, and the aperture size was 50.8 mm. The lenses were facing each other with the convex surfaces, and the material was chosen to be the N-BK7 glass for both. The circular input beam was a plane wave with a diameter of 3 mm.

Optical elements that would introduce a similar phase delay, such as phase plates, mirrors, or SLMs, can also be used to form the beam. Note that the generation mechanism can also be explained by the fact that the phase lens introduces a specific angular spectrum modification in the Fourier plane, while the projection lens performs the Fourier transformation [114, 115].

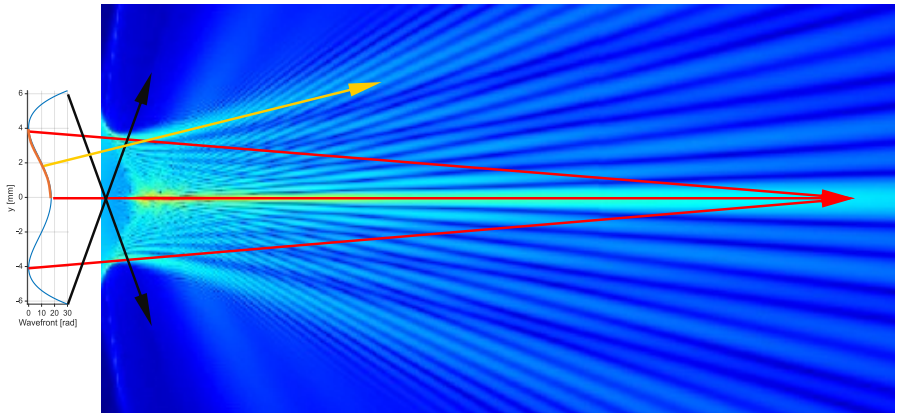


Figure 6.3: Longitudinal intensity profile of an SLB with an illustration of the rays originating from the diametral line-profile of the generating wavefront.

The intuition behind the generating principle can be gained by analyzing rays that originate in the locally perpendicular direction from various parts of the generating wavefront. These rays, representing light from separate regions of the generating wavefront, overlap as the beam propagates in space, as illustrated in Fig. 6.3. This means that the light from these regions interferes, resulting in the beam's structured pattern and pseudo-nondiffracting properties.

The superposition of overlapping rays leads to the formation of distinct beam regions during propagation. These regions are referred to as a near-field and diverging region (Fig. 6.2a). The rays originating from the generating wavefront part with the highest gradient of phase (black arrows) overlap first as the beam propagates,

contributing to the near-field region of the beam. Here, rapid changes in intensity patterns occur due to the overlapping of many rays, and the beam keeps its pseudo-nondiffracting behavior, such as regeneration behind the obstacle. The rays originating from the inflection point of this part of the wavefront (orange arrow) contribute to the outer ring in the case of the SLB, or to the outer line for the LB. The rays originating from the local extremes (red arrow) contribute to the creation of the inner core in the diverging region. In this region, the beam has a stable transversal intensity distribution that only linearly diverges with distance [110, 111, 114]. The orange part of the wavefront can be approximated using a cubic function, which gives rise to an Airy-like beam [110].

The similarity between LBs and DABs or SABs is evident. LBs are composed of Airy-like beams with opposing accelerating directions and exhibit the same reflection symmetry as SABs and DABs. SLBs are formed from Airy-like beams arranged with rotational symmetry, similar to that found in CABs. However, the angle between the Airy-like beams and their spacing is influenced by the shape of the generating wavefront. This is further described, together with the details describing the generation principle behind LBs, in the publication in the chapter 7.5 [114]. The generation principle and properties of SLBs are explained more thoroughly in the publications of Polák [110, 111].

6.2 Numerical Modeling

A dedicated simulation software was required to optimize SLBs and LBs propagation characteristics and, consequently, the beam generator itself. The motivation was to ensure that the beam maintains the spatial characteristics complying with the constraints of the alignment system, such as that the vital parts of the transversal intensity distribution fit on a CCD or CMOS detector and can be analyzed even after propagating for hundreds of meters.

At the initial stage of the research, the beam propagation was simulated using the commercial software VirtualLab Fusion [116]. This software utilizes ray tracing through the optical elements of the beam generator, resulting in an optical path difference and a density distribution of rays. These results are translated into a complex field that describes the amplitude and phase of the light. Numerical calculation combining diffraction integral or the Fourier optics approach is employed to propagate the complex field to a given distance, leveraging the Fast Fourier transformation (FFT) algorithm to numerically solve the equations [117].

Subsequently, an in-house software was developed in MATLAB [118]. This software follows the same simulation principles, but it is specifically optimized for simulating SLBs and LBs propagation. The optimization provides several advantages, such as greater control over the simulation parameters, which helps to decrease the time needed for performing the calculations. This software was used to simulate the beams presented in Fig. 6.2. Note that the simulation principles show good agreement with experiments as presented in the chapter 7.4 and additional publications [45, 63, 119].

One of the controllable parameters in the in-house developed software was the sampling rate, which is a vital parameter for the FFT algorithm. In this context, aliasing needs to be explained first. It arises when the sampling rate is insufficient to capture the high spatial frequencies present in the optical field. According to the Nyquist theorem, to avoid aliasing, the sampling interval must be at least twice the highest frequency component in the field, ensuring that all relevant spatial information is accurately represented in the resulting complex field in a given distance [120]. The spatial resolution Δx is inversely proportional to the product of matrix size M and sampling interval Δk:

$$\Delta x = \frac{1}{M \Delta k}. \tag{6.3}$$

When high spatial frequencies must be captured, the matrix size representing the complex scalar optical field can grow significantly, requiring efficient memory management. The computational complexity scales linearly for one-dimensional vectors, whereas it increases quadratically for two-dimensional matrices. For the LBs, given their symmetry, vector-based calculations are sufficient, reducing the dimensionality from matrix to vector operations, and exponentially decreasing memory requirements and computation time.

Additionally, the in-house software has the ability to simulate symmetry-breaking effects, which were introduced in the paper by Polák [121]. The symmetry breaking occurs when one or multiple apertures are present in the path of the beam. This can alter the beam's straightness due to diffraction effects, which need to be considered for alignment applications, as the shape of the alignment reference must be known. Compared to the approach presented in Polák's paper, the developed software features the ability to insert multiple apertures. This allowed for the optimization of aperture size for LB sensors described in the paper of chapter 7.6 [122].

6.3 Structured Laser Beams and Layer Beams in the Context of Alignment

To establish a reference line for alignment, it is necessary to measure the position of the SLB at multiple distances from the beam generator. The accuracy and precision of the detection algorithms were investigated on simulated transversal intensity distributions of SLBs and HSLBs in the paper of chapter 7.3 [113]. The algorithms for SLBs were also experimentally verified with the results presented in the conference proceedings of chapter 7.2 [62]. The results suggest that the algorithms will not be the main limiting factor or source of error in the alignment system.

However, the results presented in chapter 7.2 underline the need for propagating the beam inside a vacuum pipe to mitigate fluctuations and the gradient of refractive index in the propagation medium, as these can significantly affect the precision and accuracy of the alignment system. As a consequence of this finding, the research emphasis moved on to the next topic. It is evident that the generating wavefront is an important parameter that dictates the properties of the beam. Measuring this

wavefront while propagating inside the vacuum pipe can be problematic. One of the reasons can be, for example, space constraints. To solve this, a measurement technique for characterizing the generating wavefront based on a single image of the transversal intensity distribution of the SLB was developed. The results were presented in the paper of chapter 7.1 [123] and also in the proceedings of SPIE, Optomechanical Engineering 2023 held in San Diego, California, USA: "Wavefront Aberration Detection of a Structured Laser Beam Using Artificial Intelligence and Its Use for Alignment" [124]. The conference paper introduces the use of the method for detecting non-symmetric optical aberrations, which can be present in SLBs generated using, for example, an SLB generator with misaligned lenses. However, based on our experience, this is a limited case that is not relevant in real particle alignment scenarios, where the lenses of the SLB generator are carefully aligned to produce a well-defined beam. For this reason, this conference paper is not included as part of this thesis.

An SLB-based alignment system was tested and compared with the WPS and HLS, with the results presented in the paper by Niewiem [60]. In the paper, the SLB was propagated inside a vacuum pipe, where the pressure reached 10^{-2} mbar, which mitigated most of the unwanted atmospheric effects. The results of the relative alignment showed promising results with a standard deviation error of offset measurements below 20 µm over the length of 140 m. The alignment reference could not be measured simultaneously along the entire path of the beam. This arises when the central core of the SLB is obscured by a camera, as it is prevented from propagation and also from further position measurements. In the paper, this was addressed by introducing moving mechanical shutters, which briefly cover the beam while sequentially measuring the position of the alignment reference by inserting the CMOS chip in the path of the beam. However, this increased the time of the measurement. The paper discusses that this is one source of error, where the reference line shows a shift in time. This can be caused by the fact that the SLB generator was not inside the vacuum. Therefore, not all of the effects caused by the non-uniformity of the refractive index in the atmosphere were mitigated. Additionally, even a slight physical movement of the generator or instability of laser illumination can also introduce a similar error. Pellicle beam splitters can be used to mitigate this problem [125]. However, a slight wedge angle between the surfaces of the beam splitter can cause angular deviation of the beam over distances of hundreds of meters. This effect can be partly limited by calibration, however, it can spoil the straightness and quality of the reference line.

We propose to address this challenge by moving away from SLBs, or any other beam with rotational symmetry, to LBs. LBs generate a reference plane, which is enabled by the reflection symmetry of the transversal intensity distribution along the entire path of the beam, instead of a reference line generated by the SLB. This is illustrated in Fig. 3 of the paper in the chapter 7.6 [122]. In the proposed solution, LBs provide the basis for an orthogonal alignment reference given by two reference planes. This is established by two LBs rotated by 90 degrees, as is illustrated in Figs. 4 and 6 of the paper presented in the chapter 7.6 [122]. The reference planes along both axes are detected using a hollow sensor, developed specifically

for this task. This sensor is composed of four linear CCD sensors placed around a square aperture, as can be seen in Fig. 5 of the publication included in chapter 7.6 [122]). The aperture allows the beam to propagate further, without fully obstructing it. Furthermore, a roll misalignment can be measured using this system, adding an additional degree of freedom. The analysis of the developed system in comparison with a laser tracker measurement is described over the distance of 2 m (chapter 7.6 [122]). The detection algorithm for the detection of the reference plane was introduced in the conference paper in the chapter 7.4 [119]. The detection algorithms were also presented in the conference proceedings: "Layer Beams and Their Prospect for Long-Range Alignment" [63], which is not part of this thesis. This proceeding also discusses the influence of reflections inside the vacuum pipe on the LB signal-to-noise ratio.

Another critical consideration in an alignment system's development is the environment of the particle accelerator in which the alignment sensors operate. High-energy radiation can degrade electronic components over time, potentially compromising the reliability of the system, destroying the electronics, and increasing the costs. To address this challenge, a signal transmission system based on an optical fiber matrix was tested as a potential solution. This approach would allow the signal to be guided away from the radiation area while keeping the electronics shielded from direct radiation exposure. The feasibility of this technique was also presented in the paper in the chapter 7.6 [122].

7 Collection of Papers

This chapter presents results as a collection of six publications, including four peer-reviewed journal articles and two conference papers. The first three publications focus on the methods developed for SLBs, while the additional three shift the focus to the LBs. It is obvious that the focus of the research shifted towards LBs. Based on the aforementioned findings of this research, it became evident that LBs could provide additional benefits to the alignment system compared to SLBs. However, if needed, the methods developed for SLBs can, after a slight alteration, also be used for LBs. Note that the abbreviations used in the publications can differ from those in the thesis. A distinction was made in the chapter that contains a list of abbreviations to facilitate reading.

7.1 Wavefront Reconstruction of a Non-Diffracting Structured Laser Beam

This paper introduces a novel technique for estimating wavefronts of SLBs. The study introduces an approach combining artificial intelligence with least-squares fitting to determine symmetrical wavefront aberrations. By analyzing a single SLB transversal intensity distribution, the method estimates symmetrical coefficients of Zernike polynomials of the generating wavefront, namely the defocus and different orders of spherical aberrations. Results are compared to the measurements obtained using a Shack-Hartmann sensor [126]. The advantage of this approach is that the generating wavefront estimation is enabled even in difficult conditions, such as when the beam propagates inside a vacuum, where it can be difficult to insert a wavefront sensor. The paper was published in Optics Express (Q2, Impact Factor = 3.2).

Research Article | Vol. 31, No. 25 / 4 Dec 2023 / Optics Express 42099
Optics EXPRESS

Wavefront reconstruction of a non-diffracting structured laser beam

MARTIN DUSEK,[1,2,*] JEAN-CHRISTOPHE GAYDE,[1] AND MIROSLAV SULC[2,3]

[1]The European Organization for Nuclear Research (CERN), Geneva, Switzerland
[2]Technical University of Liberec (TUL), Liberec, Czech Republic
[3]Institute of Plasma Physics of the Czech Academy of Sciences (IPP CAS), Prague, Czech Republic
[*]martin.dusek@cern.ch

Abstract: The Structured Laser Beam (SLB) is a pseudo-non-diffracting laser beam that shares many characteristics with a Bessel beam. However, it can theoretically propagate over an unlimited distance while maintaining an extremely low inner core divergence of only 0.01 mrad. This makes it a promising candidate for precise long-distance alignment applications such as the alignment of particle accelerator components at CERN. In this work, a novel method to assess the symmetrical wavefront aberrations induced by an SLB generator is presented. Our approach is based on the analysis of a single-intensity distribution of an SLB. The coefficients of the Zernike polynomials are estimated using artificial intelligence before least-squares fitting is used to refine the result. This approach ensures that the fitting avoids local minima. This method provides a novel way to analyze the optical aberrations induced by the SLB generator.

Published by Optica Publishing Group under the terms of the Creative Commons Attribution 4.0 License. Further distribution of this work must maintain attribution to the author(s) and the published article's title, journal citation, and DOI.

1. Introduction

Accurately aligning accelerator components over long distances poses a significant challenge, requiring precision of the transversal position in the range of tens of micrometers over distances of hundreds of meters. At CERN, straight-line reference systems have been developed to meet these stringent accuracy requirements [1]. These systems, such as the Wire Positioning System and Hydrostatic Leveling System, use physical references, in these cases stretched wires and water levels, respectively. While highly precise, they suffer from implementation difficulties and component costs and are difficult to scale to even larger accelerators. An optical-based system could serve as a viable alternative for future colliders like the Compact Linear Collider (CLIC) [2] or the Future Circular Collider (FCC) [3], which are currently under study at CERN. These projects require tight alignment tolerances in the transversal direction, with an accuracy of up to 10 μm (1σ) over a 200 m span [4]. Several optical-based systems for aligning structures over long distances have been proposed in various works [4–9], however, the drawback of these systems is their relatively high divergence, which makes it challenging to achieve accurate straight-line reference measurements over long distances.

A promising candidate to overcome this drawback is the Structured Laser Beam (SLB) [10]. The SLB is a pseudo-non-diffracting beam with a transversal intensity profile similar to a Bessel Beam (BB) of zeroth order [11,12]. It shares certain properties with the BB, such as a low divergence of the central core compared to a Gaussian Beam (GB) and the ability for regeneration behind obstacles [13]. Various reports have explored the use of pseudo-non-diffracting beams for alignment purposes. Parks [14–17] used BB for aligning optical elements, while Gale [18] employed projected BB for aligning larger structures over 19 m. However, contrary to a BB, the SLB maintains a well-defined central core that can fit on a reasonably sized sensor chip even after propagating for several hundred meters. Propagation tests up to 900 m have been conducted at

#502452 https://doi.org/10.1364/OE.502452
Journal © 2023 Received 25 Aug 2023; revised 15 Oct 2023; accepted 16 Oct 2023; published 29 Nov 2023

Optics EXPRESS

CERN, yielding a divergence of under 0.01 mrad. This enables direct reading of the SLB image using a reasonably sized camera chip even after propagation over hundreds of meters.

The generation principle for an SLB relies on utilizing the symmetrical optical aberrations, namely defocus and spherical aberrations, and is described in detail in subsequent sections. It is crucial to know the values of the defocus and spherical aberrations to determine SLB properties. Some studies have addressed the issue of aberrated BBs produced by oblique illumination of an axicon or a diffracting element [19–21]. Dudutis [22] demonstrated the use of these aberrated beams for glass dicing. Khonina presented a method for analyzing astigmatic BBs to detect birefringence of gradient-index lenses and crystals [23,24] and presented a way to analyze the intensity distribution of optical aberrations for a combination of an axicon and bi-convex lens [25]. Miao [26] proposed a technique for phase front retrieval and correction of a BB. However, none of these works presented a fast and reliable method for assessing wavefront aberrations in beams generated solely by symmetrical optical aberrations, such as an SLB.

To evaluate the wavefront shape, traditional wavefront sensing methods can be employed. However, this approach can be problematic since the wavefront should be measured directly behind the projection lens. In the context of long-distance alignment applications, the SLB propagates within a vacuum pipe, making it challenging to directly measure the wavefront immediately behind the generator. The considerable diameter of the generator projection lens can also introduce complexities in measurements using conventional wavefront sensing methods. This paper presents a simple method for estimating the wavefront of an SLB utilizing a combination of a convolutional neural network (CNN) and least-square fitting. While there have been reports of using artificial intelligence (AI) for detecting wavefront aberrations [27–29], to the best of our knowledge, AI has not been employed for wavefront analysis of non-diffracting beams. This method enables the determination of the SLB dominant symmetrical wavefront aberrations using a single SLB intensity distribution, with application to high-precision, long-distance alignment, where it can provide information about the beam properties.

2. Methodology

The SLB can be generated using various generators that create a uniquely shaped wavefront by combining rotationally symmetrical aberrations: spherical aberration, secondary spherical aberration and defocus. Such an optical system functions as a Keplerian beam expander, maintaining the nearly parallel nature of both input and output beams while introducing a phase delay. This phase delay results in a distinctive wavefront shape. It is important to note that this wavefront is formed directly behind the projection lens, as depicted in Fig. 1. As one moves farther from the generator along the direction of SLB propagation, various segments of the wavefront undergo constructive and destructive interference, resulting in an intensity distribution resembling that of a Bessel Beam. However, in the case of SLB, there is a radial intensity modulation of the beam's rings. The shape of the wavefront directly influences beam properties, including the core size, the number of rings, and their intensity modulation. A critical parameter in this context is the so-called zero-phase gradient ring, depicted in Fig. 2, which can be utilized to determine the central core size [30].

An SLB can be generated using a variety of generators. In this work, a 5 mm ball lens made of N-BK7 glass is used in combination with a plano-convex projection lens. The projection lens is made of N-BK7 glass with a diameter of 9 mm and a radius of curvature of 10.3 mm. By changing the distance between the lenses, denoted as L_{PL} in the interval L_{PLMIN} to L_{PLMAX}, the diameter of the zero-phase gradient ring is changed, affecting the core size as illustrated in Fig. 2.

The values of L_{PLMIN} and L_{PLMAX} were equal to 18.8 and 19.25 mm respectively. This interval of values ensures that the SLB pattern can fit into a 10x10 mm region of interest on a Basler camera acA4112-30uc featuring a CMOS chip measuring 14.13x10.35 mm placed 1.5 m away from the generator. The limitations of our experimental setup defined this constraint. The shorter

Optics EXPRESS

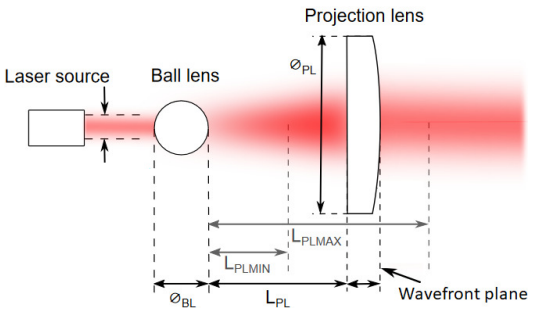


Fig. 1. Schematic of an SLB generator.

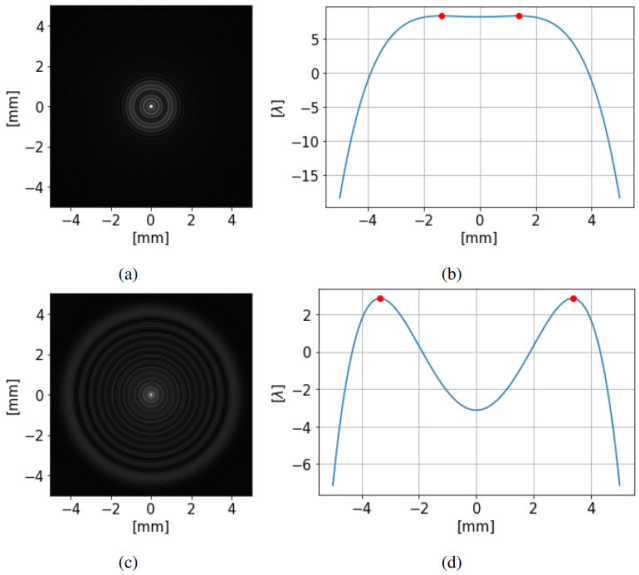


Fig. 2. Simulated intensity distributions and corresponding line profiles using Eq. (3) traced to z = 1.5 m. (a) c_j values corresponding to L_{PLMAX} producing a core size of 0.26 mm (b) the corresponding wavefront profile. The zero-phase gradient ring is highlighted by red dots having a diameter of 2.81 mm. (c) c_j values corresponding to L_{PLMIN} producing a core size of 0.16 mm (d) the corresponding wavefront profile. The zero-phase gradient ring is highlighted by red dots having a diameter of 6.6 mm.

Optics EXPRESS

L_{PL} reduces the amount of defocus aberration in the wavefront. This affects the size of the zero-phase gradient ring diameter, which becomes larger. The SLB with a relatively small core size is created as a result at a certain distance. Other parameters, such as the number of rings and divergence, are also affected by the change of the L_{PL} distance. This generation principle allows for fast and easy tuning of the SLB core size and other parameters. More details about the generation principle can be found in our previous works [10,30,31] and in the paper of Herman [32].

A method that analyses a single transversal intensity distribution to estimate the shape of the wavefront directly behind the projection lens was proposed. The phase of the complex field behind the projection lens, hence the wavefront shape, can be described using normalized Zernike polynomials [33]. Zernike polynomials are described by Z_j and their respective coefficients c_j, The Noll indexing was used [34].

To validate the method, results were compared with measured data obtained from a Shack-Hartmann sensor (SHS). The SHS was placed as close as physically possible in front of the projection lens to measure the wavefront in the plane directly behind the projection lens. The SHS consisted of a microlens array MLA300-14AR from Thorlabs combined with a Basler camera a2A5328-15umPRO. The wavefront shape and phase were calculated using in-house software [35].

Equation (1) describes the complex field of a non-aberrated SLB, which is approximated using only defocus and spherical aberrations with index j equal to 4, 11, and 22, respectively.

$$s(x_0, y_0, 0) = S_0 exp[i2\pi(c_4 Z_4 + c_{11} Z_{11} + c_{22} Z_{22})] \tag{1}$$

Equation (2) describes a situation where other aberrations that do not contribute to the creation of a beam are present, represented as the sum of the j-number of Zernike polynomials in the complex field. These aberrations can have unwanted influence on the intensity distribution symmetry.

$$g(x_0, y_0, 0) = G_0 exp(i2\pi \sum_j c_j Z_j); j \notin \{4, 11, 22\} \tag{2}$$

If the complex field is known, a diffraction integral can be employed to propagate the field and reconstruct the transversal intensity distribution $U(x, y, z)$ at an arbitrary distance z as described by Eq. (3). In this equation, k represents the angular wavenumber and λ the wavelength of light.

$$U(x, y, z) = \frac{1}{i\lambda z} exp(ikz) exp[\frac{ik(x^2 + y^2)}{2z}] FT\{s(x_0, y_0, 0) g(x_0, y_0, 0) exp[(x_0^2 + y_0^2)\frac{ik}{2z}]\} \tag{3}$$

The method presented here deals with the inverse task. The intensity distribution $I(x, y)$ of the SLB is measured using a CMOS chip at a given distance from the projection lens. This measurement serves as input for a non-linear-least-squares minimization of the c_4, c_{11} and c_{22} values to match the measured intensity distribution $I(x, y)$ at a given distance z according to the Eq. (4) [26]. We assume $g(x_0, y_0, 0) = 0$ for the fitting process. This estimation is allowed by the fact that, in reality, the values of aberrations expressed by $g(x_0, y_0, 0)$ are small. This will become evident in the following chapters. $S_0 = 1$ was also assumed.

$$S = \min_{c_4, c_{11}, c_{22}} \sum_x \sum_y [U(x, y, z) - I(x, y)]^2 \tag{4}$$

When the minimization process begins with coefficient values equal to zero or random values, the fitting process becomes trapped in a local minimum, failing to determine the values of the polynomials even for least-squares fitting with fine-tuned parameters. To mitigate this issue, a convolutional neural network (CNN) was employed to obtain the initial estimates for the c_4, c_{11}

Optics EXPRESS

and c_{22} values.

$$RMSE_{wf} = [\sum_{j}(c_j Z_j)^2]^{1/2} \tag{5}$$

DenseNet121, InceptionV3, and Resnet-50 architectures were trained to estimate the coefficient values. Detailed architectural schemes are provided in additional materials. An input of the networks was a 224x224x3 intensity distribution of the SLB represented as an RGB image. An output linear dense layer provided values for the matrix of the three symmetrical coefficients of the Zernike polynomials. Models were trained using a dataset of 100,000 simulated transversal intensity distributions of the SLB, which were generated using Eq. (3) traced up to 1.5 m.

The ranges of c_j of values used in Eq. (1) and (2) for the generation of the training data were obtained from multiple measurements of SLB wavefronts in the interval L_{PLMIN} and L_{PLMAX} using a well-aligned generator and the SHS. These measurements are presented in the following chapter. The wavefront root-mean-squared error ($RMSE_{wf}$) was calculated using Eq. (5) up to j = 66, excluding piston (c_1), tilts (c_2, c_3), and defocus (c_4) and spherical aberrations (c_{11}, c_{22}), to be in an interval of 0.06 to 0.08λ. The wavefront, therefore, can be approximated by Eq. (1) without significantly affecting the calculation of the zero-phase gradient ring. This is true for most of the generators, such as the ones presented in [30]. One has to be careful when short focal length distance lenses are used as a SLB generator. As a generator consisting of two 5 mm high index ball lenses, the system can be more prone to misalignment and cause a larger influence of non-symmetrical aberrations on the intensity pattern.

Equation (2) was used as noise together with a Gaussian intensity noise with mean zero and variance equal to 1e-7. The amplitude $S_0 = 1$ was assumed. The c_j value intervals in units of [λ] used for training can be seen in Table 1. Note that though the magnitude of the c_{22} is small, it has an important effect on the beam properties due to its symmetry and, therefore, must be used for the description of the SLB wavefront.

Table 1. Interval of c_j values used for training dataset simulations.

Coefficient c_j	[λ]
$j = 1$	0
$j = 4$	[-7.85; -1.25]
$j = 11$	[-2.55; -2.45]
$j = 22$	[-0.07; -0.08]
$j \in [2, 66] \setminus \{4, 11, 22\}$	[-0.02; 0.02]

The dataset was divided into 80,000 images for testing and 20,000 images for validation. The input images were normalized min-to-max in the interval of [0, 1] to mitigate the influence of intensity, and a square root stretching operation was applied to enhance the shape features. An Adam optimizer using a learning rate 1e-3 was used and halved every 15 epochs down to a minimum value of 5e-6. The batch size was set to 32 using 300 epochs for training. The mean-squared error (MSE) of the c_4, c_{11} and c_{22} values served as the learning metric. The change of a loss function MSE during the training process can be seen in Fig. 3.

InceptionV3 consistently achieved stable validation loss function MSE values, converging to the order of 1e-5. ResNet50 and DenseNet121 exhibited stable validation loss function MSE values in the lower order of 1e-4. To assess the performance of the trained networks, we conducted a reconstruction experiment involving 1,000 wavefronts using simulated data that were not part of the training set. We compared the predicted wavefronts with a reference wavefront by calculating the difference in $RMSE_{wf}$ values. This involved subtracting two sets of coefficient values representing the predicted and reference wavefronts for j in the interval of 4 to 66. This means that the values of $RMSE_{wf}$ were largely influenced by the aberrations introduced by Eq. (2),

Optics EXPRESS

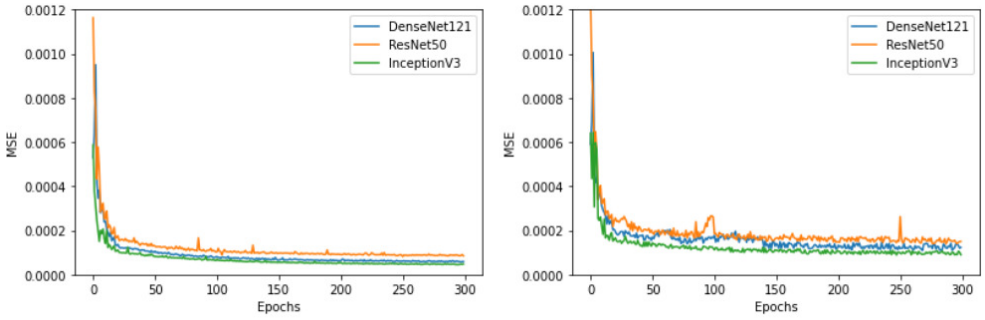


Fig. 3. Loss function changing process of different networks. (a) Training process (b) Validation process. For detailed architectures of ResNet50, InceptionV3, and DenseNet121 see Visualization 1, Visualization 2, and Visualization 3, respectively.

which were not estimated by the AI. The mean values and error bars indicating the standard deviation are presented in Fig. 4. Notably, InceptionV3 outperformed the other architectures, achieving an RMSE of 0.054λ. In contrast, the RMSE values for ResNet50 and DenseNet121 architectures are 0.104λ and 0.096λ, respectively. Consequently, we have selected InceptionV3 for subsequent reconstructions.

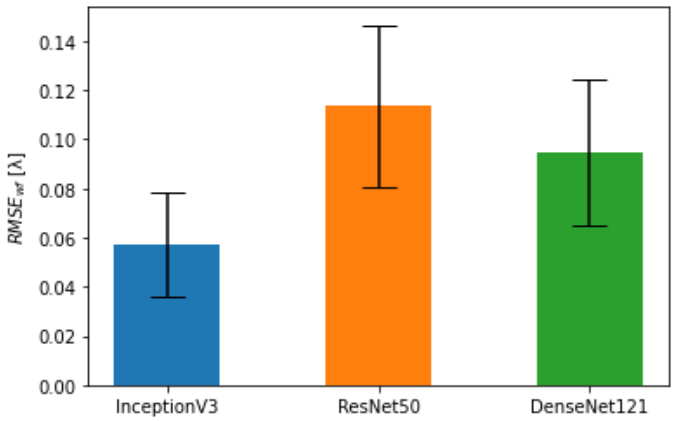


Fig. 4. Mean $RMSE_{wf}$ values of the difference between the reference and predicted wavefront. Error bars represent the standard deviation.

3. Results

3.1. Simulation

The method was validated by reconstructing the wavefront of a simulated intensity distribution with known values of the c_4, c_{11} and c_{22} that were not utilized during the training. Data were generated using the same procedure as for the training data.

The simulated reference intensity distribution, AI estimation followed by the fitting process can be seen in Fig. 5(a), Fig. 5(b) and Fig. 5(c) respectively. The wavefront residual, which represents the difference between the reference wavefront and the wavefront obtained after the fitting, is depicted in Fig. 5(d). For comparative analysis of the c_4, c_{11} and c_{22} the coefficient values can be

Optics EXPRESS

seen in Fig. 5(e). The layout presented in this figure is replicated in subsequent figures, each showcasing additional wavefront reconstructions. The $RMSE_{wf}$ values were calculated for the coefficients in the interval from 4 to 66, excluding piston and tilts.

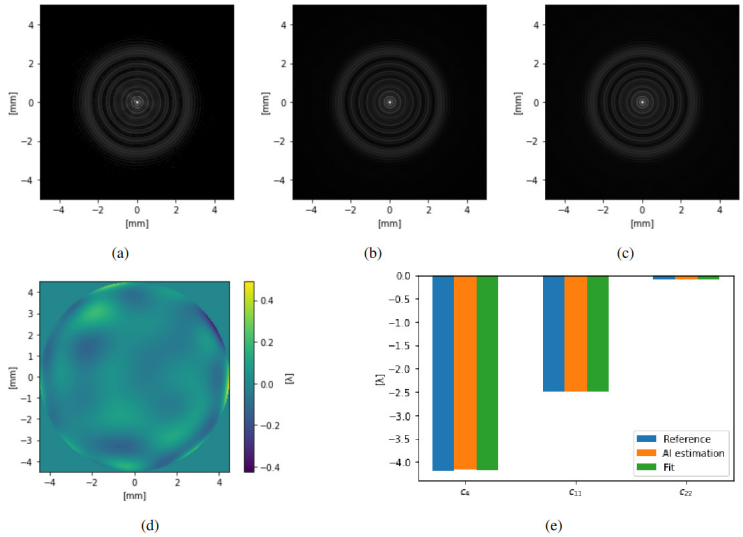


Fig. 5. Validation of the method using simulated data. The square root stretching was used to enhance the features in the intensity distributions. (a) Reference simulated intensity distribution (b) Intensity distribution estimated by artificial intelligence (AI) (c) Intensity distribution obtained through fitting (d) Wavefront residual representing the difference between the reference and fitted wavefront (e) c_j values of reference, AI estimation and fitting for defocus, spherical and secondary spherical aberration

In the measurement displayed in Fig. 5, the percent error for the reference symmetrical coefficients c_4, c_{11} and c_{22} is equal to 0.64% going down to 0.14% after fitting. The $RMSE_{wf}$ between the reference and the fitting process stands at 0.057λ after including the error of the non-symmetrical coefficients up to c_{66}. The peak-to-valley (PV) wavefront difference between the initially generated reference and the wavefront obtained through fitting measures at 0.89λ.

The percent errors in the measurement presented in Fig. 6 are equal to 0.38% and 0.37% for prediction and fitting respectively. The $RMSE_{wf}$ is equal to 0.077λ after fitting. The peak-to-valley (PV) wavefront difference is measured to be 0.74λ.

The method has been effectively applied to data that were not part of the training dataset. Fitting reduces the error of the AI estimation even when only the c_4, c_{11} and c_{22} are the subject of change. As a result, the coefficients used to generate the SLB are estimated with slightly higher accuracy. Using AI estimation alone is up for consideration, reducing the method's runtime from seconds to milliseconds without significantly sacrificing accuracy. The main major portion of the $RMSE_{wf}$ are the aberrations induced by Eq. (2).

3.2. Experiments

Wavefronts of several SLBs were measured using the SHS sensor and taken as a reference. The intensity distributions were measured using the camera placed 1.5 m away from the generator. The images were taken with low exposure values in order. Hence, pixels are not saturated. The image was cut to have a size 10x10 mm, and the resolution was lowered to match the input size of the InceptionV3 network. Two laser source with a wavelength of 532 nm and power of 0.9 mW

Optics EXPRESS

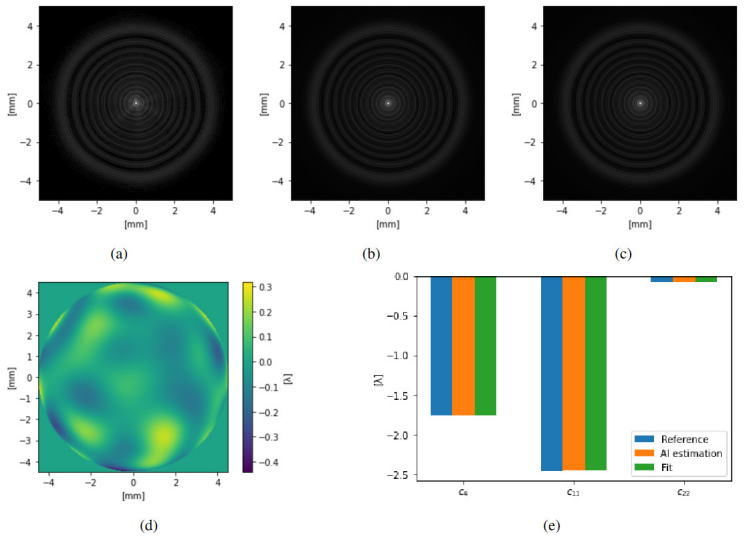


Fig. 6. Validation of the method using simulated data. The square root stretching was used to enhance the features in the intensity distributions. (a) Reference simulated intensity distribution (b) Intensity distribution estimated by artificial intelligence (AI) (c) Intensity distribution obtained through fitting (d) Wavefront residual representing the difference between the reference and fitted wavefront (e) c_j values of reference, AI estimation and fitting for defocus, spherical and secondary spherical aberration

was used for measurements in Figs. 7 and 8. For measurements in Figs. 9 and 10, a laser source with a power of 4.5 mW with a wavelength of 532 nm was used.

In the wavefront estimation depicted in Fig. 7 the percent error for the reference symmetrical coefficients c_4, c_{11} and c_{22} is equal to 0.57% going down to 0.45% after fitting. The $RMSE_{wf}$ equals to 0.088λ after fitting. Simultaneously, the peak-to-valley (PV) wavefront difference between the initially generated reference and the wavefront obtained through fitting measures at 1.15λ.

In the measurement presented in Fig. 8, the $RMSE_{wf}$ stands at 0.081λ after fitting. The percent error of the defocus and spherical aberrations is equal to 0.24% and 0.15% for AI prediction and fitting, respectively. The PV wavefront difference between the generated reference and the wavefront was obtained through fitting measures at 0.88λ.

Experiments effectively demonstrate the method's utility in estimating the wavefront of an SLB, specifically the coefficients c_4, c_{11}, and c_{22}. Notably, despite the AI model being trained on a simulated dataset, it proves to be highly effective when applied to real measurements.

In the measurement presented in Fig. 9, the $RMSE_{wf}$ is equal to 0.085λ after fitting. The percent errors of the c_4, c_{11} and c_{22} for the AI estimation is equal to 1.47% and 0.52% for the fitting. The peak-to-valley (PV) wavefront difference between the initially generated reference and the wavefront obtained through fitting measures at 1.12λ.

In the wavefront estimation shown in Fig. 10, the percent error of the AI estimation is equal to 1.45% decreasing down to 0.12% after using the fitting. The $RMSE_{wf}$ stands at 0.082λ after using the fitting process. Simultaneously, the peak-to-valley (PV) wavefront difference between the initially generated reference and the wavefront obtained through fitting measures at 0.92λ.

An increase in the reconstruction error for the coefficients c_4, c_{11}, and c_{22} of the AI estimation is apparent for both measurements in Figs. 9 and 10. This increase could be attributed to the utilization of a different laser source with higher power and a distinct spatial illumination

Optics EXPRESS

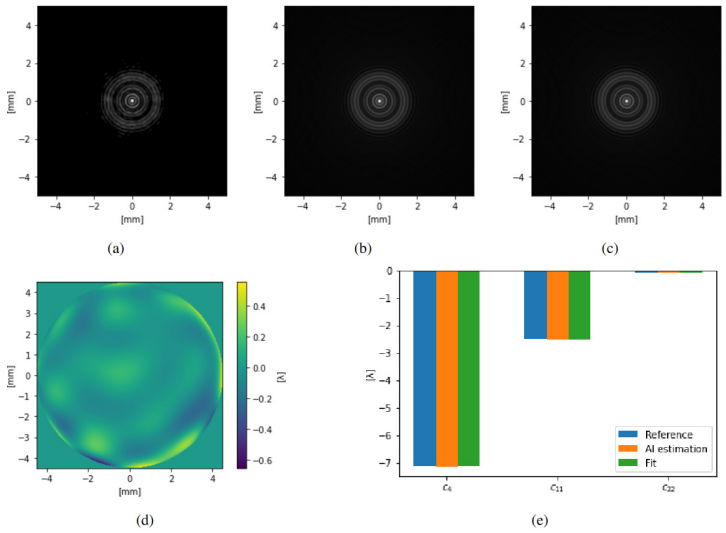


Fig. 7. Validation of the method using a comparison with a SHS wavefront measurement. The square root stretching was used to enhance the features in the intensity distributions. (a) Measured intensity distribution (b) Intensity distribution estimated by artificial intelligence (AI) (c) Intensity distribution obtained through fitting (d) Wavefront residual representing the difference between the reference and fitted wavefront (e) c_j values of measured reference, AI estimation and fitting for defocus, spherical and secondary spherical aberration

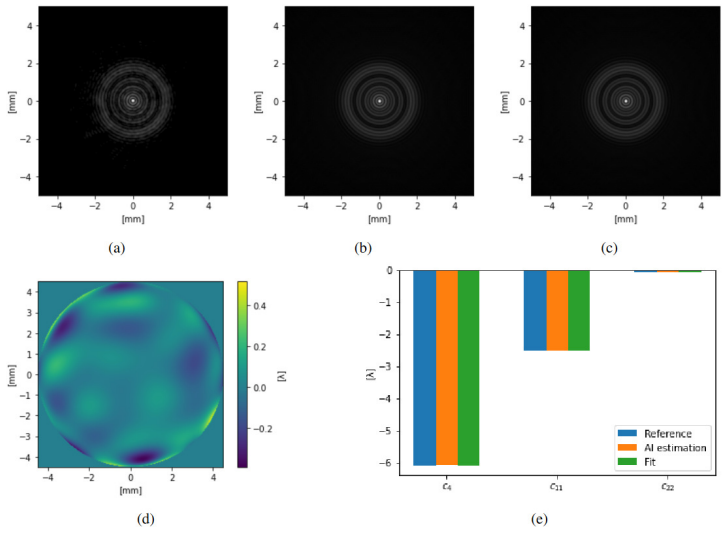


Fig. 8. Validation of the method using a comparison with a SHS wavefront measurement. The square root stretching was used to enhance the features in the intensity distributions. (a) Measured intensity distribution (b) Intensity distribution estimated by artificial intelligence (AI) (c) Intensity distribution obtained through fitting (d) Wavefront residual representing the difference between the reference and fitted wavefront (e) c_j values of measured reference, AI estimation and fitting for defocus, spherical and secondary spherical aberration

Optics EXPRESS

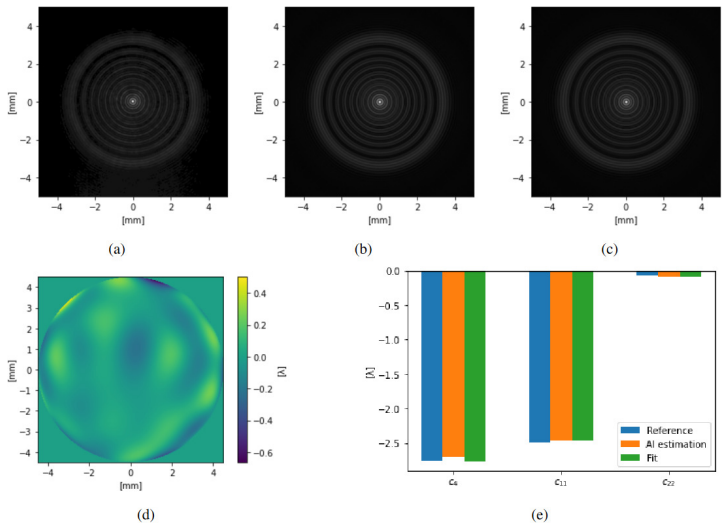


Fig. 9. Validation of the method using a comparison with a SHS wavefront measurement. The square root stretching was used to enhance the features in the intensity distributions. (a) Measured intensity distribution (b) Intensity distribution estimated by artificial intelligence (AI) (c) Intensity distribution obtained through fitting (d) Wavefront residual representing the difference between the reference and fitted wavefront (e) c_j values of measured reference, AI estimation and fitting for defocus, spherical and secondary spherical aberration

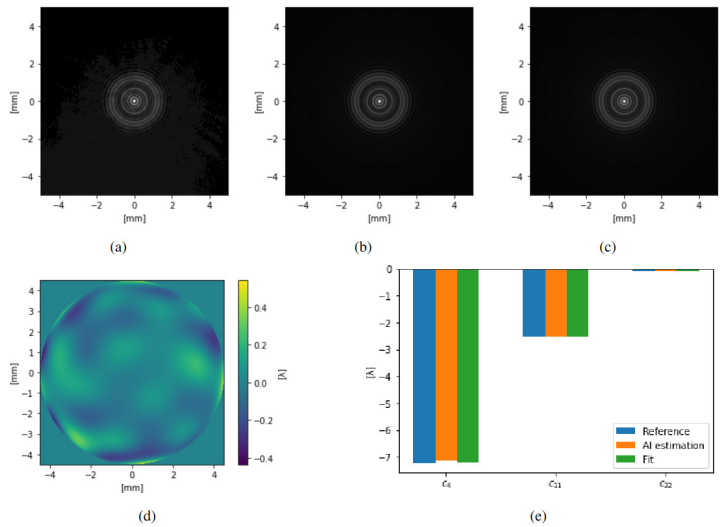


Fig. 10. Validation of the method using a comparison with a SHS wavefront measurement. The square root stretching was used to enhance the features in the intensity distributions. (a) Measured intensity distribution (b) Intensity distribution estimated by artificial intelligence (AI) (c) Intensity distribution obtained through fitting (d) Wavefront residual representing the difference between the reference and fitted wavefront (e) c_j values of measured reference, AI estimation and fitting for defocus, spherical and secondary spherical aberration

Optics EXPRESS

distribution than for the previous measurements. After closely examining the figures, a stray light outside of the SLB's outer ring can be seen. This can cause an increase in the AI estimation error.

If we compare the reconstructed and measured reference wavefronts from the experiments, the zero-phase gradient ring can be calculated with an error of less than 10 μm for all of the presented reconstructions.

4. Discussion

The results obtained from this study show the advantage of using AI combined with least-squares fitting to estimate the SLB wavefront, and its characteristics, using symmetrical defocus (c_4) and spherical aberrations (c_{11}, c_{22}) with a root-mean-squared error of the wavefront estimation being smaller than 0.09λ. This approximation by symmetrical aberrations is enabled by the fact that non-symmetrical aberrations in the SLB wavefront have low magnitudes, considering the SLB generators used in long-distance alignment. Note that using lenses with shorter focal lengths can cause the generator to be susceptible to misalignment and to the effect of non-symmetrical aberrations.

While the AI estimation of the Zernike polynomial coefficients alone demonstrates satisfactory results, the switch to a different laser source decreased the accuracy of the AI estimation. The AI performance could be improved by increasing the number of samples used for training or possibly by incorporating an illumination distribution change into the training dataset generation process. Training on real data could improve the results. However, this process can be labor-intensive for large datasets. The subsequent least-squares fitting process generally refines the estimation of these coefficients, leading to higher precision. The trade-off between the accuracy gain and time span of the method needs to be considered when it comes to the use of the fitting, which can be rendered unnecessary. Importantly, despite being trained on simulated data, the CNN was successfully applied to measured data from the laboratory, with results aligning with the SHS measurements.

By accurately estimating the wavefront, describing it using the dominant defocus and spherical aberrations produced by the SLB generator, it becomes feasible to determine the beam properties. Notably, the zero-phase gradient ring, which affects the size of the SLB core. This assessment will be beneficial for ensuring beam quality in precision-demanding applications such as long-distance accelerator alignment. The simulation approach employed in this study allows to generate non-diffracting beams through aberrations and can offer a straightforward means to obtain a desired beam shape through the manipulation of the induced aberrations.

Funding. CERN.

Acknowledgments. The authors acknowledge the financial support provided by the Knowledge Transfer group at CERN through the KT Fund. Portions of this work were presented at the conference SPIE Optomechanical Engineering 2023, Wavefront aberration detection of a Structured Laser Beam using artificial intelligence and its application in alignment.

Disclosures. The authors declare no conflicts of interest.

Data availability. Data underlying the results presented in this paper are not publicly available at this time but may be obtained from the authors upon reasonable request.

References

1. H. Durand Mainaud, S. B. Jimenez, T. Dijoud, M. Duquenne, A. Herty, and K. Kucel, "HL-LHC alignment requirements and associated solutions," in *Proceedings 8th Int. Particle Accelerator Conference (IPAC'17)*, (2017), pp. 1893–1896.
2. CERN, "The Compact Linear Collider (CLIC)," https://home.cern/science/accelerators/compact-linear-collider.
3. FCC collaboration, others, "FCC-ee: the lepton collider: future circular collider conceptual design report volume 2," Eur. Phys. J. Spec. Top. **228**(2), 261–623 (2019).
4. G. Stern, "Study and development of a laser based alignment system for the compact linear collider," Ph.D. thesis, ETH Zurich (2016).

Optics EXPRESS

5. T. Suwada, M. Satoh, S. Telada, and K. Minoshima, "Propagation and stability characteristics of a 500-m-long laser-based fiducial line for high-precision alignment of long-distance linear accelerators," Rev. Sci. Instrum. **84**(9), 093302 (2013).
6. L. V. Griffith, R. F. Schenz, and G. E. Sommargren, "Magnetic alignment and the poisson alignment reference system," Rev. Sci. Instrum. **61**(8), 2138–2154 (1990).
7. D. Kaemtner and J. Prenting, "Straight Line Reference System (SLRS) for the Adjustment of the X-ray Free-electron Laser (XFEL) at DESY," in *Proceedings of the 9th International Workshop on Accelerator Alignment (IWAA)*, Stanford Linear Accelerator Center (SLAC), California, United States, (2006).
8. M. Beker, G. Bobbink, B. Bouwens, *et al.*, "The rasnik 3-point optical alignment system," J. Instrum. **14**(08), P08010 (2019).
9. C. Zhang, M. Hasegawa, K. Kanda, and T. Shinomoto, "Performance of the iris diaphragm laser alignment system of the SPring-8," in *Proceedings of 13th Int. Workshop on Accelerator Alignment (Beijing, China)*, (2014).
10. J. Gayde and M. Sulc, "An optical system for producing a structured beam," EP3564734 (2019).
11. J. Durmin, "Exact solutions for nondiffracting beams," J. Opt. Soc. Am. A **4**(4), 651–654 (1987).
12. J. Durnin, J. Miceli, and J. H. Eberly, "Comparison of bessel and gaussian beams," Opt. Lett. **13**(2), 79–80 (1988).
13. Y. Shen, S. Pidishety, I. Nape, and A. Dudley, "Self-healing of structured light: a review," J. Opt. **24**(10), 103001 (2022).
14. R. Parks, "Alignment using axicon plane gratings," Proc. SPIE **10747**, 1074703 (2018).
15. R. E. Parks, "Aligning reflecting optics with bessel beams," Proc. SPIE **11488**, 114880J (2020).
16. R. E. Parks, "Practical considerations for using grating produced bessel beams for alignment purposes," Proc. SPIE **11816**, 1181603 (2021).
17. R. E. Parks, "Rapid centering of optics," Proc. SPIE **11889**, 118890V (2021).
18. D. M. Gale, "Visual alignment of mechanical structures using a bessel beam datum: practical implementation," Proc. SPIE **8082**, 80823D (2011).
19. S. N. Khonina, V. V. Kotlyar, V. A. Soifer, *et al.*, "Astigmatic bessel laser beams," J. Modern Opt. **51**(5), 677–686 (2004).
20. H. Cheng, C. Xia, S. M. Kuebler, *et al.*, "Aberration correction for slm-generated bessel beams propagating through tilted interfaces," Opt. Commun. **475**, 126213 (2020).
21. R. Dwivedi, P. Sharma, V. Kumar, *et al.*, "Axicon aberration leading to short-range nondiverging optical array and elliptical dark hollow beam," Opt. Eng. **57**(5), 055106 (2018).
22. J. Dudutis, R. Stonys, G. Račiukaitis, *et al.*, "Glass dicing with elliptical bessel beam," Opt. Laser Technol. **111**, 331–337 (2019).
23. S. N. Khonina, V. D. Paranin, A. V. Ustinov, *et al.*, "Astigmatic transformation of bessel beams in a uniaxial crystal," Opt. Appl. **46**, 5–18 (2016).
24. S. N. Khonina, S. V. Karpeev, and V. D. Paranin, "Birefringence detection of a gradient-index lens based on astigmatic transformation of a bessel beam," Optik **164**, 679–685 (2018).
25. S. N. Khonina, N. L. Kazanskiy, P. A. Khorin, *et al.*, "Modern types of axicons: New functions and applications," Sensors **21**(19), 6690 (2021).
26. B. Miao, L. Feder, J. E. Shrock, *et al.*, "Phase front retrieval and correction of bessel beams," Opt. Express **30**(7), 11360–11371 (2022).
27. G. Allan, I. Kang, E. S. Douglas, G. Barbastathis, and K. Cahoy, "Deep residual learning for low-order wavefront sensing in high-contrast imaging systems," Opt. Express **28**(18), 26267–26283 (2020).
28. S. W. Paine and J. R. Fienup, "Machine learning for improved image-based wavefront sensing," Opt. Lett. **43**(6), 1235–1238 (2018).
29. Y. Nishizaki, M. Valdivia, R. Horisaki, *et al.*, "Deep learning wavefront sensing," Opt. Express **27**(1), 240–251 (2019).
30. W. Niewiem, K. Polak, M. Dusek, D. Mergelkuhl, J.-C. Gayde, A. Wieser, and M. Sulc, "Variation of structured laser beam pattern and optimization for an alignment reference line creation," Optics Express (to be published) (2023).
31. J.-C. Gayde, M. Sulc, and K. Polak, "Introduction to structured laser beam for alignment and status of the R&D," (2022).
32. R. M. Herman and T. A. Wiggins, "Production and uses of diffractionless beams," J. Opt. Soc. Am. A **8**(6), 932–942 (1991).
33. Z. von F, "Beugungstheorie des schneidenver-fahrens und seiner verbesserten form, der phasenkontrastmethode," Physica **1**(7-12), 689–704 (1934).
34. R. J. Noll, "Zernike polynomials and atmospheric turbulence," J. Opt. Soc. Am. **66**(3), 207–211 (1976).
35. M. Dusek, "Advanced calibration and characterization of a Shack-Hartmann sensor," Master's thesis, Technical University of Liberec (2021).

5.183.15.154 {ts '2025-01-30 14:11:12'}

7.2 Detection of Structured Laser Beam Centroid and Its Use For Alignment

This conference paper presents the development of detection techniques for the SLB centroid coordinates. It evaluates and compares several centroid detection algorithms, including best-fitting of parameterized Bessel functions and center of gravity methods with gamma correction and thresholding corrections. Both simulated and experimental data are analyzed, with experiments involving controlled CMOS sensor translations using a high-precision motorized stage to assess precision. Additionally, the paper underlines the problems caused by the refractive index gradient and fluctuations. This contribution was presented at the International Workshop on Accelerator Alignment held in Ferney-Voltaire, France (IWAA2022) [62].

DETECTION OF STRUCTURED LASER BEAM CENTROID AND ITS USE FOR ALIGNMENT

Martin DUSEK, CERN, Geneva Switzerland, and TUL, Liberec, Czech Republic
Krystof POLAK, CERN, Geneva, Switzerland and TUL, Liberec, Czech Republic
Jean-Christophe GAYDE, CERN, Geneva, Switzerland
Miroslav SULC, TUL, Liberec, Czech Republic
Dirk MERGELKUH, CERN, Geneva, Switzerland
Witold NIEWIEM, CERN, Geneva, Switzerland and ETH, Zurich, Switzerland

Abstract

A Structured Laser Beam (SLB) [1] is a pseudo-non-diffractive optical beam. Its transverse profile is similar to a Bessel Beam (BB), hence its bright central core is surrounded by concentric circles. SLB can propagate with very low divergence over long distances. Propagation over 200 m has been tested with a divergence under 0.01 mrad. Therefore, the central core can still fit on the camera chip and its centroid position can be accurately detected, which is not the case for well-known Gaussian beams (GB). These properties make the SLB a promising candidate for long-distance alignment applications because it could be used as a reference line.

The alignment accuracy is affected by the algorithms for centroid detection. In this work, different algorithms for centroid position detection are evaluated and compared on simulated data, namely the best fitting of a well-parameterized Bessel function and different alternations of the center of gravity methods. In addition to simulations, real data are obtained during experiments using a high-precision motorized stage to induce a known translation of a sensor resulting in misalignment. This misalignment is compared with the misalignment detected by an SLB sensor. Therefore, the potential of SLB for long-distance alignment is explored.

CERN-BE-2023-012
31/10/2022

INTRODUCTION

The alignment of accelerator components with high accuracy is a challenging task. At CERN straight-line reference systems have been developed to meet the tight accuracy needs. The principle of the systems is based on stretched wires (Wire Positioning System) and water level (Hydrostatic Leveling System) [2]. These systems are precise in the order of micrometers over hundreds of meters, however, have drawbacks such as cost or implementation difficulties. It is also difficult to find a system that could give similar results for the comparison. Hence using a laser as a reference line can be a viable alternative.

The laser light path is assumed to be a straight line. Note that this has to be investigated due to refraction and symmetry breaking [3]. Systems with laser beams propagating in a vacuum, to minimize the effect of refraction caused by air fluctuations, have been developed for several accelerators. Japanese High Energy Accelerator Research Organization (KEK) uses mechanically switched quadrant-photodetectors to detect the laser propagating inside a vacuum tube [4]. Estimated accuracy is 100 μm over 500 m. The quadrant-photodetectors however have a drawback, if there is an irregularity in the laser spot shape, the centroid detection accuracy can be strongly affected.

The Compact Linear Collider (CLIC) [5] is a proposed accelerator that is under study at CERN. The project has quite tight alignment tolerances of 10 μm over 200 m. The LAMBDA sensor was in development for this task [6]. The principle lies in projecting a GB propagating through a vacuum on a plate. The plate is movable, therefore it can block the path of the laser when moved in. The projection of the GB is then viewed with the camera and the center is calculated and measured using Gaussian function fitting and photogrammetry. However, this system has several disadvantages. After propagation of 200 m, most of the intensity is lost and the ability for precise detection of the center is affected due to the divergence and beam energy loss. The other source of error is the photogrammetric camera objective, which induces field deformation due to lens aberrations, and also brings additional calculation steps.

The Structured Laser Beam has the potential for long-distance alignment due to its extremely low divergence and sharply defined core, which can fit on a reasonably sized chip even after propagating for 120 m (figure 5). This allows us to read the image straight from the camera chip, without using any optics, and use highly precise algorithms for center detection. This can potentially eliminate the drawbacks of the LAMBDA sensor and quadrant-photodetector systems.

To meet the tight alignment tolerances, algorithms for centroid detection with sub-pixel accuracy need to be implemented. The centroid detection will be discussed in the following chapters together with the investigation of the refractive index fluctuation effect of the medium of propagation. The resulting data should highlight the potential of SLB for long-distance alignment applications.

DETECTION OF A BEAM CENTROID

Center of Gravity

The Center of gravity (CoG) algorithm, the so-called first moment weighted by intensity, is widely used in different image processing applications [7]. It is not computationally expensive and reaches sub-pixel accuracy. The centroid coordinates $\bar{x}$ and $\bar{y}$ are calculated as:

$$\bar{x} = \frac{\sum_{x=0}^{x_{max}} \sum_{y=0}^{y_{max}} I(x,y)x}{\sum_{x=0}^{x_{max}} \sum_{y=0}^{y_{max}} I(x,y)} \quad (1)$$

$$\bar{y} = \frac{\sum_{x=0}^{x_{max}} \sum_{y=0}^{y_{max}} I(x,y)y}{\sum_{x=0}^{x_{max}} \sum_{y=0}^{y_{max}} I(x,y)} \quad (2)$$

where $I(x,y)$ is the measured intensity at a given pixel row x and column y of an image.

The preprocessing of an image can reduce noise in the image and increase the accuracy of CoG algorithms. In our case thresholding and gamma correction were used and will be referred to as the TCoG and GCoG respectively.

The TCoG algorithm uses the thresholding function *T(x,y)* which sets the pixel value to zero when its intensity is lower than the threshold level *t* after background subtraction:

$$T(x,y) = \begin{cases} I(x,y), I(x,y) \geq t \\ 0, I(x,y) < t \end{cases} \quad (3)$$

In the case of GCoG, we introduce a non-linear relationship between pixel intensity levels using function G_{corr}. Hence low-intensity values are lowered and high-intensity values are enhanced:

$$G_{corr}(x,y) = I_{max} \left(\frac{I(x,y)}{I_{max}} \right)^{\gamma} \quad (4)$$

As the value of gamma parameter γ increases, the upward-sloping of the function is larger, hence the bigger the relative difference between the intensity levels.

Best fitting of a well-parameterized Bessel function

Best-fit algorithm (BFA) finds the optimal parameters of the equation describing the BB intensity distribution, to match the shape of the observed beam. The intensity distribution of a BB with the center intensity normalized to one is described as:

$$I(x,y,\bar{x},\bar{y},k_T) = \left(J_0 \left(k_T \sqrt{(x-\bar{x})^2 + (y-\bar{y})^2} \right) \right)^2 \quad (5)$$

where J_0 is a Bessel function of the first kind and zero order, k_T is the transverse wave vector. The parameters k_T, $\bar{x}$ and $\bar{y}$ are the subject of change during the optimization process which roughly estimates the values. After the optimization, the precise positions of $\bar{x}$ and $\bar{y}$ are found using non-linear least-squares fitting:

$$\underset{\bar{x},\bar{y}}{minimize}\ I(x,y,\bar{x},\bar{y},k_T) = \sum_{i=0}^{m} I(x,y,\bar{x},\bar{y},k_T)^2 \quad (6)$$

It is possible to use BFA for the centroid detection of SLB, due to the similarity of the intensity distributions between BB and SLB. Note, that this fact can also be a cause of the error.

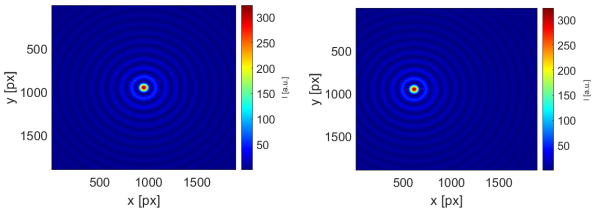


Figure 1: Image of the region of interest (ROI) with the BB centered in the middle of it. Latter image with the BB centroid shifted on X-axis by 320 pixels.

Bessel Beam centroid detection

To investigate the error in centroid detection caused by the fact that the equation 5 does not precisely describe the intensity distribution of an SLB, we used BFA to detect the centroid of a BB first. To be sure that the center of the BB centroid is in a known spot, simulated beam intensity distributions were generated using the software VirtualLab Fusion©. We simulated a system with an NBK-7 glass axicon with an angle of 1°. The size of the output images was 1901x1901 pixels (px).

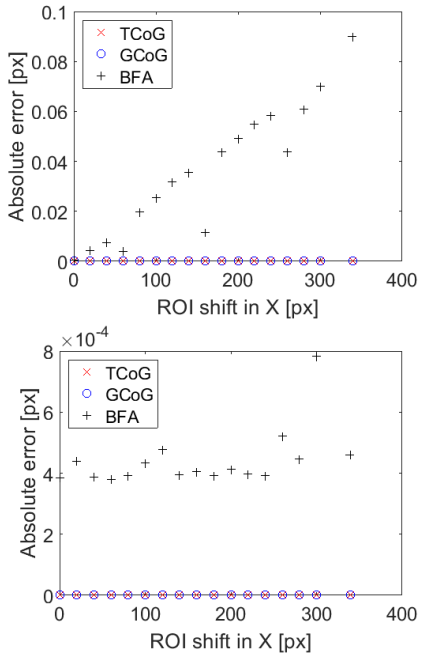


Figure 2: Absolute error of BB centroid coordinates dependency on ROI shift in X-direction for $\bar{x}$ (top) and $\bar{y}$ (bottom).

It was assumed that BFA will be more precise than the algorithms using the CoG principle. To investigate the performance, the rectangular ROI sized 950x950 pixels was extruded out of the original image. The centroids of the ROI and BB were in the corresponding known positions. Later, we introduced a shift of the ROI in the X-axis to have the beam centroid in a different position relative to

the ROI centroid as illustrated in the right part of figure 1.

All of the centroid algorithms with fixed parameters k_T, t, and γ were used to find the centroid in images with linearly increasing shift in the X-coordinate of the ROI. Then we compared the known position of the BB centroid with the one detected. By an absolute error, we mean residual between the known centroid of the beam and the detected one.

The results in figure 2 show that when we introduce a shift in X-axis, the absolute error of the $\bar{x}$ for the BFA is linearly increasing with the shift. While the Y-axis shift remains zero, hence the beam is centered in that axis, the error of $\bar{y}$ does not show the linear trend. CoG algorithms are not affected by the shift in the X-axis, the error remains in the order of 10^{-6} of a pixel and does not show any trend. The process was tested by introducing a shift in Y-axis while X-axis staying the same with a similar result. Hence only the error of $\bar{y}$ was linearly increased with the shift in Y-axis, while the error of $\bar{x}$ remained unaffected.

Structured Laser Beam centroid detection

The algorithms were tested on simulated SLB data as well. The shifting of the ROI in the X-direction was repeated. We can see the same linear trend of the absolute error for BFA which goes up to 0.18 pixels. We believed that this is caused by the fact that some parts of the beam's outer rings are cut out of the image (figure 1). Therefore, the circular mask was used to make sure that only full rings remain in the image (figure 3).

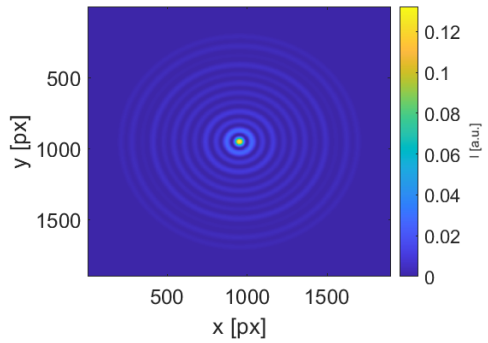


Figure 3: SLB intersected using a circular mask, hence only full beam rings are present in the image.

The results in figure 4 show that masking out the non-full rings significantly lowers the error of BFA and it is no longer linearly dependent on the ROI shift in the X-direction. The error of the GCoG is in the order of 10^{-3} pixels, while the error of the TCoG is in the order of 10^{-5} pixels. After using a mask, the error of BFA is in the order of 10^{-2} pixels.

The CoG algorithms are slightly more accurate and less computationally expensive than BFA. Hence they are suitable for applications where the detection of centroid in multiple images per second is needed (table 1). The TCoG algorithm behaves better for simulated data. However, in

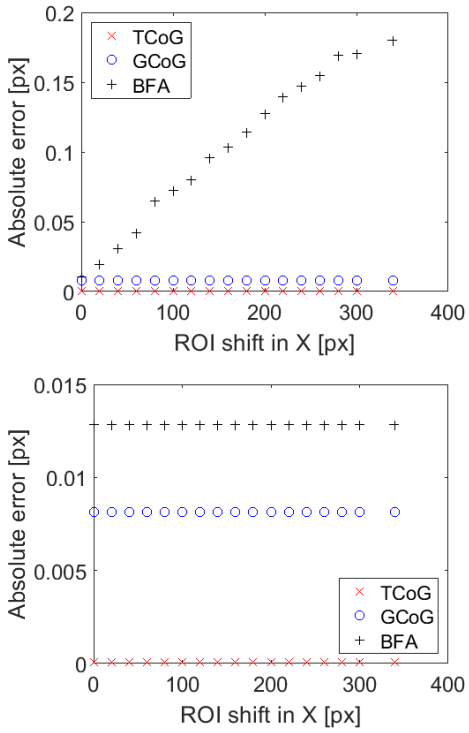


Figure 4: Absolute error of SLB $\bar{x}$ centroid coordinate dependency on ROI shift in X-direction for unmasked (top) and masked (bottom) images respectively.

real conditions, background subtraction has to be done, hence it can be prone to background illumination changes. The algorithm is also sensitive to the changes of threshold level t.

Table 1: Relative computational time for analysis of 1901x1901 pixel image. Implemented in MATLAB.

Algorithm	**Computational time**
BFA	40.03 s
GCoG	0.17 s
TCoG	0.16 s

The camera chips have a rectangular shape hence the error of the BFA can be significant and depends on the relative position of the beam centroid to the image center. In our simulations, the error was reaching up to 0.18 pixels. The preliminary tests on simulated images with introduced noise show that the absolute error of the BFA caused by the relative beam position can be even higher. This can have a significant effect on high-precision alignment applications. To get rid of this source of error, it is necessary to use a circular mask that cuts out non-full outer beam rings. This is not the case for the CoG algorithms, because the threshold and gamma correction minimizes the influence of the rings on the centroid detection.

LONG DISTANCE ALIGNMENT INVESTIGATION

In this chapter, the potential of the SLB for use in high-precision alignment was investigated also experimentally. Refractive index fluctuations of the propagation media play a major role in laser light alignment systems. The SLB is a novel type of laser beam hence the influence of the phenomenon has not been yet described thoroughly. The SLB propagation and stability were measured over 120 m in one of the CERN underground tunnels (figure 5).

We used the GCoG to detect the centroid with 3 frames per second for 1 hour. Even though the TCoG behaves better on simulated data, in real conditions it is prone to the choice of the optimal threshold level t and background illumination. These effects need to be investigated more to be able to use the TCoG algorithm proficiently. The absolute of the GCoG is not as significant even if the γ is not chosen optimally and the background illumination does not play such a big effect, due to the working principle of the algorithm.

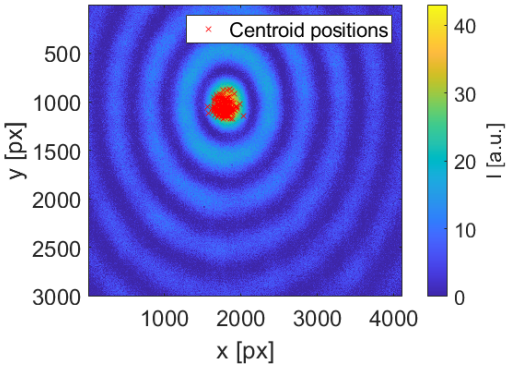


Figure 5: Real image of SLB propagated over 120 m in CERN underground tunnel. Projected on a camera with a chip size of 14.1x10.3 mm and pixel size of 3.45 μm.

The maximal amplitude of the oscillations is $\pm$0.82 mm and $\pm$0.53 mm with standard deviation σ of 0.234 mm and 0.229 mm for x and y respectively. This will play a major role if we want to achieve alignment in the order of μm. On the other hand, the measured data do not have a large spread and they are oscillating around one point. Hence, it can be advantageous to extract information about the position by taking the mean of all centroid positions.

We decided to rebuild the experiment for a shorter distance in the laboratory to investigate, how well it is possible to extract the information about the position of a sensor relative to a reference position given by the beam.

Setup

The beam was propagated over 1.8 m on an optical table. SLB was projected straight on a camera chip without any objective lens. The SLB is stationary forming a reference, while the camera is moved by precise amounts using the highly precise motorized stage hence representing an object of alignment. We used Thorlabs one-axis motorized stage MT1/M-Z8 with a resolution of 50 nm,

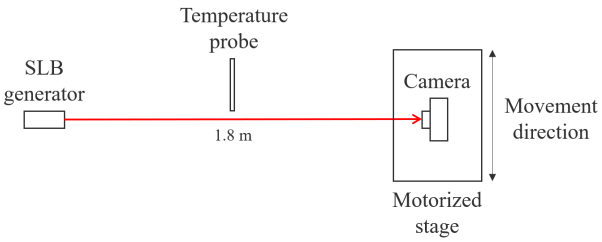


Figure 6: Schematic view of the setup.

The angles between the camera, motor, and laser were measured with a laser tracker. It was calculated that the perpendicularity misalignment between the camera chip, motor movement direction, and laser line is under $\pm 1°$.

Results and discussion

The long-term stability of the line was measured for 11 hours (figure 7). We can see noticeable oscillations of the beam centroid with an amplitude of $\pm$5 μm.

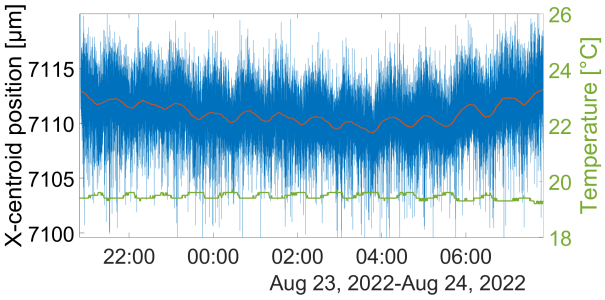


Figure 7: Stability of the beam was measured for 11 hours including the temperature measurement. The red line represents the moving average of the data for better visibility of the trend.

The temperature in the laboratory is relatively stable due to the air-conditioning (AC). It was measured with a resolution of 0.1 °C. The temperature probe was placed approximately in the middle between the camera and the generator. The correlation between temperature and the position of the reference line is noticeable. As the temperature periodically changes, which is caused by the AC switching on and off, the same periodical change can be seen on the moving average of the centroid coordinate. The low-frequency change that is noticeable over the whole span of the data can be caused by the thermal expansion of the camera/generator holders, local temperature changes, or by a different, yet unknown factor.

The relative movement from the original position was also investigated. The motorized stage with the camera was moved for 15 μm. When it was in place the data acquisition

started for 20 seconds. We decided to use the GCoG algorithm to obtain the centroid position by analyzing 3 frames per second. The average standard deviation of the data in each position was 1.2 μm. All values greater than 2σ were marked as noise and the rest of the data was averaged to obtain an average value of the position. This process was repeated several times.

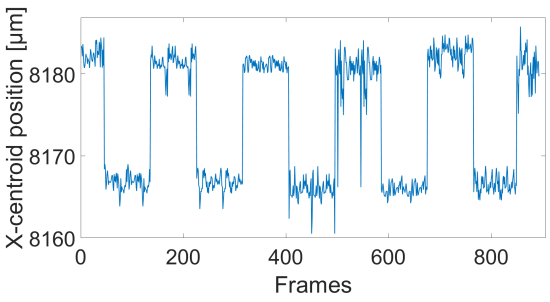


Figure 8: X-centroid coordinates obtained by GCoG while moving the camera for 15 μm.

We were able to reconstruct the relative movement of 15 μm multiple times with an error of ± 1.3 μm. The 1° misalignment of the setup means that the movement will not be completely perpendicular to the line, hence the systematic error is introduced. However, by simple trigonometric calculation, we can conclude, that this systematic error will be in the order of nm.

Results show that the refractive index oscillations of the propagation media caused by temperature instabilities, air fluctuations, and other variables represent a problem in future long-distance alignment applications as expected. We propose propagating the laser inside a tube, ideally under a vacuum, to obtain even better results.

CONCLUSION

Multiple algorithms for centroid coordinate detection of pseudo-non-diffractive beams, namely the BB and the SLB, were principally explained and compared. Results show that a preprocessing of the images is needed to obtain precise results. For the BFA, a circular mask to filter out the non-full ring of the beam needs to be used. The TCoG algorithm is very prone to the value of threshold level and background illumination changes. The GCoG has the best trade-off between speed, precision, and gamma parameter sensitivity for real measurements.

The potential of SLB for long-distance alignment applications was investigated. The bright central core can fit on the camera chip after propagating over 120 m hence it is possible to easily detect its centroid coordinates. However, it was confirmed that the atmospheric turbulence and surrounding conditions play a major role in the beam stability and detection of the magnitude of the misalignment. Refraction can also have a significant influence on the reference line's straightness.

The experiment was rebuilt for a shorter distance in the laboratory. The beam was propagated in the free space and misalignment of 15 μm with an error of ± 1.3 μm over 2 m was detected multiple times. We propose propagating a beam inside a tube and vacuum in future experiments to minimize the effect of refractive index fluctuations.

ACKNOWLEDGEMENT

The authors acknowledge the financial support provided by the Knowledge Transfer group at CERN through the KT Fund.

This work has also been partly carried out within the framework of the project "Partnership for Excellence in Superprecise Optics" (Reg. No. CZ.02.1.01/0.0/0.0/16_026/008390) and co-funded by European Structural and Investment Funds.

REFERENCES

[1] J.-C. Gayde and M. Sulc, "An Optical System for Producing a Structured Beam," EP3564734, 2019.

[2] H. Mainaud Durand et. al., "HL-HLC Alignment Requirements and Associated Solutions," CERN, 2017, Copenhagen, Denmark, Proceedings of IPAC2017.

[3] K. Polak, J.-C. Gayde, and M. Sulc, 'Structured laser beam for alignment and large-scale metrology', Euspen Conf., vol. EUSPEN2022, p. 4, 2022.

[4] T. Suwada, M. Satoh, S. Telada, and K. Minoshima, 'Propagation and stability characteristics of a 500-m-long laser-based fiducial line for high-precision alignment of long-distance linear accelerators', Review of Scientific Instruments, vol. 84, no. 9, p. 093302, Sep. 2013, doi: 10.1063/1.4819960.

[5] CERN. `https://home.cern/science/accelerators/compact-linear-collider`. Accessed 26. August 2021.

[6] G. Stern, 'Study and development of a laser based alignment system for the compact linear collider', Doctoral Thesis, ETH Zurich, 2016. doi: 10.3929/ethz-a-010621412.

[7] A. M. Nightingale and S. V. Gordeyev, 'Shack-Hartmann wavefront sensor image analysis: a comparison of centroiding methods and image-processing techniques', OE, vol. 52, no. 7, p. 071413, Mar. 2013, doi: 10.1117/1.OE.52.7.071413.

7.3 Analysis of Centroiding Algorithms for Non-Diffracting Structured and Hollow Structured Laser Beams

This paper explores different centroiding algorithms for detecting the alignment reference given by SLBs and Hollow SLBs. The research is conducted on simulated data. Various techniques, including center of gravity methods with gamma correction and thresholding corrections, as well as correlation template matching, are evaluated for their robustness and accuracy. The study also introduces a novel polarization-based centroiding algorithm, leveraging the polarization distribution of Hollow SLB. It also provides a deep comparative analysis of these methods under different noise conditions, and analyzes the computational effectiveness and accuracy. The erratum is included, which provides additional explanation and correction for the correlation template matching algorithms. This paper and the erratum were published in Applied Optics (Q3, Impact Factor = 1.7).

Research Article Vol. 63, No. 1 / 1 January 2024 / Applied Optics 263

applied optics

Analysis of centroiding algorithms for non-diffracting structured and hollow structured laser beams

Martin Dusek,[1,2,*] Eva Roikova,[1,2] Dirk Mergelkuhl,[1] Jean-Christophe Gayde,[1] Krystof Polak,[1,2] and Miroslav Sulc[2,3]

[1]The European Organization for Nuclear Research (CERN), Geneva, Switzerland
[2]Technical University of Liberec (TUL), Liberec, Czech Republic
[3]Institute of Plasma Physics of the Czech Academy of Sciences (IPP CAS), Prague, Czech Republic
*martin.dusek@cern.ch

Received 23 October 2023; revised 24 November 2023; accepted 24 November 2023; posted 28 November 2023; published 21 December 2023

This paper explores the potential of optical-based systems, specifically pseudo-non-diffractive beams, as an alternative for alignment. The study focuses on structured laser beams and hollow structured laser beams, which exhibit lower divergence and enhanced detection capabilities. The research objective is to analyze and compare centroiding algorithms in terms of accuracy and robustness to noise. The study compares the gamma-corrected and threshold-corrected center of gravity and correlation template matching. It also introduces a polarization-based algorithm.

Published by Optica Publishing Group under the terms of the Creative Commons Attribution 4.0 License. Further distribution of this work must maintain attribution to the author(s) and the published article's title, journal citation, and DOI.
https://doi.org/10.1364/AO.509927

1. INTRODUCTION

A multi-point alignment of particle accelerator components is a challenging task due to the need for accuracy of tens of micrometers over hundreds of meters. The fundamental approach of these systems involves measuring the offset relative to a reference line. At CERN, the European Organization for Nuclear Research, line reference systems such as a wire positioning system combined with a hydrostatic leveling system were developed to meet tight accuracy needs [1]. While these systems exhibit high precision, they also have limitations, such as implementation complexities and component costs. Using an optical-based system as a reference line serves as a potential alternative. Several optical-based systems for aligning structures over long distances have been presented in various works [2–6]. One drawback of these systems is the relatively high divergence of optical systems caused by diffraction, which makes the straight-line reference measurement more challenging over long distances.

A laser light path is typically assumed to be a straight line. Systems with laser beams propagating in a vacuum, to minimize the effect of refraction caused by air fluctuations, have been developed for several accelerators. The Japanese High Energy Accelerator Research Organization (KEK) employs mechanical shutters with quadrant-photodetectors to detect the laser propagating inside a vacuum tube [2]. The estimated accuracy is 100 μm over 500 m. However, the quadrant-photodetectors have a drawback: if there is an irregularity in the laser spot shape, the centroid detection accuracy can be strongly affected [7].

The Compact Linear Collider (CLIC) [8] is a proposed accelerator that is currently under study at CERN. The project has very tight alignment tolerances of 10 μm (1σ) over 200 m. A LAMBDA sensor was developed for this task by Stern [9]. The sensor's principle involves projecting a Gaussian beam (GB) propagating through a vacuum on a plate. The plate is placed on a mechanical shutter that can obstruct the path of the laser. The projection of the GB is then viewed with a camera. The center is calculated and measured using Gaussian function fitting and photogrammetry techniques. This system suffers from several drawbacks. After propagating over several tens of meters, most of the beam intensity is lost, and the ability to precisely detect the center is compromised due to the divergence. Another source of error arises from the photogrammetry technique used, which induces field deformation of the captured image due to lens aberrations. The correction of the field deformation requires additional calculation steps.

A structured laser beam (SLB) and hollow structured laser beam (HSLB) are pseudo-non-diffractive beams with a transversal intensity profile similar to a Bessel beam (BB) of a zeroth and first or higher orders, respectively [10–13]. They share the properties of the BB, such as lower divergence of the central core compared to a GB and the possibility to regenerate behind an obstacle. The generation of such beams relies on optical

aberrations of the optical elements used. More about the generation principle and parameter assessment can be found in our previous works [14–17] and in the paper by Herman [18]. Propagation over 900 m was recently tested with the divergence of the central core under 0.01 mrad. Even after propagating for several hundred meters, the central core of the beam can fit within a reasonably sized CMOS or CCD chip, enabling direct image capture from the chip without the need for additional optics. Hence, there is a potential to minimize the drawbacks of the LAMBDA sensor and other optical systems. This makes a pseudo-non-diffractive beam-based straight-line reference system a promising candidate for the alignment of future colliders at CERN. These include the currently studied CLIC or Future Circular Collider (FCC) [19].

There are several reports on using pseudo-non-diffractive beams for alignment. The BB has been used for the alignment of lenses by Parks [7] where the center of gravity is used with a threshold to detect the centroid of the beam and comments on the disadvantage of using quadrant-photodetector for the BB centroid detection. Gale detects the center by observing a crossed wire with a projection of the BB to align large structures over 19 m [20]. None of these works provides a quantitative, in-depth analysis of algorithms that can be used to detect the BB, SLB, or HSLB centroid. Bridging this knowledge gap is critical for quantifying the error introduced by the algorithm in the alignment system.

Center of gravity and correlation template matching algorithms are well known, and their accuracy has already been studied for different applications such as Shack–Hartmann sensing and image processing [21–23]. Nevertheless, these algorithms have never been studied when applied to centroid detection of pseudo-non-diffractive beams. This work aims to provide an in-depth analysis of the accuracy of such algorithms on simulated data. Additionally, a novel method for the detection of the HSLB centroid using knowledge of the polarization distribution is presented. This is made possible by the generation principle of the HSLB that includes the non-classically polarized field of the input beam through radial, azimuthal, or spiral polarization. The resulting data give a perspective on the potential of pseudo-non-diffractive beams, particularly the SLB and HSLB, for alignment applications. Furthermore, the study highlights the pros and cons of the algorithms for centroid detection in specific conditions.

2. METHODOLOGY

A. Weighted Center of Gravity Algorithm

The weighted center of gravity (WCoG) algorithm, the so-called first moment weighted by intensity, is not computationally expensive and reaches sub-pixel accuracy. The centroid coordinates $\bar{x}$ and $\bar{y}$ are calculated as

$$\bar{x} = \frac{\sum_{x=0}^{x_{\max}} \sum_{y=0}^{y_{\max}} I(x,y)x}{\sum_{x=0}^{x_{\max}} \sum_{y=0}^{y_{\max}} I(x,y)}, \tag{1}$$

$$\bar{y} = \frac{\sum_{x=0}^{x_{\max}} \sum_{y=0}^{y_{\max}} I(x,y)y}{\sum_{x=0}^{x_{\max}} \sum_{y=0}^{y_{\max}} I(x,y)}, \tag{2}$$

where $I(x, y)$ is the intensity distribution at a given pixel row x and column y of an image.

The preprocessing of an image can reduce noise in the image and increase the accuracy of WCoG algorithms. This paper used thresholding and gamma correction, referred to as the TCoG and GCoG, respectively.

The TCoG algorithm uses the thresholding function $T(x, y)$, which sets the pixel value to zero when its intensity is lower than the threshold level t after background subtraction:

$$T(x,y) = \begin{cases} I(x,y), & I(x,y) \geq t \\ 0, & I(x,y) < t \end{cases}. \tag{3}$$

In the case of GCoG, a non-linear relationship between pixel intensity levels using function G_{corr} was introduced. Hence, low-intensity values are lowered, and high-intensity values are enhanced:

$$G_{\text{corr}}(x,y) = I_{\max}\left(\frac{I(x,y)}{I_{\max}}\right)^{\gamma}. \tag{4}$$

As the value of the gamma parameter γ increases, the curvature and the gradient of the curve become more significant, hence the more prominent the relative difference between the low- and high-intensity levels. In other words, higher γ values make the bright parts even brighter and the dark parts even darker, emphasizing the differences. Lower γ values have the opposite effect, making the image appear more uniform in intensity. Hence, in the gamma-corrected image, only the brightest pixels of the inner core will be visible [24].

B. Correlation Template Matching Algorithm

The correlation template matching algorithm (CORR) calculates a normalized 2D correlation function $C(u, v)$ between a squared 2D Gaussian function template $t(x, y)$ and the intensity distribution [25]:

$$C(u\bar{x},\bar{y}) = \frac{\sum_{x,y}\left|I(x,y) - \overline{I_{u,v}}\right|\left[t\,(x-\bar{x}, y-\bar{y}) - \bar{t}\right]}{\left\{\sum_{x,y}\left|I(x,y) - \overline{I_{u,v}}\right|^2 \sum_{x,y}\left[t\,(x-\bar{x}, y-\bar{y}) - \bar{t}\right]^2\right\}^{0.5}}. \tag{5}$$

Here $\bar{t}$ is the mean of the template intensity and $\overline{I_{u,v}}$ is the mean of the intensity distribution in the region under the feature. The input parameters of the algorithm are the size of the side of the squared template S_c and the standard deviation of the Gaussian function STD_c, which affects the shape of the function. A Gaussian interpolation is applied to obtain sub-pixel results. An in-depth explanation of the sub-pixel extraction and the formula can be found in the paper from Li *et al.* [23]. Note that for the HSLB, the Gaussian template has inverted intensity values to match the HSLB core.

C. Polarization Algorithm

If one assumes a radially polarized input beam to produce the HSLB, a polarimetric centroid detection algorithm (POL) developed in this paper can be used. Polarimetric measurement allows Stokes parameters to be obtained [26]. Knowing these parameters, a polarization ellipse orientation angle ψ can be

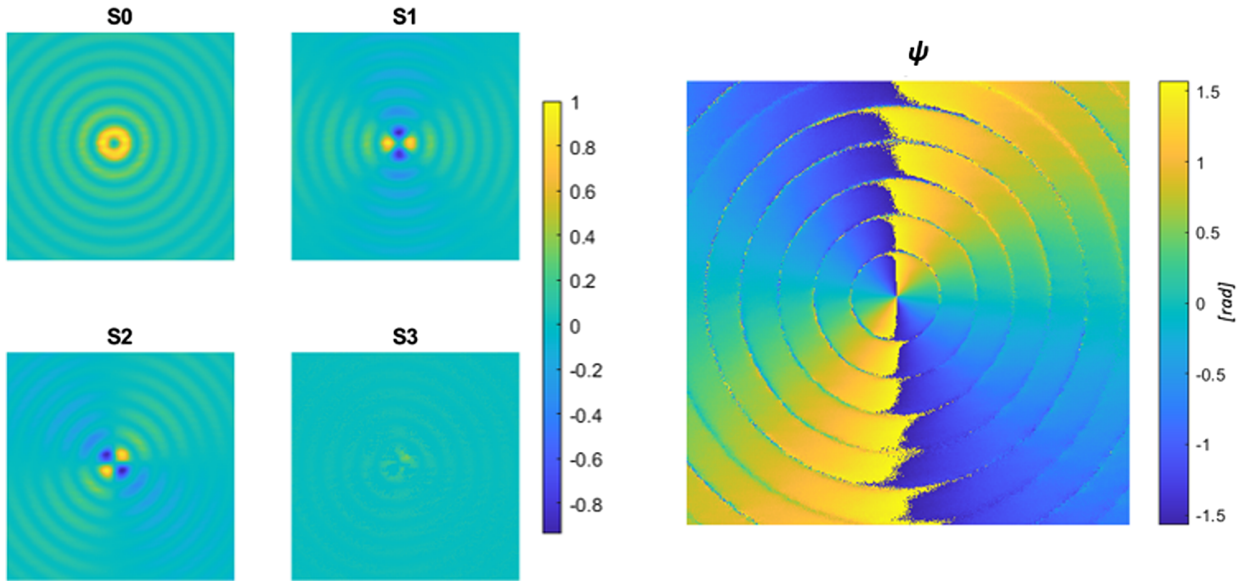


Fig. 1. S0, S1, S2, and S3 represent normalized Stokes parameters of HSLB with radial polarization distribution. ψ represents orientation angle of polarization ellipses.

determined; see Fig. 1. For each interval (ψ_i, ψ_{i+1}) spaced by $\frac{\pi}{180}$ rad, pixel coordinates (x_p, y_p) were found with the corresponding value of the polarization ellipse orientation angle:

$$P_i(x_p, y_p) \in (\psi_i, \psi_{i+1}), \quad \text{where} \quad \psi \in \left(-\frac{\pi}{2}, \frac{\pi}{2}\right) \quad \text{and} \quad i = 1, 2, \ldots, 180. \tag{6}$$

Every set of P_i coordinates was fitted with the linear equation

$$y_i = p_1 x_i + p_2. \tag{7}$$

To preserve the stability of evaluation, the coefficient of determination R^2 was required to be higher than 0.996. Only fitted lines in the following interval are considered to fulfill those conditions:

$$\psi \in \left(-\frac{4\pi}{9}, -\frac{\pi}{18}\right) \cup \left(\frac{\pi}{18}, \frac{4\pi}{9}\right). \tag{8}$$

The centroid coordinates $\bar{x}$ and $\bar{y}$ of the HSLB are found as the intersection of fitted lines fulfilling the condition in Eq. (8). The number of lines p_{lines} can be altered by changing the spacing of the interval.

D. Simulation Parameters

A comprehensive analysis of centroiding algorithms on simulated data is presented. The data used for the analysis were generated through numerical simulations utilizing custom-developed software. The simulation involved tracing rays through the generator, consisting of a 5 mm ball lens made of S-LAH79 Ohara glass with a refractive index of approximately two for a wavelength of 632.8 nm, which is the wavelength of the laser source used. A plano–convex projection lens, constructed with Schott N-BK7 glass, was utilized, having a diameter of 25.4 mm and a radius of curvature of 25.8 mm. The distance between the lenses was set to be $L_{\text{PL}} = 96.8$ mm. The input field of the SLB was linearly polarized, while for the HSLB, it was radially polarized. The scheme of a generator can be seen in Fig. 2.

For long-distance applications, where the beam can travel hundreds of meters, detecting the centroid position at multiple points, each at a different distance, is necessary. Hence, it is crucial to evaluate the performance of the algorithms for beams with various core sizes due to divergence. A numerical calculation of a Fresnel diffraction integral was performed for the traced field directly behind the generator and propagated to distances from 2 to 102 m with a step size of 2 m to generate intensity distributions in different distances. This resulted in 51 intensity distributions that were subjected to subsequent analysis. The virtual camera chip had dimensions of 10 × 10 mm, with 2001 × 2001 pixels (px). The intensity distributions with the corresponding diagonal line intensity profiles and core sizes at 102 m can be seen in Fig. 3. For the SLB, the core size was defined as the radius of the first dark circle surrounding the central core. For the HSLB, it is the radius of the most intense part of the first ring.

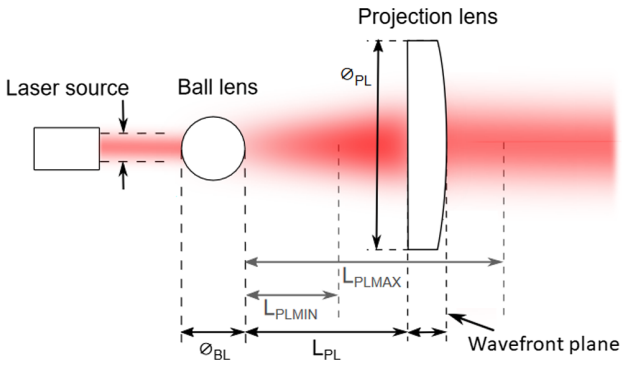


Fig. 2. Schematic of an SLB generator.

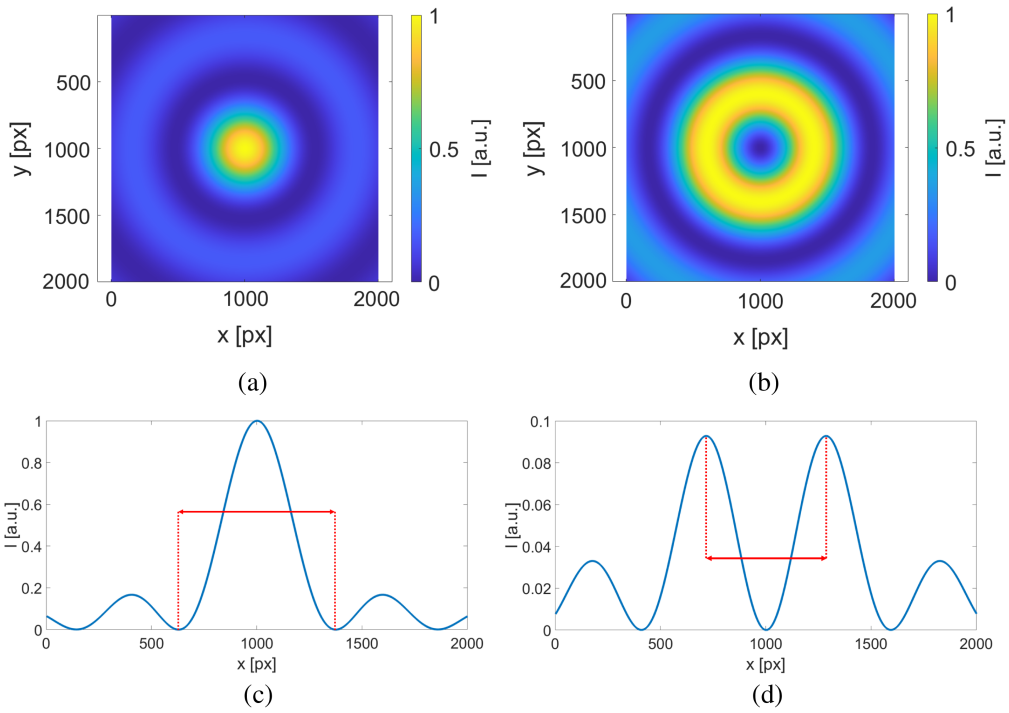


Fig. 3. (a) Simulated SLB intensity distribution at 102 m. (b) Simulated HSLB intensity distribution at 102 m. (c) SLB's diagonal line intensity profile with the core size definition indicated in red. (d) HSLB's diagonal intensity line profile with the core size definition indicated in red.

A rectangular region of interest (ROI) measuring 1501 × 1501 px was extracted from each simulated intensity distribution. The corresponding position of the centroid for both the ROI and the beam was then established. Subsequently, a sub-pixel shift of 0.31 px was introduced in both axes for the ROI centroid using bicubic interpolation to displace the beam and ROI centroid relatively. This means that the position of the beam centroid was never precisely in the middle of the pixel. Hence, the symmetry did not artificially improve the results. Applying these measures accounted for real measurement conditions. Consequently, the centroid coordinates for both axes were adjusted to 751.31 px. Shifting the beam to different positions within the ROI was tested without affecting the overall results.

The algorithms underwent various testing methodologies, including evaluations of accuracy, time span, robustness to intensity noise, and sensitivity to parameters such as t, γ, STD_c, S_c, p_{lines}. All parameter values were determined based on empirical observations derived from previous experiments.

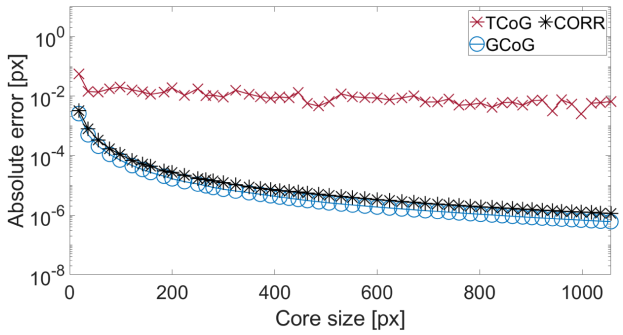
The accuracy assessment involved defining an absolute error (AE) as the absolute difference between the known position of the beam centroid and its corresponding position detected by the algorithm. A mean absolute error (MAE) with a standard deviation of the AE values (STD_e) was calculated by averaging the absolute error values across all core sizes in both axes to obtain a measure of overall accuracy. Analyzing the time span entailed modifying the region of interest (ROI) size and evaluating the accuracy and time required to analyze a single intensity distribution by each algorithm. This process is referred to as windowing. The noise was introduced by adding Gaussian white noise, which was employed to analyze the noise robustness of the algorithms, characterized by a mean value and a variance denoted as $\mathrm{var}_{\mathrm{noise}}$. During actual measurements, the signal-to-noise ratio (SNR) values are high, meaning that the beam is easily visible due to the possibility of controlling the laboratory condition in our particular case. The values of $\mathrm{var}_{\mathrm{noise}}$ were chosen based on the empirical observation and are therefore relatively low. Note that there will be no investigation of algorithm failure due to noise since this requires more than an order of magnitude higher $\mathrm{var}_{\mathrm{noise}}$ values. The sensitivity to parameters t, γ, STD_c, S_c, p_{lines} was compared by examining the mean and standard deviation of detected center positions (STD_p) with different parameter values.

3. RESULTS

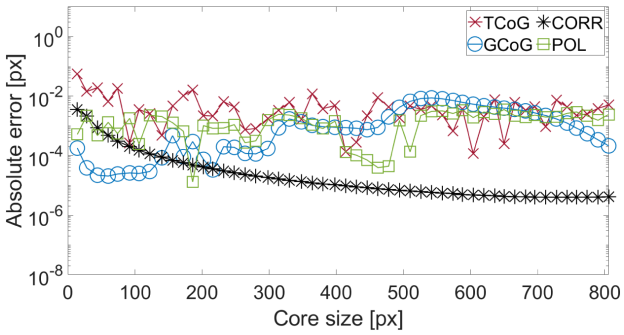
A. Effect of the Core Size

In Figs. 4(a) and 4(b), the absolute error (AE) of the SLB and HSLB centroid detection for different algorithms and various sizes of the central core is presented. The values of the parameters t, γ, STD_c along with the mean absolute error (MAE) for the SLB algorithm can be found in Fig. 4(c). Similar values for the HSLB, including p_{lines}, are provided in Fig. 4(d). It is crucial to note that S_c was set to be equal to the core size. The image data used for analysis were free of noise.

The AE generally goes down as the core size increases for all of the algorithms. The TCoG algorithm has a linearly decreasing trend with the MAE values for both beams in the order of hundredths of a pixel. The CORR is exponentially decreasing for both beams together with the GCoG for the SLB. The AE for CORR remains below 1e-2 px for a core size of 50 px and reaches the order of 1e-6 px for larger core sizes in both beams. The values repeat themselves for the GCoG in the case of the SLB.



(a)



(b)

	MAE [px]	Parameters
TCoG	1.01e-2	$t = 0.7 \cdot I_{max}$
GCoG	7.27e-5	$\gamma = 4$
CORR	1.02e-4	$STD_c = 100$

(c)

	MAE [px]	Parameters
TCoG	1.34e-2	$t = 0.4 \cdot I_{max}$
GCoG	1.24e-4	$\gamma = 4$
CORR	1.12e-4	$STD_c = 100$
POL	1.51e-3	$p_{lines} = 50$

(d)

Fig. 4. (a) AE of the algorithms detecting the centroid of the SLB in noiseless intensity distributions with the pixel size of a core. The change of the core size is caused by the increasing camera distance from 2 to 102 m. Zoom in on GCoG and CORR. (b) AE of the algorithms detecting the centroid of the HSLB in noiseless intensity distributions with the pixel size of a core caused by the camera distance varying from 2 to 102 m. Zoom in on GCoG, CORR, and POL. (C) MAE and t, γ, STD_c parameters used for SLB centroid detection. (D) MAE and t, γ, STD_c, p_{lines} parameters used for HSLB centroid detection.

For the HSLB, the GCoG, and the POL, the AE has a slightly linearly increasing trend with core size with the MAE equal to 1.24e-4 and 1.51e-3 px, respectively.

For short-distance alignment applications, it is crucial to ensure that, due to the small size of the core, the resolution is adequate for the required level of accuracy. It is worth noting that the GCoG algorithm seems to have the lowest AE values for beams with core sizes smaller than 150 px for both beams and has an overall best performance for the SLB. The best-performing algorithm for the HSLB seems to be the CORR.

B. Windowing and Time Span Analysis

The AE of the SLB and HSLB centroid detection for a single intensity distribution at a distance of 102 m is shown for different sizes of ROI. The ROI sizes ranged from 15 to 750 px, while the core size of the SLB was fixed at 1056 and 811 px for HSLB. The parameters t, γ, STD_c, p_{lines} used are similar to the ones in Figs. 4(c) and 4(d). If the ROI size was smaller than the core size, the parameter S_c was set to be two pixels smaller. The image analysis was conducted on noiseless data.

For the SLB, as presented in Fig. 5(a), the AE decreases as the ROI size increases for all algorithms before hitting a plateau. The TCoG algorithm exhibits an AE in the order of tenths of a pixel, which drops rapidly after the ROI size reaches 200 px after which AE remains in the order of hundredths of a pixel. The GCoG algorithm demonstrates that the AE is in the order of tenths of a pixel until the ROI size exceeds 220 px where it reaches the AE order of 1e-6 px after hitting the plateau. The AE of the CORR algorithm is only affected the most among the algorithms by the changing ROI size and hits the plateau after 320 px.

The time span analysis, shown in Fig. 5(b), indicates that the time spent calculating the centroid increases with the ROI size for all three algorithms. For ROI sizes smaller than 200 px, the time span of the CORR algorithm is below 0.05 s, below 5e-3 s for the GCoG algorithm, and below 5e-4 s for the TCoG algorithm. For the 750 px ROI, the AE of the CORR algorithm exceeds 1.64 s. For the GCoG, it reaches 0.13 s, while for TCoG, it goes up to 0.05 s.

Similar to the SLB analysis, the AE for HSLB decreases with increasing ROI size for all algorithms, as seen in Fig. 6(a). The AE of the TCoG algorithm reaches up to 0.95 px and slowly falls until it drops rapidly after the ROI size reaches 641 px. Afterward, the AE gets to 4.97e-3 px. The AE of the GCoG algorithm follows a similar trend, starting at 1.85 px, falling to 2.17e-4 px after the ROI size is equal to 691 px. The AE of the CORR algorithm starts at 0.29 px, reaching a plateau after the ROI size is equal to 400 px. The POL algorithm is almost unaffected by the ROI size and has the MAE value of 2.11e-3.

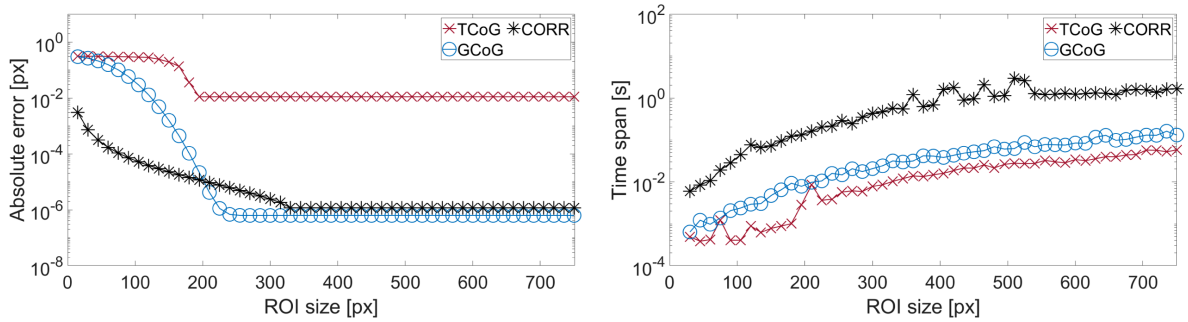


Fig. 5. (a) AE of the algorithms detecting the centroid of the SLB in noiseless intensity distributions with ROI size varying from 15 to 750 px. (b) Time span of algorithms for different sizes of the ROI.

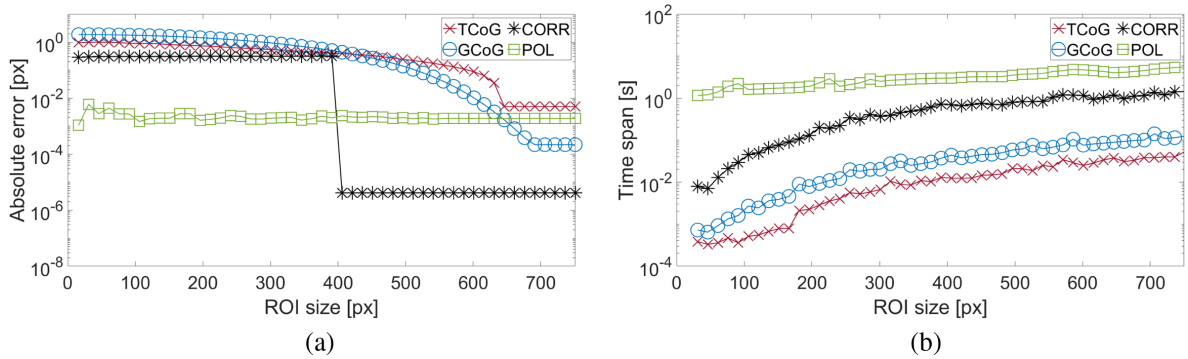


Fig. 6. (a) AE of the algorithms detecting the centroid of the HSLB in noiseless intensity distributions with ROI size varying from 15 to 750 px. (b) Time span of algorithms for different sizes of the ROI.

The time span analysis, shown in Fig. 6(b), exhibits similar trends and values for TCoG, GCoG, and CORR as observed in the SLB analysis. The POL algorithm is slower compared to the other algorithms. The time span starts at 1.10 s for an ROI size of 15 px and increases to 5.90 s.

The algorithms are susceptible to small ROI sizes, which may result in a higher AE due to the exclusion of a significant portion of the central core from the analysis. The ROI size can be reduced without sacrificing the accuracy of each algorithm by analyzing the point when the curve reaches the plateau phase. Otherwise, there will be a trade-off between the time and accuracy.

It is important to note that lowering the value of the p_{lines} parameter can also decrease the time span for the POL algorithm, but this change may increase the AE. Further analysis of this aspect will be conducted in the subsequent section. The results also suggest that the beam center can be larger than the chip size. However, the image's contrast is significantly reduced, and the centroid position analysis can be challenging during an actual measurement.

C. Sensitivity to the Change of Algorithm Parameters

To determine the optimal algorithm parameter and evaluate its sensitivity to variations, a comparison between the mean detected centroid along the x-axis and the mean reference value, accompanied by the standard deviation STD_c was conducted. A Gaussian white noise mask with a mean of zero and a variance of 1e-4 was introduced, which was then applied to intensity distributions of beams with varying core sizes. This method ensures uniformity in the noise distribution across all images, emphasizing the algorithm parameter's sensitivity in the outcomes rather than susceptibility to the inherent randomness of the noise. The known reference position of the centroid along the x-axis was established at 751.31 px.

Figures 7 and 9 depict the AE values corresponding to various core sizes. Additionally, Figs. 8 and 10 furnish the mean and standard deviation (STD_c) values for the detected x-coordinates of SLB and HSLB, respectively. In the case of the TCoG algorithm, the parameter t was calculated as $t = c_t \cdot I_{\max}$, with values of c_t being 0.65, 0.7, and 0.75 for SLB, and 0.4, 0.5, and 0.6 for HSLB. As for the GCoG algorithm, the parameter γ was consistently set to 3, 4, and 5 for both types of beams. The template size dS_c was varied by $\gamma \pm 4$ px, and STD_c was established at 50, 100, and 150 for both SLB and HSLB.

For the SLB, the mean closest to the reference value for the TCoG was achieved with $c_t = 0.7$, resulting in a difference of the mean equal to 1.04e-3 px relative to the reference value, together with the smallest STD_p relative to the other values, equal to 2.03e-2 px. The mean closest to the reference value for the GCoG, with a difference of 1.01e-3 px and with the smallest STD_p of 5.94e-4 px, were both observed for $\gamma = 4$. For the CORR algorithm, the most precise results were obtained with the precisely measured core size together with $\text{STD}_c = 100$,

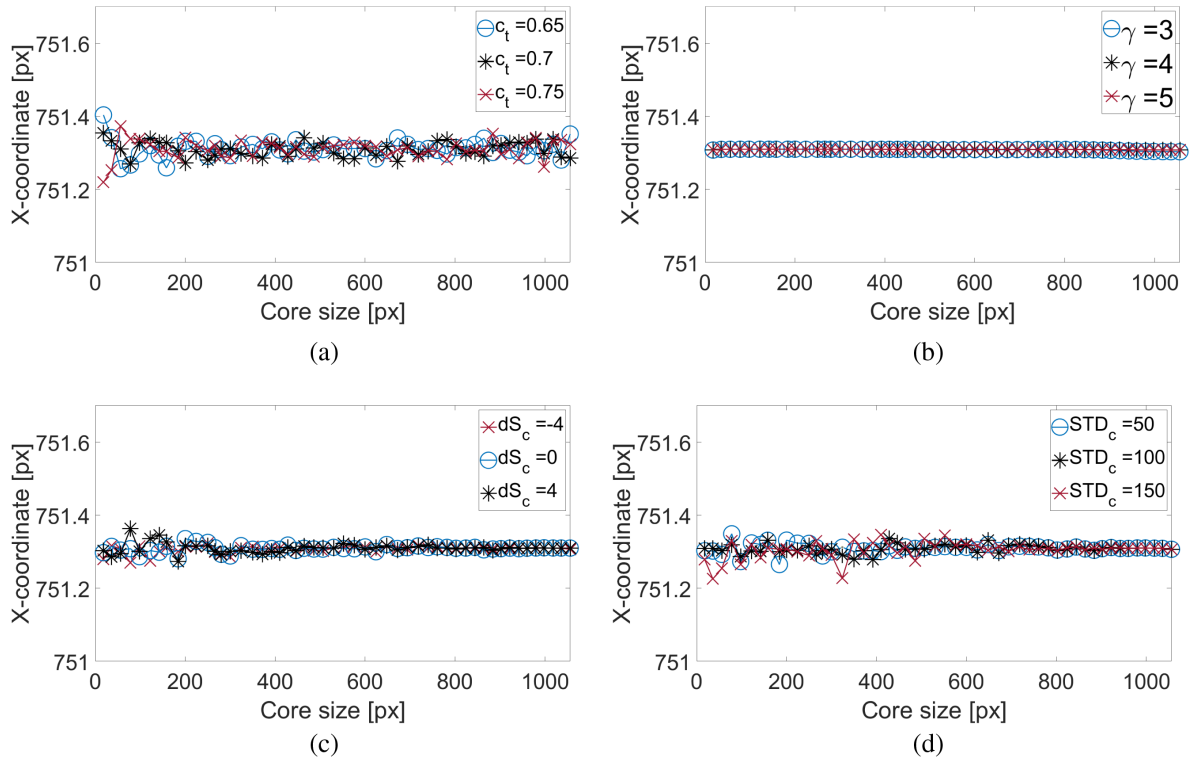


Fig. 7. Detected x-coordinate positions of the SLB for the beams with different core sizes with different values of the algorithm parameters. (a) TCoG with changing c_t, (b) GCoG with changing γ, (c) CORR with changing dS_c, and (d) CORR with changing STD_c.

	Mean [px]	STDp [px]
$c_t = 0.65$	751.312	2.35e-2
$c_t = 0.7$	751.309	2.03e-2
$c_t = 0.75$	751.308	2.68e-2

(a)

	Mean [px]	STDp [px]
$\gamma = 3$	751.309	2.00e-3
$\gamma = 4$	751.310	5.59e-4
$\gamma = 5$	751.309	6.23e-4

(b)

	Mean [px]	STDp [px]
$dS_c = -4$	751.309	1.01e-2
$dS_c = 0$	751.309	9.03e-3
$dS_c = 4$	751.312	1.40e-2

(c)

	Mean [px]	STDp [px]
$STD_c = 50$	751.309	1.30e-2
$STD_c = 100$	751.309	9.03e-3
$STD_c = 150$	751.312	2.50e-2

(d)

Fig. 8. Mean and STDp values of the detected x-coordinates for different values of the algorithm parameters. (a) TCoG with changing c_t, (b) GCoG with changing γ, (c) CORR with changing dS_c, and (d) CORR with changing STD_c.

with a difference of the mean equal to 1.05e-3 px and the STD_p of 9.03e-3 px.

For the HSLB, the mean closest to the reference value for the TCoG, with a difference of 1.24e-3 px, was observed for $c_t = 0.4$, along with the smallest STD_p of 1.20e-3 px. For the GCoG algorithm, the mean with a difference of 1.12e-3 px, and the smallest STD_p of 9.20e-3 px were obtained with $\gamma = 4$. The most precise results for the CORR algorithm were obtained with the precisely measured core size, with a difference of the mean equal to 1.02e-3 px and the STD_p of 1.10e-2 px using $\mathrm{STD}_c = 100$. Increasing the p_{lines} parameter for the POL algorithm improves accuracy and reduces the STD_p. When $p_{\mathrm{lines}} = 50$, the mean and reference value difference is 1.02e-3 px, with an STD_p value of 1.70e-2 px.

Using a sub-optimal parameter value for each algorithm can lead to elevated AE and a reduction in overall robustness. It is observed that the CoG algorithms appear to exhibit greater sensitivity to the parameter selection compared to the CORR algorithm for both types of beams, with the exception of the GCoG, which demonstrates the least susceptibility to the choice of the parameter in the case of the SLB. Regarding the POL algorithm, a reduction in the number of p_{lines} enhances the algorithm's speed, offering advantages in high-speed applications. The time span of the algorithm was linearly increasing with the

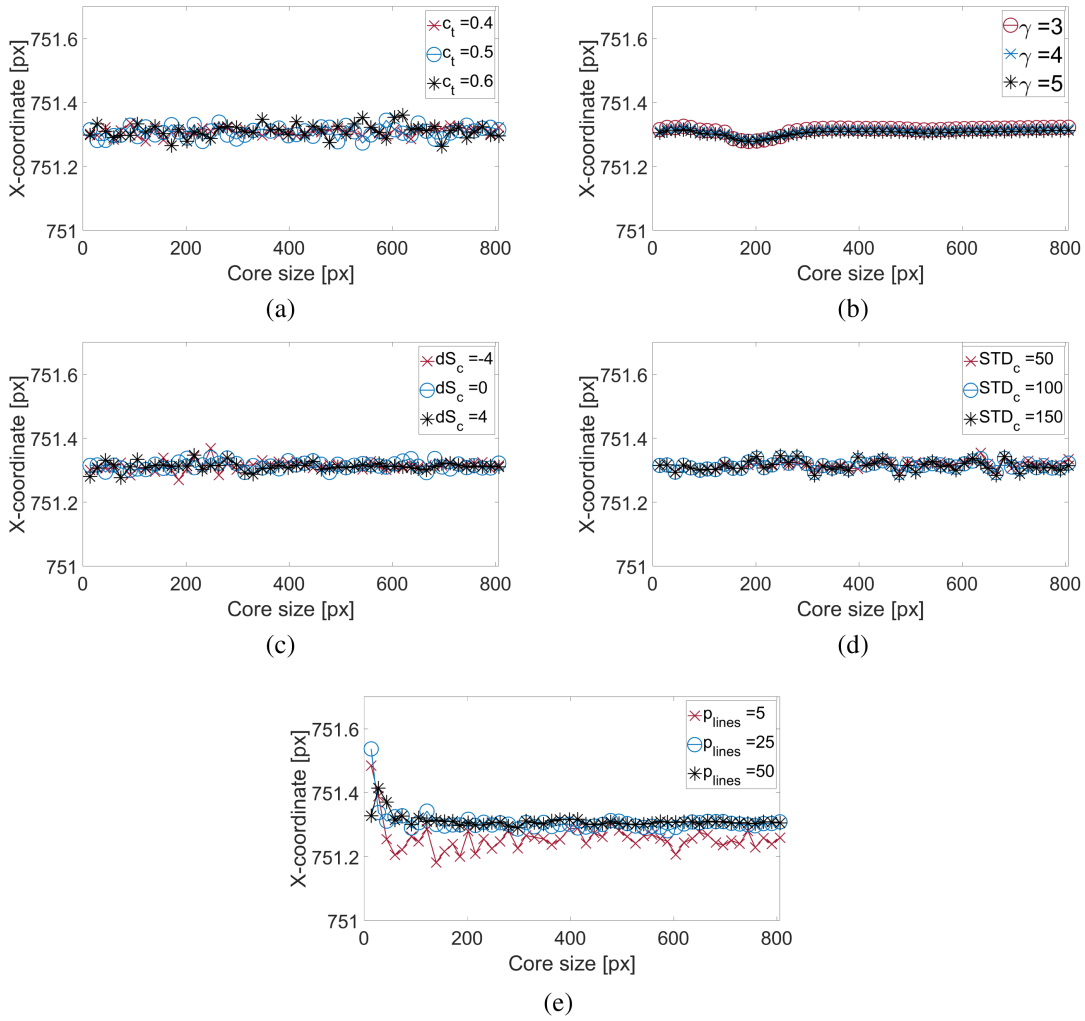


Fig. 9. Detected x-coordinate positions of the HSLB for the beams with different core sizes with different values of the algorithm parameters. (a) TCoG with changing c_t, (b) GCoG with changing γ, (c) CORR with changing dS_c, (d) CORR with changing STD_c, and (e) POL with changing p_{lines}.

number of lines used from 1.2 to 5.9 s. However, this also results in an increase in AE. Using $p_{\mathrm{lines}} = 50$ yielded satisfactory results in terms of the AE.

D. Noise Influence

The impact of noise was investigated by systematically varying the $\mathrm{var}_{\mathrm{noise}}$ of Gaussian white noise while keeping the mean value at zero. Twenty intensity distributions were analyzed, and the mean of the AE was taken for each core size to mitigate the random effects of noise. The error bars are not shown in the graphs, as the standard deviation of the data was lower by one order of magnitude.

For the SLB, the results of TCoG, GCoG, and CORR algorithms with $\mathrm{var}_{\mathrm{noise}}$ values of 1e-4, 5e-4, and 10e-4 can be observed in Fig. 11. The mean absolute error (MAE) and standard deviation of error (STDe) values are presented in Fig. 12. As $\mathrm{var}_{\mathrm{noise}}$ increases, both MAE and STDe show an upward trend for all algorithms. This behavior is also evident in the graphs as the curves shift towards higher absolute error (AE) values and exhibit increased oscillations. The MAE is generally in the order of 1e-2 px for all algorithms. For core sizes larger than 500 px, CORR exhibits similar MAE values to GCoG. However, for smaller core sizes, both AE and oscillations increase significantly, especially for $\mathrm{var}_{\mathrm{noise}} = 10\text{e-}4$, where AE exceeds 0.1 px for several ROI sizes, representing the highest value among all algorithms.

For HSLB, the results of TCoG, GCoG, and CORR algorithms with $\mathrm{var}_{\mathrm{noise}}$ values of 1e-4, 5e-4, and 10e-4 can be seen in Fig. 13. The MAE and STDe values are presented in Fig. 14. Like SLB, increasing $\mathrm{var}_{\mathrm{noise}}$ leads to higher MAE and STDe, as evident from the graphs with curves shifting towards higher AE values and increased oscillations. The MAE is generally in the order of 1e-1 px for all algorithms, except for GCoG, which achieves a minimum of 3.91e-3 px for $\mathrm{var}_{\mathrm{noise}} = 1\text{e-}4$, 7.92e-3 px for $\mathrm{var}_{\mathrm{noise}} = 5\text{e-}4$, and for CORR, which achieves a minimum of 5.32e-2 px for $\mathrm{var}_{\mathrm{noise}} = 1\text{e-}4$. Except for CORR, all algorithms perform significantly worse for small core sizes, particularly with $\mathrm{var}_{\mathrm{noise}}$ values of 5e-4 and 10e-4. In these cases, there is an exponential decrease in performance with core size.

In the majority of cases, algorithms have lower AE for bigger core sizes. The results indicate that for SLB, GCoG is the least

	Mean [px]	STDp [px]
$c_t = 0.4$	751.309	1.20e-2
$c_t = 0.5$	751.307	1.70e-2
$c_t = 0.6$	751.312	2.10e-2

(a)

	Mean [px]	STDp [px]
$\gamma = 3$	751.313	1.25e-2
$\gamma = 4$	751.309	9.20e-3
$\gamma = 5$	751.307	2.10e-3

(b)

	Mean [px]	STDp [px]
$dS_c = -4$	751.314	1.50e-2
$dS_c = 0$	751.311	1.10e-2
$dS_c = 4$	751.313	1.30e-2

(c)

	Mean [px]	STDp [px]
$STD_c = 50$	751.313	1.40e-2
$STD_c = 100$	751.311	1.10e-2
$STD_c = 150$	751.313	1.50e-2

(d)

	Mean [px]	STDp [px]
$p_{lines} = 5$	751.258	4.50e-2
$p_{lines} = 25$	751.307	3.50e-2
$p_{lines} = 50$	751.311	1.70e-2

(e)

Fig. 10. Mean and STDp values of the detected x-coordinates for different values of the algorithm parameters. (a) TCoG with changing c_t, (b) GCoG with changing γ, (c) CORR with changing dS_c, (d) CORR with changing STD_c, and (e) POL with changing p_{lines}.

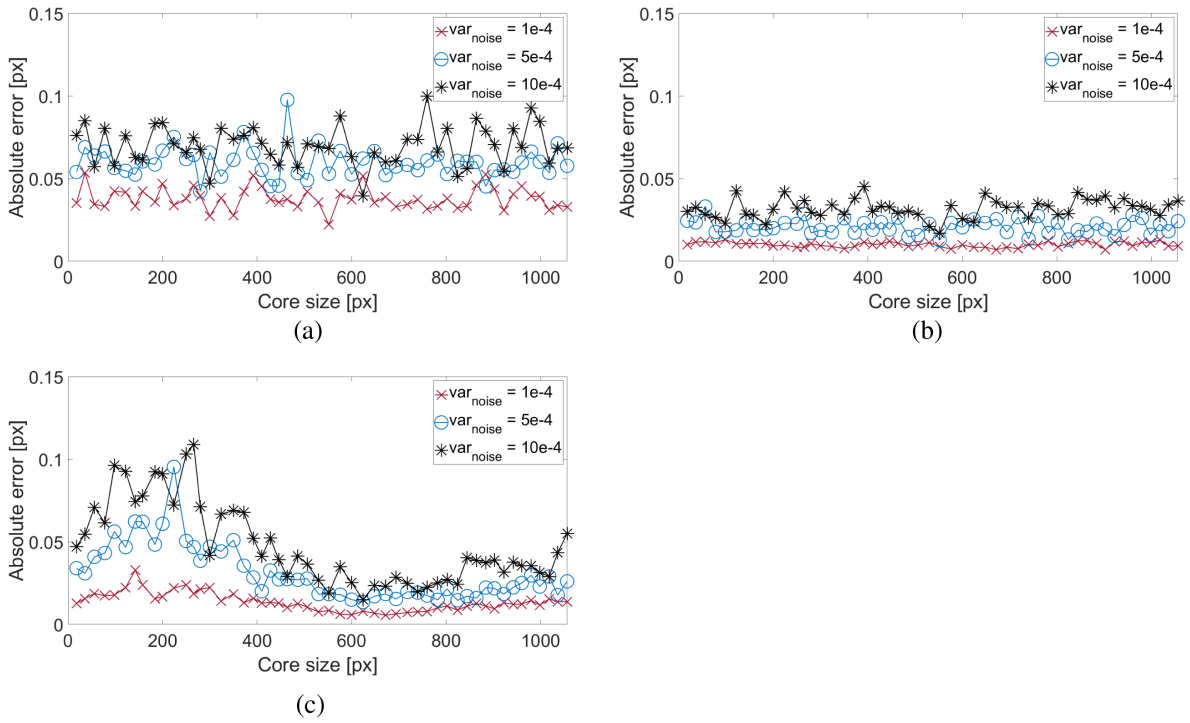


Fig. 11. AE of the (a) TCoG, (b) GCoG, and (c) CORR detecting the centroid of the noised SLB intensity distributions with the $\text{var}_{\text{noise}}$ equal to 1e-4, 5e-4, and 10e-4 px and the size of the core in pixels caused by the camera distance increase from 2 to 102 m.

affected by noise influence, while CORR performs as well as GCoG for core sizes larger than 500 px. TCoG is the most susceptible to noise among the algorithms. For HSLB, all algorithms, except CORR, exhibit significantly poorer performance for small core sizes. This makes CORR the most consistent algorithm, GCoG the least sensitive to noise, and the POL algorithm the most affected by noise.

4. DISCUSSION

The results indicate that the GCoG algorithm is the least affected by algorithm parameter choice and exhibits the highest overall accuracy for SLB. It also demonstrates robustness to noise. For the HSLB, the GCoG algorithm is relatively more sensitive to the choice of the γ parameter. When selected appropriately, it remains the least susceptible to noise, except for core

var_{noise}	MAE [px]	STDe [px]
1e-4	3.99e-2	7.10e-3
5e-4	5.87e-2	8.80e-3
10e-4	7.31e-2	1.23e-2

(a)

var_{noise}	MAE [px]	STDe [px]
1e-4	9.50e-3	1.40e-3
5e-4	2.26e-2	4.20e-3
10e-4	3.25e-2	5.10e-3

(b)

var_{noise}	MAE [px]	STDe [px]
1e-4	1.41e-2	6.70e-3
5e-4	3.06e-2	1.42e-2
10e-4	4.67e-2	2.60e-2

(c)

Fig. 12. MAE and STDe values for the (a) TCoG, (b) GCoG, and (c) CORR detecting the centroid of the noised SLB intensity distributions with the var_{noise} equal to 1e-4, 5e-4, and 10e-4 px.

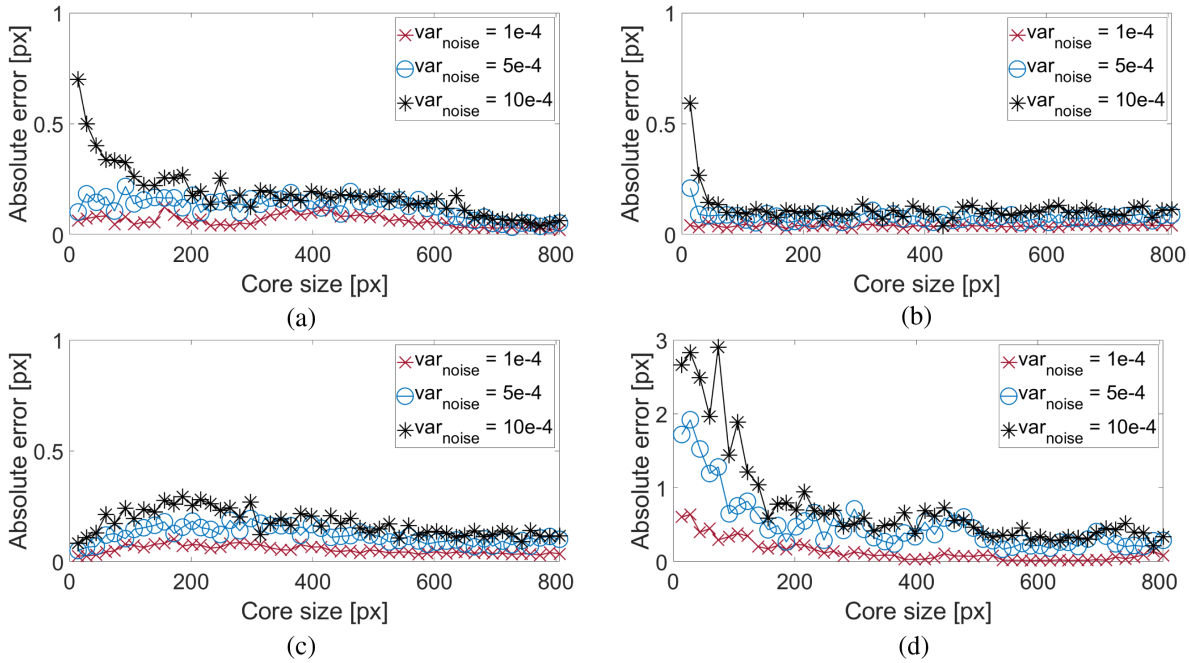


Fig. 13. AE of the (a) TCoG, (b) GCoG, (c) CORR, and (d) POL for detected centroid positions of the noised HSLB intensity distributions with the var_{noise} equal to 1e-4, 5e-4, and 10e-4 px and the size of the core in pixels caused by the camera distance increase from 2 to 102 m. Note that the y-axis scale in (d) is three times higher.

sizes smaller than 30 px. In this case, the CORR algorithm performs better, although its performance is slightly worse for larger core sizes. For SLB, the CORR algorithm shows comparable accuracy to GCoG for core sizes larger than 500 px but performs significantly worse for small core sizes. Additionally, the CORR algorithm consistently exhibits robustness to the choice of S_c and STD_c parameters for both beams.

In comparison, the TCoG algorithm performs with lower accuracy than the GCoG and CORR for both beam types and is also sensitive to the choice of the t parameter. It exhibits significantly poorer performance for HSLBs with small core sizes, especially for var_{noise} equal to 10e-4. The POL algorithm is the most noise-sensitive and yields the lowest accuracy among the algorithms, particularly for small core sizes.

The CoG-based algorithms are considerably faster than CORR and POL, especially when working with high-resolution images. However, the speed of CORR and POL can be increased through windowing without compromising algorithm accuracy. The speed of the CORR algorithm can be enhanced to match the level of CoG-based algorithms. On the other hand, the POL algorithm exhibits significantly lower speed even for small ROI sizes. The speed of CoG-based algorithms can also be improved by windowing but requires a sufficiently large window size to maintain accuracy.

Overall, the centroid-detection-based algorithm errors are approximately one order of magnitude smaller for the SLB than the HSLB when considering noise. The induced error for SLB ranges around 1e-2 px for most algorithms and noise values,

var_{noise}	MAE [px]	STDe [px]
1e-4	6.11e-2	2.64e-2
5e-4	1.24e-1	4.73e-2
10e-4	1.86e-1	1.17e-1

(a)

var_{noise}	MAE [px]	STDe [px]
1e-4	3.91e-2	5.70e-3
5e-4	7.93e-2	2.28e-2
10e-4	1.48e-1	7.47e-2

(b)

var_{noise}	MAE [px]	STDe [px]
1e-4	5.32e-2	1.89e-2
5e-4	1.19e-1	3.67e-2
10e-4	1.73e-1	5.68e-2

(c)

var_{noise}	MAE [px]	STDe [px]
1e-4	1.37e-1	1.48e-1
5e-4	4.99e-1	3.89e-1
10e-4	7.66e-1	6.80e-1

(d)

Fig. 14. MAE and STDe values for the (a) TCoG, (b) GCoG, (c) CORR, and (d) POL detecting the centroid of the noised HSLB intensity distributions with the var_{noise} equal to 1e-4, 5e-4, and 10e-4 px.

while for the HSLB, it is in the order of 1e-1 px. This discrepancy may be attributed to the higher contrast between the core and rings in SLB. CoG-based algorithms only utilize the core of the SLB for detection and rely on the first bright ring of the HSLB, resulting in a smaller area and reduced sensitivity to intensity noise. Even though the POL algorithm performs worst relative to the others, the results suggest that it can be successfully employed in low-noise conditions, where the polarization analysis for centroid detection is favorable, for example, when only part of the beam is visible on the chip or where the intensity is not uniform but where the polarization distribution is preserved.

These results indicate the potential of an SLB and an HSLB for long-distance accelerator alignment, where the required accuracy is typically in the micrometer or tens of micrometer range. It suggests that centroiding algorithms will not be the primary or decisive source of error in the case of relatively high-SNR applications such as accelerator alignment, where the measurement conditions can be controlled.

Funding. Technická Univerzita v Liberci (SGS-2023-3399); CERN (http://dx.doi.org/10.13039/100012470).

Acknowledgment. Portions of this work were presented at the 16th International Workshop on Accelerator Alignment (IWAA 2022), Detection of Structured Laser Beam Centroid and its Use for Alignment. The authors acknowledge the financial support provided by the Knowledge Transfer group at CERN through the KT Fund.

Disclosures. The authors declare no conflicts of interest.

Data availability. Data underlying the results presented in this paper are not publicly available at this time but may be obtained from the authors upon reasonable request.

REFERENCES

1. H. Durand Mainaud, S. B. Jimenez, T. Dijoud, *et al.*, "HL-LHC alignment requirements and associated solutions," in *Proceedings 8th International Particle Accelerator Conference (IPAC)* (2017), pp. 1893–1896.
2. T. Suwada, M. Satoh, S. Telada, *et al.*, "Propagation and stability characteristics of a 500-m-long laser-based fiducial line for high-precision alignment of long-distance linear accelerators," Rev. Sci. Instrum. **84**, 093302 (2013).
3. L. V. Griffith, R. F. Schenz, and G. E. Sommargren, "Magnetic alignment and the Poisson alignment reference system," Rev. Sci. Instrum. **61**, 2138–2154 (1990).
4. D. Kämtner and J. Prenting, "Straight line reference system (SLRS) for the adjustment of the x-ray free-electron laser (XFEL) at DESY," in *9th International Workshop on Accelerator Alignment*, 26–29 September 2006.
5. M. Beker, G. Bobbink, B. Bouwens, *et al.*, "The Rasnik 3-point optical alignment system," J. Instrum. **14**, P08010 (2019).
6. C. Zhang, M. Hasegawa, K. Kanda, *et al.*, "Performance of the iris diaphragm laser alignment system of the spring-8," in *Proceedings of 13th International Workshop on Accelerator Alignment*, Beijing, China, 2014.
7. R. E. Parks, "Practical considerations for using grating produced Bessel beams for alignment purposes," Proc. SPIE **11816**, 11–18 (2021).
8. CERN, "Compact linear collider," https://home.cern/science/accelerators/compact-linear-collider. Accessed 26 August, 2021.
9. G. Stern, "Study and development of a laser based alignment system for the compact linear collider," Ph.D. thesis (ETH Zurich, 2016).
10. J. J. J. Durnin, "Exact solutions for nondiffracting beams. I. The scalar theory," J. Opt. Soc. Am. A **4**, 651–654 (1987).
11. J. Durnin, J. J. Miceli, and J. H. Eberly, "Comparison of Bessel and Gaussian beams," Opt. Lett. **13**, 79–80 (1988).
12. S. N. Khonina, N. L. Kazanskiy, S. V. Karpeev, *et al.*, "Bessel beam: significance and applications—a progressive review," Micromachines **11**, 997 (2020).
13. S. N. Khonina, N. L. Kazanskiy, P. A. Khorin, *et al.*, "Modern types of axicons: new functions and applications," Sensors **21**, 6690 (2021).
14. J.-C. Gayde and M. Sulc, "An optical system for producing a structured beam," (2019).
15. J.-C. Gayde, M. Sulc, and K. Polak, "Introduction to structured laser beam for alignment and status of the R&D," (2022).
16. W. Niewiem, K. Polak, M. Dusek, *et al.*, "Variation of structured laser beam pattern and optimization for an alignment reference line creation," Opt. Express (to be published).
17. M. Dusek, J.-C. Gayde, and M. Sulc, "Wavefront reconstruction of a non-diffracting structured laser beam," Opt. Express **31**, 42099–42110 (2023).
18. R. M. Herman and T. A. Wiggins, "Production and uses of diffractionless beams," J. Opt. Soc. Am. A **8**, 932–942 (1991).
19. A. Abada, M. Abbrescia, S. S. AbdusSalam, *et al.*, "FCC-ee: the lepton collider: future circular collider conceptual design report volume 2," Eur. Phys. J. Spec. Top. **228**, 261–623 (2019).
20. D. M. Gale, "Visual alignment of mechanical structures using a Bessel beam datum: practical implementation," Proc. SPIE **8082**, 1013–1024 (2011).

21. A. M. Nightingale and S. V. Gordeyev, "Shack-Hartmann wavefront sensor image analysis: a comparison of centroiding methods and image-processing techniques," Opt. Eng. **52**, 071413 (2013).
22. H. C. V. Assen, M. Egmont-Petersen, and J. H. C. Reiber, "Accurate object localization in gray level images using the center of gravity measure: accuracy versus precision," IEEE Trans. Image Process. **11**, 1379–1384 (2002).
23. X. Li, X. Li, and C. Wang, "Improvement of correlation-based centroiding methods for point source Shack–Hartmann wavefront sensor," Opt. Commun. **411**, 187–194 (2018).
24. S.-C. Huang, F.-C. Cheng, and Y.-S. Chiu, "Efficient contrast enhancement using adaptive gamma correction with weighting distribution," IEEE Trans. Image Process. **22**, 1032–1041 (2012).
25. J.-C. Yoo and T. H. Han, "Fast normalized cross-correlation," Circuits Syst. Signal Process. **28**, 819–843 (2009).
26. B. Schaefer, E. Collett, R. Smyth, *et al.*, "Measuring the stokes polarization parameters," Am. J. Phys. **75**, 163–168 (2007).

5.183.15.154 {ts '2025-01-30 14:15:27'}

applied optics

Analysis of centroiding algorithms for non-diffracting structured and hollow structured laser beams: erratum

Martin Dusek,[1,2,*] Eva Roikova,[1,2] Dirk Mergelkuhl,[1] Jean-Christophe Gayde,[1] Krystof Polak,[1,2] and Miroslav Sulc[2,3]

[1]The European Organization for Nuclear Research (CERN), Geneva, Switzerland
[2]Technical University of Liberec (TUL), Liberec, Czech Republic
[3]Institute of Plasma Physics of the Czech Academy of Sciences (IPP CAS), Prague, Czech Republic
*martin.dusek@cern.ch

Received 18 July 2024; posted 18 July 2024; published 7 August 2024

This erratum serves to correct an equation in Appl. Opt. 63, 263 (2024). © 2024 Optica Publishing Group. All rights, including for text and data mining (TDM), Artificial Intelligence (AI) training, and similar technologies, are reserved.

https://doi.org/10.1364/AO.535245

1. CORRELATION TEMPLATE MATCHING ALGORITHM

In order to make the Eq. (5) in the original paper [1] clearer, the indexing of the variables was corrected. Normalized 2D correlation function $C(\bar{x}, \bar{y})$ between a squared 2D Gaussian function template $g_t(x, y)$ and the intensity distribution $I(x, y)$ is calculated as

$$C(\bar{x}, \bar{y}) = \frac{\sum_{x,y} |I(x, y) - \overline{I_{u,v}}|[g_t(x - \bar{x}, y - \bar{y}) - \overline{g_t}]}{\left\{\sum_{x,y} |I(x, y) - \overline{I_{u,v}}|^2 \sum_{x,y} [g_t(x - \bar{x}, y - \bar{y}) - \overline{g_t}]^2\right\}^{0.5}}. \quad (5)$$

where $\overline{g_t}$ is the mean of the template intensity and $\overline{I_{u,v}}$ is the mean of the intensity distribution in the region under the feature. The input parameters of the algorithm are the size of the side of the squared template S_c and the standard deviation of the Gaussian function STD_c.

REFERENCE

1. M. Dusek, E. Roikova, D. Mergelkuhl, *et al.*, "Analysis of centroiding algorithms for non-diffracting structured and hollow structured laser beams," Appl. Opt. **63**, 263–274 (2024).

7.4 Generation of Symmetrical Optical Caustic Beams for Precise Alignment

This conference paper presents the first ideas behind generating LBs using cylindrical lenses. It explores the beam characteristics and optimization for long-distance propagation supported by both theoretical modeling and experimental validation. It demonstrates the tunability of beam properties to meet the requirements of long-distance alignment systems. Additionally, it experimentally analyzes the precision of algorithms for detecting an alignment reference plane. These results were presented at the 15th International Particle Accelerator Conference in Nashville, USA (IPAC2024) [119]. Note that use of the detection algorithms on experimental data of LBs was also presented in the proceedings of the International Workshop on Accelerator Alignment held in San Francisco, California, USA (IWAA2024): "Layer beams and their prospect for long-range alignment" [63].

ISBN: 978-3-95450-247-9 ISSN: 2673-5490 doi: 10.18429/JACoW-IPAC2024-THPG35

GENERATION OF SYMMETRICAL OPTICAL CAUSTIC BEAMS FOR PRECISE ALIGNMENT

M. Dusek *,[1], J-Ch. Gayde
The European Organization for Nuclear Research (CERN), Geneva, Switzerland
M. Sulc[1]
Institute of Plasma Physics of the Czech Academy of Sciences, Prague, Czech Republic
[1]also at Technical University of Liberec (TUL), Liberec, Czech Republic

Abstract

Generating layers of symmetrical optical caustic beams using a specific configuration of cylindrical lenses is an innovative idea with potential application in precision alignment and other fields. The technique allows the generation of layers of non-diffracting beams with opposite accelerating directions. This approach can be extended in two dimensions or to create rotationally symmetric beams. Prior methods have produced similar beams using spatial light modulators, but the presented approach with cylindrical lenses reduces setup complexity and cost, thereby opening the possibility for new applications. In the context of particle accelerators, these include particle acceleration using high-power lasers and alignment of accelerator components. The presented research emphasizes the possibility for this technique to be used as a reference line for precise alignment. It allows the generation of reference lines with a thickness in the order of millimeters for distances of tens to hundreds of meters, which is advantageous for large accelerator facilities. A brief description of the sensors used to detect misalignment is also presented.

INTRODUCTION

The phenomenon of optical caustics manifests itself whenever light interacts with curved surfaces, either through reflection or refraction [1, 2]. Optical Caustic Beams (OCB) are characterized by wavefronts that result in beam trajectories causing interference effects which lead to non-diffractive-like properties.

The discovery of Airy Beams (AiB) [3], exhibiting a cubic phase and odd symmetry, initiated the research field of caustic beams. This exploration led to the identification of Symmetric Airy Beams [4] and Symmetric Pearcey Gaussian Beams [5]. These symmetric beams, distinguished by their phase profiles with even symmetry, with cubic phase for the former and with quadratic phase for the latter, have opened new avenues for research. OCBs find applications in particle manipulation [6], acceleration [7], and material processing [8].

Current methods for generating these beams typically involve the use of a spatial light modulator (SLM) to encode the phase profile desired, combined with a lens for spatial Fourier transformation. Various other techniques employ specialized optical components [9, 10]. Recent studies have explored the feasibility of generating non-symmetrical AiBs using readily available cylindrical lenses.

At CERN, there is a significant focus on researching non-diffractive beams for their potential in aligning accelerator components [11–15] and particle acceleration [16], due to unique properties such as low divergence and longitudinal polarization. This contribution focuses on the use of such beams for alignment of accelerator components with respect to a reference line or a plane over long distances. More about the alignment process and about the current state-of-the-art can be read in the work of Mainaud Durand [17].

Given the vast scale of the CERN accelerator complex, there is a need for a simple, scalable, and cost-effective method for generating such beams. This study proposes the use of plano-convex cylindrical lenses to generate layers of OCBs with even phase symmetry, referred to as Layer Beams (LB). The flexibility of this approach is demonstrated by showing how beam properties can be tailored to generate beams that serve as the reference plane for alignment over 140 m.

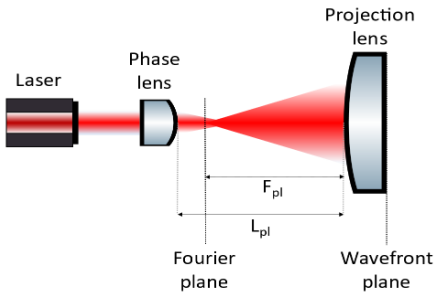


Figure 1: Layer Beam generator.

METHODOLOGY

Layer Beam Generation Principle

The generation of a LB involves a series of cylindrical lenses as seen in Fig. 1. The initial lens, referred to as the phase lens (PhL), is illuminated by a Gaussian beam. Functioning similarly to the spatial light modulator, the lens serves as a phase modulator. The phase of the light undergoes spatial Fourier transformation by the projection lens (PL), which leads to a change of the wavefront directly behind the PL. The line profile of the wavefront can be described by a summation of second-order and fourth-order polynomials. The distance between the lenses (L_{pL}) dictates

* martin.dusek@cern.ch

Content from this work may be used under the terms of the CC BY 4.0 licence (© 2024). Any distribution of this work must maintain attribution to the author(s), title of the work, publisher, and DOI.

ISBN: 978-3-95450-247-9 ISSN: 2673-5490 doi: 10.18429/JACoW-IPAC2024-THPG35

© Content from this work may be used under the terms of the CC BY 4.0 licence (© 2024). Any distribution of this work must maintain attribution to the author(s), title of the work, publisher, and DOI.

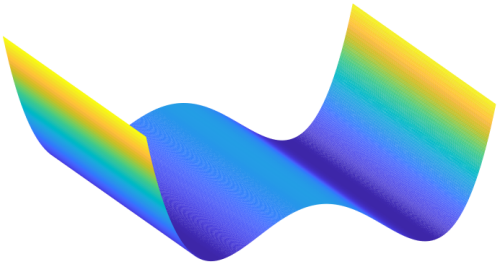


Figure 2: Illustration of the shape of an LB wavefront.

whether the beam will propage to infinity or only over a limited distance. This phase modulation occurs within a specific range of distances behind the phase lens, which is unique to each lens and determined by factors such as refractive index and focal length. An illustration of the shape of an infinitely propagating LP wavefront can be seen in Fig. 2.

It is important to note that a relatively short focal length for the phase lens is necessary to achieve the desired phase modulation. A focal length of 5.79 mm was used in our case. The focal length of the projection lens was 100 mm. The L_{pL} distance was optimized for 140 m propagation, matched to the length of our testing facility. It was ensured that the essential part of the transversal profile of the beam was visible on a camera chip of 14.57 × 12.6 mm.

Adding an additional lens rotated perpendicular to the original in front of the phase lens, increases the length of the pattern. This technique was used in this paper to generate the LB. The rotated lens had the same parameters as the phase lens.

Note that using round lenses with rotational symmetry leads to rotationally symmetric beams with a bright core in the middle such as the Structured Laser Beam [14].

Misalignment Detection

In order to detect the reference plane of the LB, a weighted center of gravity algorithm (first moment weighted by intensity) is used to calculate a centroid coordinate from each row of pixels. The centroid coordinate $\bar{x}$ of the row intensity vector $I(x)$ is calculated as:

$$\bar{x} = \frac{\sum_{x=0}^{x_{max}} I(x)x}{\sum_{x=0}^{x_{max}} I(x)} \quad (1)$$

The thresholding function sets the pixel value to zero when its intensity is lower than the threshold level, and is used to preprocess the intensity vector. The threshold level was set equal to 20% of the maximum intensity of the $I(x)$.

RESULTS

Long Distance Propagation

The LB propagation was simulated in the commercially available software VirtualLab Fusion. The simulated longitudinal and transversal profiles can be seen in the Figs. 3 and 4 respectively. The LB propagation was set to be 140 m and the transversal intensity was detected at 2, 15, 33, and 140 m.

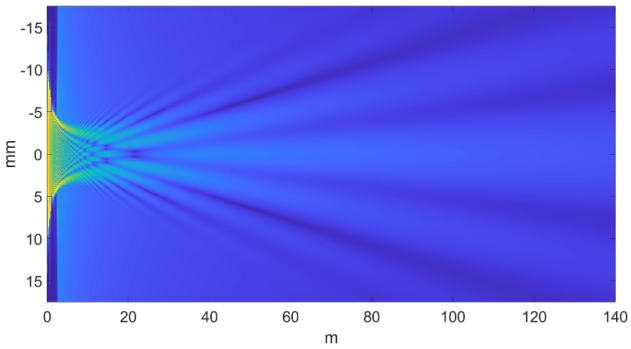
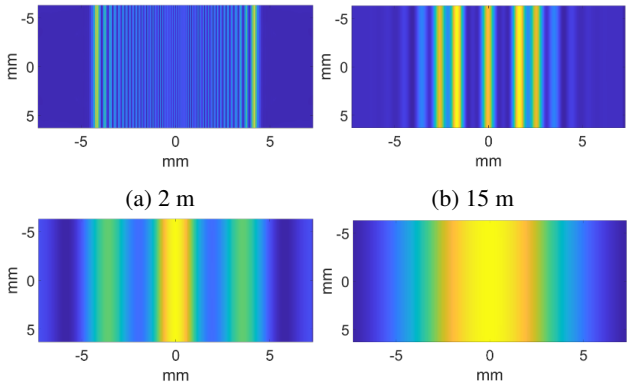


Figure 3: Simulated longitudinal profile of the LB. Contrast enhanced.

The intensity distribution changes rapidly over the first 20 m, but at a distance of 30 m is composed of only three lines. After this distance the pattern does not change but the lines diverge. At 140 m only the central line of the pattern is visible on the detection area.



(a) 2 m (b) 15 m

(c) 46 m (d) 140 m

Figure 4: Simulated transversal profiles at distances of (a) 2 m, (b) 15 m, (c) 46 m and (d) 140 m

A generator with the same properties used for the simulations was constructed, with the resulting beam propagated over 140 m. The measured transversal profiles are shown in Fig. 5. A clear resemblance to the simulation can be seen. The beam is optimized such that the central part of the pattern is visible on the camera, to allow the reference plane to be detected. Even though the decrease in contrast is evident at 140 m, it was still possible to detect the reference plane.

Misalignment Detection

Transversal intensity distributions of different LB patterns measured at 9 m and 52 m were analyzed using the centroiding algorithm, with the results shown in Fig. 6. The centroid from each row is plotted in red, with the fitted average shown in yellow. The algorithm's performance decreases as the number of lines in the image increases. This is seen through the higher spread in centroid points along the fitted average.

ISBN: 978-3-95450-247-9 ISSN: 2673-5490 doi: 10.18429/JACoW-IPAC2024-THPG35

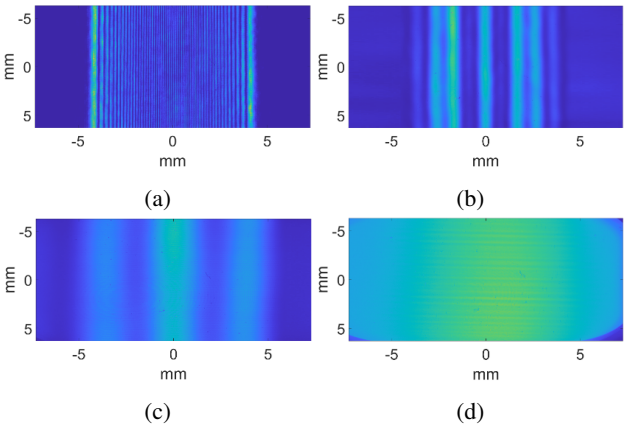


Figure 5: Measured transversal profiles at distances of (a) 2 m, (b) 15 m, (c) 46 m and (d) 140 m

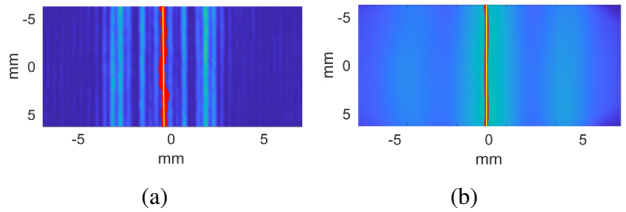


Figure 6: Measured transversal profiles at a distance of (a) 9 m and (b) 52 m analyzed using the centroid algorithm. Red points represent the centroid found for each row, the yellow line the least squared fit of these centroids.

To test the algorithm and its ability to detect misalignment in accelerator components, the LB was propagated inside the pipe over 2 m to mitigate the influence of atmospheric fluctuations in refractive index on the stability of the beam. For future system it is foreseen that the beam will propagate in vacuum so that this effect can be completely neglected. For this test the camera chip was located at the end of the pipe and mounted on a motorized linear stage as illustrated in Fig. 7. The repeatability of the stage movement was in the tenths of µm. The chip was moved perpendicularly to the beam by a known amount, to simulate the misalignment of a component, and this misalignment was simultaneously evaluated using the beam displacement analysis. The chip stayed in one position for several seconds to further mitigate the effect of the atmospheric disturbances by taking the mean detected position from several frames. A projection lens with a focal length of 75 mm was used in this case.

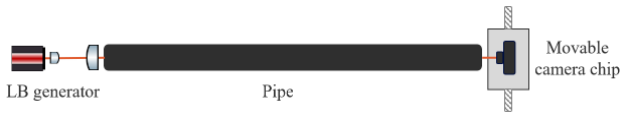


Figure 7: Measurement setup used for misalignment detection over a propagation distance of 2 m.

Figure 8 shows the results of the misalignment detection. The camera was moved transversely backwards and forwards by 10 µm several times with eight frames of data taken over 2 seconds in each position. The mean detected misalignment was 9.67 µm with a standard deviation of 0.71 µm, with the measurement still perturbed by atmospheric variations of the refractive index.

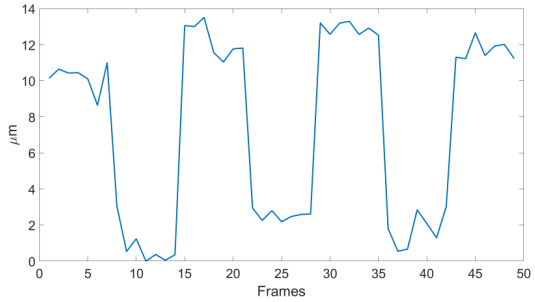


Figure 8: Misalignment detection following 10 µm movement of the camera.

CONCLUSION

This work reports on a study for the potential use of pseudo-non-diffracting Layer Beams in a multi-point straight-line alignment system for particle accelerators. A low-cost method for beam generation was introduced and optimized for propagation over 140 m. The algorithm for analyzing the orientation and position of the reference plane created by such a beam was presented and tested in the laboratory.

Additional experiments will be conducted in future with propagation in vacuum over long distances for a comparison to current state-of-the-art alignment methods at CERN.

ACKNOWLEDGEMENTS

The authors acknowledge the financial support provided by the IPAC2024 student travel grant and by the Knowledge Transfer group at CERN through the KT Fund.

This work was partly supported by the Student Grant Scheme at the Technical University of Liberec through project SGS-2024-3423.

REFERENCES

[1] Y. Kravtsov and Y. Orlov, *Caustics, catastrophes, and wave fields*. 1983, vol. 26, p. 1038. doi:10.1070/PU1983v026n12ABEH004582

[2] J. F. Nye, *Natural Focusing and Fine Structure of Light: Caustics and Wave Dislocations*. CRC Press, 2000. doi:10.1119/1.19543

[3] G. A. Siviloglou *et al.*, "Observation of accelerating airy beams," *Physical Review Letters*, vol. 99, p. 213 901, 2007. doi:10.1103/PhysRevLett.99.213901

[4] P. Vaveliuk *et al.*, "Symmetric airy beams," *Optics Letters*, vol. 39, pp. 2370–2373, 2014. doi:10.1364/OL.39.002370

[5] Y. Wu *et al.*, "Symmetric pearcey gaussian beams," *Optics Letters*, vol. 46, pp. 2461–2464, 2021. doi:10.1364/OL.425889

Content from this work may be used under the terms of the CC BY 4.0 licence (© 2024). Any distribution of this work must maintain attribution to the author(s), title of the work, publisher, and DOI.

ISBN: 978-3-95450-247-9 ISSN: 2673-5490 doi: 10.18429/JACoW-IPAC2024-THPG35

© Content from this work may be used under the terms of the CC BY 4.0 licence (© 2024). Any distribution of this work must maintain attribution to the author(s), title of the work, publisher, and DOI.

[6] P. Zhang *et al.*, "Trapping and guiding microparticles with morphing autofocusing airy beams," *Optics Letters*, vol. 36, pp. 2883–2885, 2011. doi:10.1364/OL.36.002883

[7] J. Li *et al.*, "Vacuum electron acceleration driven by two crossed airy beams," *Optics Letters*, vol. 36, pp. 648–650, 2011. doi:10.1364/OL.36.000648

[8] D. G. Papazoglou *et al.*, "Materials processing using abruptly autofocusing beams," in *CLEO: Science and Innovations*, Optica Publishing Group, 2013, CM3H–8. doi:10.1364/CLEO_SI.2013.CM3H.8

[9] J. Wang *et al.*, "Generation of high quality airy beams with blazed micro-optical cubic phase plates," *Applied Optics*, vol. 50, pp. 6627–6631, 2011. doi:10.1364/AO.50.006627

[10] B. Yalizay, B. Soylu, and S. Akturk, "Optical element for generation of accelerating airy beams," *JOSA A*, vol. 27, pp. 2344–2346, 2010. doi:10.1364/JOSAA.27.002344

[11] W. Niewiem *et al.*, "Variation of structured laser beam pattern and optimization for an alignment reference line creation," *Optics Express*, vol. 31, pp. 43 307–43 322, 2023. doi:10.1364/OE.503016

[12] M. Dusek *et al.*, "Analysis of centroiding algorithms for non-diffracting structured and hollow structured laser beams," *Applied Optics*, vol. 63, pp. 263–274, 2024. doi:10.1364/ao.509927

[13] M. Dusek, J.-C. Gayde, and M. Sulc, "Wavefront reconstruction of a non-diffracting structured laser beam," *Optics Express*, vol. 31, pp. 42 099–42 110, 2023. doi:10.1364/oe.502452

[14] J.-C. Gayde and M. Sulc, "An Optical System for Producing a Structured Beam (European Patent No. EP3564734)," EP3564734, 2019.

[15] J.-C. Gayde *et al.*, "The potential contribution of a structured laser beam to accelerator alignment technology," in *Proc. IPAC'23*, Venice, Italy, 2023, pp. 4044–4046. doi:10.18429/JACoW-IPAC2023-THPA041

[16] K. Polak, J.-C. Gayde, and M. Sulc, "3D polarisation of a structured laser beam and prospects for its application to charged particle acceleration," in *Proc. IPAC'23*, Venice, Italy, 2023, pp. 1443–1445. doi:10.18429/JACoW-IPAC2023-TUPA047

[17] H. M. Durand *et al.*, "HL-LHC Alignment Requirements and Associated Solutions," in *Proc. IPAC'17*, Copenhagen, Denmark, May 2017, pp. 1893–1896. doi:10.18429/JACoW-IPAC2017-TUPIK085

7.5 Generation of Pseudo-Nondiffracting Symmetrical Layer Beams Using Cylindrical Lenses

This paper describes a technique for generating one- and two-dimensional LBs, utilizing a specific configuration of plano-convex cylindrical lenses. The study presents both theoretical modeling and experimental validation of the beam generation method. It also describes the principle behind the beam generation in detail and facilitates intuitive understanding. The results highlight the tunability of the beam size, propagation distance, or shape of the transversal intensity distribution for the needs of alignment systems. This paper was published in Optics Express (Q2, Impact Factor = 3.2).

Research Article Vol. 32, No. 24 / 18 Nov 2024 / Optics Express 42368
Optics EXPRESS

Generation of pseudo-nondiffracting symmetrical Layer beams using cylindrical lenses

MARTIN DUŠEK,[1,2,*] SEBASTIAN FIGURA,[1,3] JEAN-CHRISTOPHE GAYDE,[1] AND MIROSLAV ŠULC[2,4]

[1]The European Organization for Nuclear Research (CERN), Geneva, Switzerland
[2]Technical University of Liberec (TUL), Liberec, Czech Republic
[3]Cracow University of Technology (CUT), Cracow, Poland
[4]Institute of Plasma Physics of the Czech Academy of Sciences (IPP CAS), Prague, Czech Republic
*martin.dusek@cern.ch

Abstract: The pseudo-nondiffracting behavior of optical caustic beams makes them potentially useful in precise component alignment at CERN. This paper introduces an innovative method for generating one and two-dimensional symmetrical Airy-like beams, known as Layer beams, utilizing a specific configuration of plano-convex cylindrical lenses. Simulations and experimental results have validated this method, demonstrating its potential for scalable and cost-effective beam production with tunable properties, making it practical for a wide range of scientific applications.

Published by Optica Publishing Group under the terms of the Creative Commons Attribution 4.0 License. Further distribution of this work must maintain attribution to the author(s) and the published article's title, journal citation, and DOI.

1. Introduction

Optical caustic is a well-known phenomenon present in everyday life every time light is reflected or refracted by curved surfaces [1,2]. Similarly, optical caustic beams (OCB) [3] are characterized by wavefronts, hence ray envelopes, which cause the rays to overlap in a specific way creating caustic beam trajectories, due to the superposition of different wavefront parts. These beams exhibit interesting properties, including pseudo-nondiffracting behavior and the capacity for regeneration beyond obstacles.

The behavior of OCBs can be explained by catastrophe theory, where the ray envelopes are structurally stable singularities. It allows for the so-called fold and cusp caustics. An example of fold-type caustics is an Airy beam [4], having the ray envelope characterized by a cubic power. After their subsequent empirical validation [5], extensive research has been dedicated to elucidating the properties and exploring the diverse applications of such beams. These include light-sheet microscopy [6], particle manipulation [7], plasma channel generation [8], and other areas [9].

Cusp-like beams are characterized by even symmetry of the ray envelope. Examples of these beams are the symmetric Airy beams [10,11], the Pearcey-Gaussian beams [12], and the symmetric Swallowtail beams [13]. They can be imagined as two Airy-like beams with opposing acceleration directions.

The state-of-the-art approach to generating the aforementioned beams involves using a Gaussian beam incident on a spatial light modulator encoded with an angular phase of the desired beam, coupled with a lens performing a spatial Fourier transformation, or by encoding a computer-generated hologram on the spatial light modulator [5,10,11,13]. Alternatively, diverse methodologies utilizing specialized off-the-shelf components were shown [14–23]. Although previous studies have reported the potential for straightforward Airy-like beam generation using

#537554 https://doi.org/10.1364/OE.537554
Journal © 2024 Received 26 Jul 2024; revised 20 Sep 2024; accepted 22 Sep 2024; published 5 Nov 2024

Optics EXPRESS

standard cylindrical lenses [24–27], the generation of cusp caustic beams through a similar approach remains unexplored, as far as our knowledge extends.

At CERN, pseudo-nondiffracting beams are currently under extensive investigation regarding their utility in aligning accelerator components [28–31] and particle acceleration applications [32]. OCBs, with their distinctive properties, hold promise to be used as a multi-point reference for the alignment of accelerator parts at CERN similar to the wire positioning and hydrostatic leveling system [33]. Our previous research focused on the use of the so-called Structured laser beam [28,34] for this purpose, which can generate a reference line. Layer beams offer an advantage in multi-point alignment as they create a reference plane, which can ease the detection of multiple points at one moment in time over a long distance. Given the vast nature of the accelerator complex, a simple, scalable, and cost-effective solution for generating such beams is highly desirable. This paper presents a novel method for generating so-called one-dimensional and two-dimensional beams, using various configurations of plano-convex cylindrical lenses. These beams, referred to as Layer beams, address the specified requirements.

2. Methodology

The generation of a Layer beam involves a series of cylindrical lenses, as depicted in Fig. 1. The initial lens in the sequence, referred to as the phase lens, is illuminated by a Gaussian beam. This lens functions analogously to a spatial light modulator, acting as an angular phase modulator in the spectral domain. Consequently, the light in the Fourier plane located at the focal length F_{PL} of the projection lens, and in the distance L_{Ph} from the phase lens, undergoes a spatial Fourier transformation by the projection lens [35].

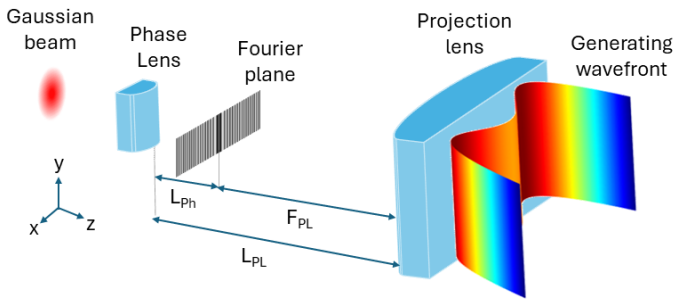


Fig. 1. One-dimensional Layer beam generator.

The generation principle can also be explained by analyzing the phase delay that is introduced by the generator, which results in the creation of a so-called generating wavefront directly behind the projection lens. This enables the intersection of rays, resulting in the creation of a beam with desired properties through the superposition of different parts of the generating wavefront.

The Layer beams can be characterized either through the angular spectrum behind the phase lens or by the generating wavefront directly behind the projection lens. In the context of this paper, the generating wavefront approach is preferred in most of the explanations due to the generation principle using cylindrical lenses, as it can be measured using a wavefront sensor.

The generating wavefront dictates the caustic structure of the beam. Its shape is influenced by the distance L_{PL} between the lenses and their parameters, such as focal length or refractive index. Note that the distance L_{PL} also determines which phase plane undergoes the spatial Fourier transformation by the projection lens. The line profile of the generating wavefront can be

Optics EXPRESS

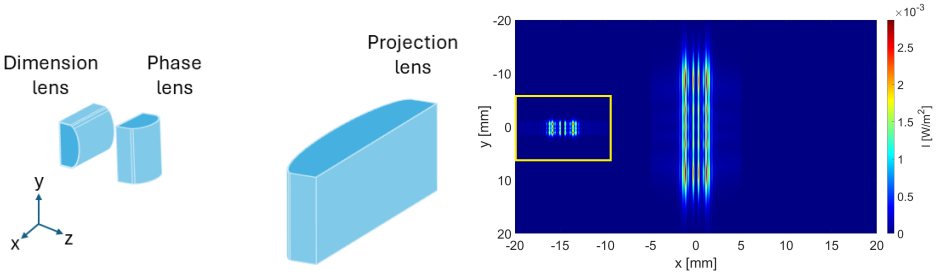
described using the equation:

$$W(x) = K_1 x^2 + \sum_{m=1}^{\infty} K_{m+1} x^{2(m+1)} \tag{1}$$

Equation (1) is directly related to optical aberrations induced by the lenses and by their position, specifically, the term with the squared power relates to defocus, and higher-order even terms correspond to various orders of spherical aberration. A change of the distance L_{PL} influences mainly the amount of the defocus in the system, which causes the generating wavefront to change shape, as will become evident in the following chapters.

Equation (1) describes the line profile of the generating wavefront of Layer beams. The line profile of the wavefront remains consistent when analyzed along the y-axis, as illustrated in Fig. 1. Consequently, describing the beam using the line profile alone is sufficient. This results in the formation of parallel lines in the transversal intensity distribution.

An additional cylindrical lens, rotated by 90 degrees around the optical axis, can be placed in front of the phase lens, as shown in Fig. 2(a). This lens is referred to as the dimension lens. This yields one-dimensional beams with the same profile of the transversal intensity distribution along the x-axis as if the dimension lens was not used, but with significantly elongated lines along the y-axis, as illustrated in Fig. 2(b). The length of these lines can be adjusted by varying the focal length and position of the dimension lens along the z-axis as it alters the divergence of the beam along the y-axis. This configuration can be beneficial in long-distance multi-point alignment applications as the size of the reference plane generated by the beam increases.



(a) (b)

Fig. 2. (a) One-dimensional Layer beam generator with a dimension lens. (b) Simulated one-dimensional Layer beam prolonged in the y-axis generated using a generator with the dimension lens. A one-dimensional Layer beam is generated using the generator without the dimension lens for comparison in the yellow rectangle.

The equation can be extended to two dimensions by superposing two one-dimensional beams rotated by 90 degrees around the optical axis, generating two-dimensional Layer beams. Such beams can be created using a generator consisting of two phase lenses and two projection lenses, each additional lens rotated by 90 degrees around the optical axis, as illustrated in Fig. 3.

Extending the equations to cylindrical coordinates yields a so-called Structured laser beam [28,34], which can be generated using lenses with rotational symmetry. This beam has an intense central core surrounded by rings, which resembles the intensity distribution of a Bessel beam [36]. In our previous works, the generation method using a high refractive index ball lens, as the phase lens, together with a plano-convex lens, as the projection lens, was demonstrated.

All of the caustic beams described above can also be generated using a reflective or transmissive optical element, which would induce a phase delay similar to that of a generating wavefront. This could be achieved with a glass plate [16] or with a mirror [18]. However, the presented approach

Optics EXPRESS

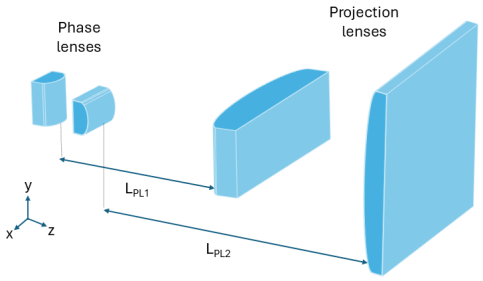


Fig. 3. Generator of two-dimensional Layer beams consisting of two phase and two projection lenses.

using a set of lenses allows for simple tunability of beam parameters by merely changing the L_{PL} distance.

3. Results

3.1. Simulations

To analyze the generator and beam properties, numerical simulations were performed using the commercially available software VirtualLab Fusion, which combines ray tracing and electromagnetic field propagation calculations. The simulated generator consisted of a plano-convex cylindrical phase lens with a focal length of 5.79 mm and another plano-convex cylindrical projection lens with a focal length of 20 mm. The lens material was N-BK7 glass. A Gaussian beam with a wavelength of 532 nm was used as a source and entered the system with a planar wavefront.

The dependence of the coefficients K_1 and K_2 of Eq. (1) on the distance L_{PL} can be seen in Fig. 4. Only the second and fourth power coefficients in Eq. (1) were used to model the wavefront line profile, as it yielded a sufficiently precise approximation. The line profile of the generating wavefront together with the longitudinal intensity distribution for different distances L_{PL} can be seen in Fig. 5 together with transversal intensity profiles at 0.4, 0.8, 1.2, and 1.6 m away from the generator in Fig. 6.

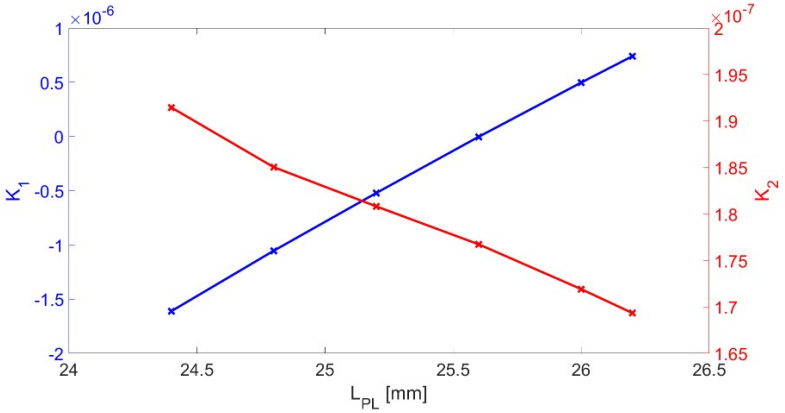


Fig. 4. Values of coefficients K_1, K_2 of Eq. (1) with respect to the L_{PL} distance.

Optics EXPRESS

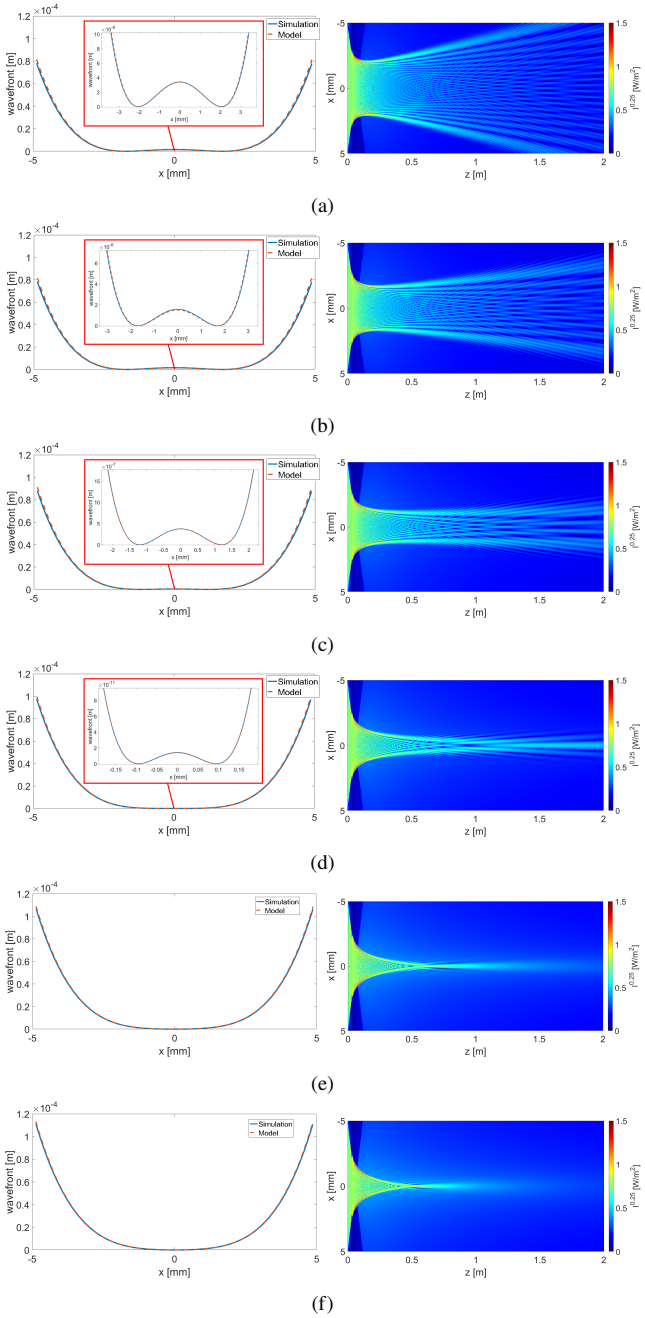


Fig. 5. A generating wavefront with the modeled wavefront according to Eq. (1) (left) and longitudinal intensity profile (right) for the L_{PL} distance of (a) 24.4 mm, (b) 24.8 mm, (c) 25.2 mm, (d) 25.6 mm, (e) 26.0 mm, and (f) 26.2 mm. The intensity was enhanced for better visibility.

Optics EXPRESS

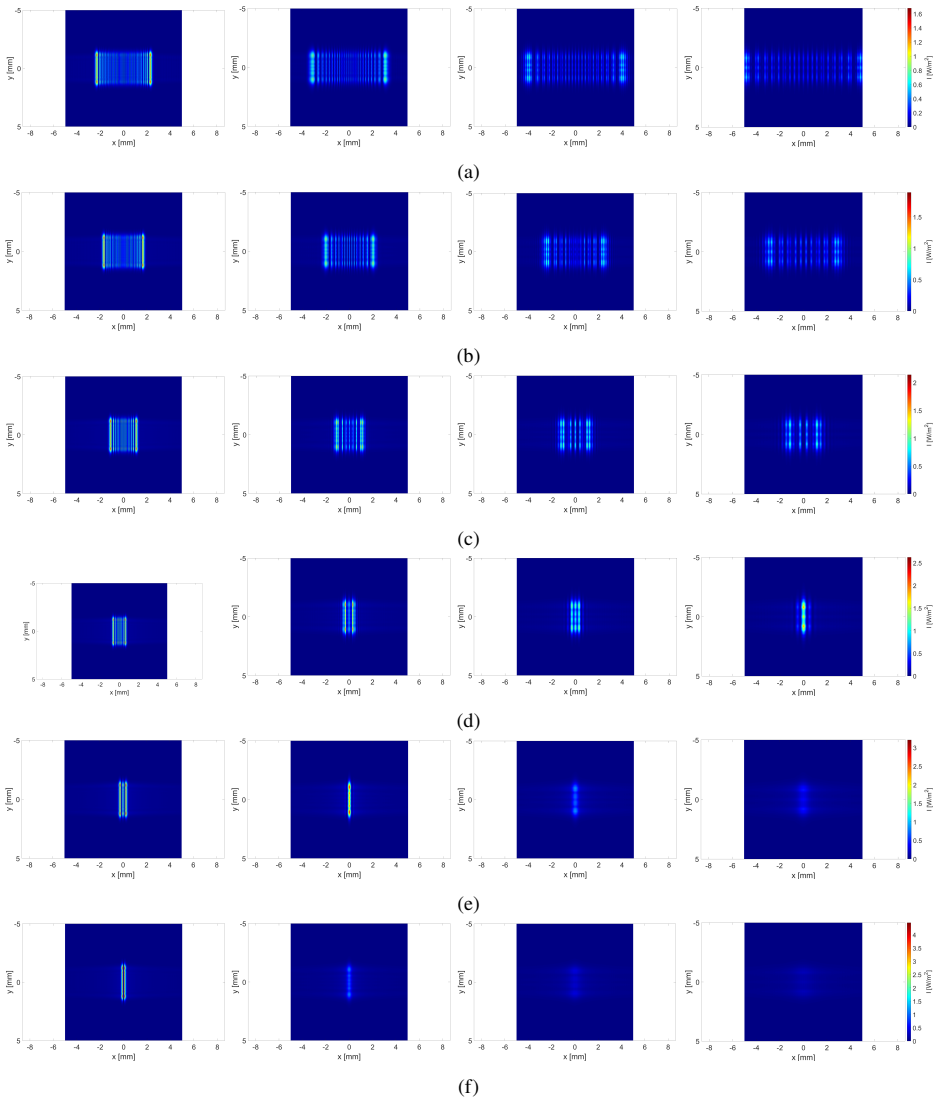


Fig. 6. Transversal intensity profile of one-dimensional Layer beams at the distance of 0.4 m, 0.8 m, 1.2 m and 1.6 m from the generator for the distance L_{PL} equal to (a) 24.4 mm, (b) 24.8 mm, (c) 25.2 mm, (d) 25.6 mm, (e) 26.0 mm, and (f) 26.2 mm.

Optics EXPRESS

The wavefront for the L_{PL} distances equal to 26.2 and 26.0 mm is converging. The coefficients K_1 and K_2 in Eq. (1) are both positive, hence the generating wavefront has no local extremes, and the beams propagate over a limited distance. As the L_{PL} distance increases, the beam travels over a shorter distance due to the higher slope of the wavefront, which is caused mainly by the change of the defocus coefficient K_1. This can be seen in Figs. 5(e), 5(f), 6(e), and 6(f).

Once the distance L_{PL} gets shorter than 25.6 mm the generating wavefront takes on a "sombrero" shape with two local minima and local maximum at the optical axis. The local minima get farther apart as the L_{PL} distance shortens and the absolute phase difference between the local minimum and maximum increases. This is caused by the fact that the defocus coefficient K_1 becomes negative and decreases as the distance L_{PL} shortens, while the spherical aberration coefficient K_2 remains positive (Fig. 4). These beams propagate to infinity (Figs. 5(a), 5(b), 5(c), 5(d), 6(a), 6(b), 6(c) , and 6(d)).

A more detailed analysis of the generating wavefront shape provides further insight into the propagation properties of the Layer beam. It is possible to trace the rays starting from the wavefront as according to the Eikonal equation, the rays are locally perpendicular to it [37]. Different parts of the generating wavefront are illustrated in Fig. 7. Regions of the Layer beam along the propagation distance are shown in Fig. 8. The intensity distribution of the beam undergoes rapid changes in the near zone, where a significant number of rays from the outer parts of the wavefront intersect with rays from other parts of the wavefront. In this area, the beam exhibits pseudo-nondiffracting properties and can regenerate behind reasonably sized obstacles, provided the obstacle does not block the majority of the beam. The outer part of the beam exhibits strong curvature. Conversely, in the diverging zone, the transversal intensity distribution remains unchanged, only diverging as rays from regions with low wavefront gradients intersect. The outer part of the beam straightens in this zone.

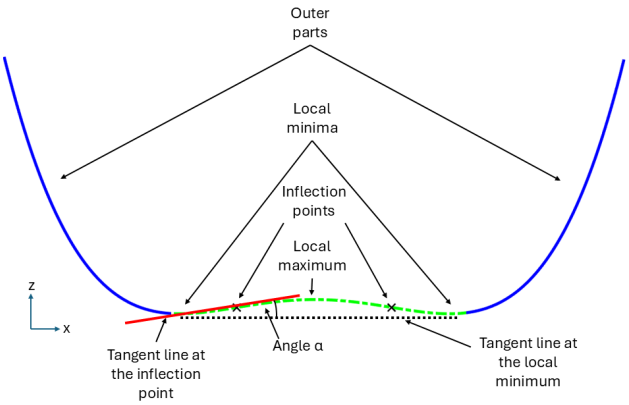


Fig. 7. Description of the generating wavefront regions.

Figures 9(a), 9(b), and 9(c) show rays originating from the generating wavefront, along with the corresponding longitudinal profiles, for propagation distances L_{PL} of 24.4, 25.6, and 26.0 mm, respectively. As mentioned in the previous text, the Layer beam is composed of two Airy-like beams with opposing acceleration directions. As the outer parts of the Airy-like beams straighten, rays originating from inflection points begin to align with the outer parts of the beam. These rays are plotted in red.

Figure 5 illustrates that the absolute phase difference between local minima and maxima increases by several orders of magnitude as the distance L_{PL} decreases. Additionally, local minima get farther apart, although only by approximately one order of magnitude. This leads to a steeper wavefront slope at the inflection points, resulting in an increase of the angle α (Fig. 7).

Optics EXPRESS

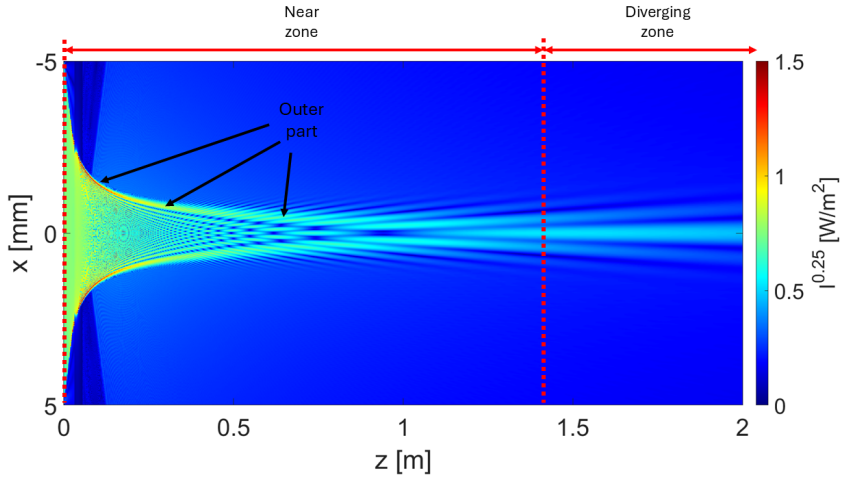


Fig. 8. Different regions along the Layer beam propagation distance.

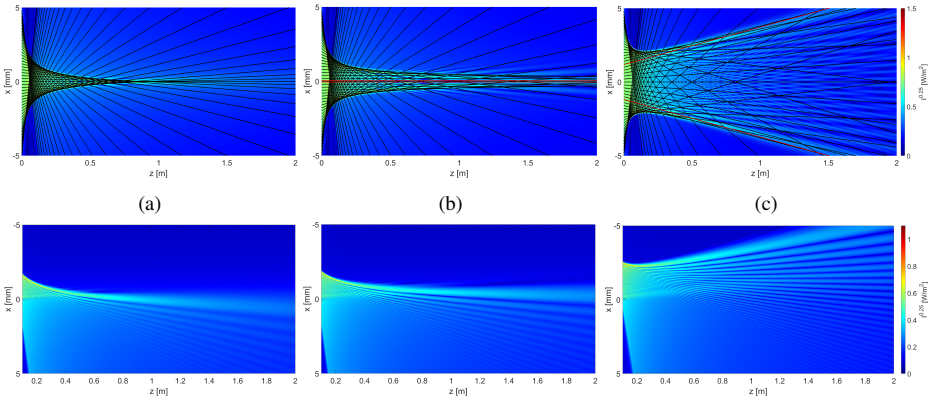


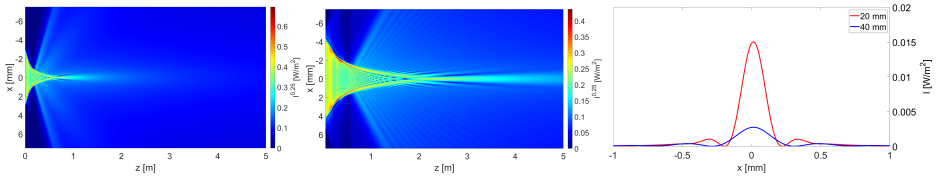
Fig. 9. Longitudinal profiles of one-dimensional Layer beams with rays plotted in black along with rays originating from inflection points in red for the distances L_{PL} equal to (a) 26.0 mm, (b) 25.6 mm, and (c) 24.4 mm. The longitudinal profiles on one of the Airy-like beams that form the Layer beam for the distances L_{PL} equal to (d) 26.0 mm, (e) 25.6 mm, and (f) 24.4 mm. The intensity was enhanced and profiles of Airy-like beams slightly zoomed in for better visibility.

Optics EXPRESS

Consequently, the outer regions of the Airy-like beams turn farther apart. The Airy-like beams that constitute the Layer beam at the respective distances L_{PL} are illustrated in Figs. 9(d), 9(e), and 9(f). It is evident that the beams turn farther and farther apart from the optical axis as the distance L_{PL} decreases. Due to this, as the distance L_{PL} shortens even more the contrast of the lines decreases until it is not possible to distinguish the line pattern at the optical axis.

For the distance L_{PL} of 26.0 mm, the beam's wavefront is entirely converging (Fig. 5(e)), with no local extrema or inflection points. The straight outer regions of the Airy-like beam intersect the optical axis, resulting in a rapid loss of power in the paraxial region and preventing the beam from propagating to infinity (Fig. 9(d)). The beam propagates only in the near zone and keeps its pseudo-nondiffracting properties along the whole propagation length.

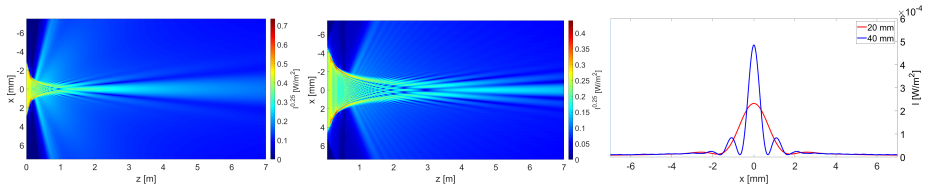
Simulated longitudinal profiles of finite Layer beams, generated using projection lenses with focal lengths (F_{PL}) of 20 mm and 40 mm, are depicted in Fig. 10. The distance L_{Ph} was fixed for both beams at 6 mm, therefore, both beams originate from the same angular phase delay in the spectral domain. As a result, the beams exhibit similar characteristics with finite propagation distances but differ in spatial scaling. The spatial scaling of the Fourier transformation is influenced by the focal length of the projection lens [35], resulting in larger spatial dimensions for beams produced with longer focal lengths. Transversal line profiles were taken at the distance of 0.8 m and 2.5 m, so the generated transversal pattern remained as similar as possible for both beams. A shorter focal length of the projection lens produces a smaller overall beam with finer features.



(a) (b) (c)

Fig. 10. Simulated longitudinal profile of finite one-dimensional Layer beams generated using focal length of the projection lens equal to (a) 20 mm, (b) 40 mm for the L_{Ph} of 6 mm. (c) Transversal intensity profile at the distance of 0.8 m from the generator for the focal length of 20 mm, and at 2.5 m from the generator for the focal length of 40 mm.

When a beam propagates to infinity, the stable diverging part of the beam forms at a greater distance for longer focal lengths of the projection lens. As a result, the pattern formed in the diverging region exhibits smaller features. This phenomenon is particularly significant for long-distance alignment, where propagation distances can extend to tens or hundreds of meters. This effect is illustrated in Fig. 11, where the projection lens with a focal length of 40 mm



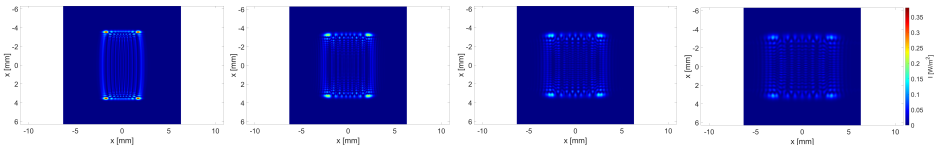
(a) (b) (c)

Fig. 11. Simulated longitudinal profile of infinitely propagating one-dimensional Layer beams generated using focal length of the projection lens equal to (a) 20 mm, (b) 40 mm for the L_{Ph} of 5.6 mm. (c) Transversal line profile at the distance of 7 m from the generator.

Optics EXPRESS

produces a beam with finer features at a distance of 7 m, compared to a focal length of 20 mm. The distance L_{Ph} for both beams was equal to 5.6 mm.

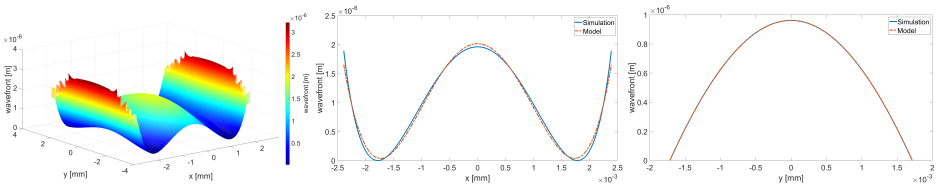
Transversal intensity profiles of a simulated two-dimensional Layer beam at the distance of 1, 1.5, 2, and 2.5 m from the generator are shown in Fig. 12. An additional phase lens with the same parameters was added, along with a projection lens with a focal length of 50 mm, rotated 90 degrees around the optical axis (Fig. 3) with the distance L_{PL1} = 28.6 mm, and the distance L_{PL2} = 55.9 mm. This leads to the creation of a pattern that is composed of two orthogonal Layer beams. At 1.5 m (Fig. 12(a)), noticeable field distortion occurs due to the beam passing through the projection lens, manifesting as curved lines in the pattern. However, this effect diminishes as the beam propagates further.



(a) (b) (c) (d)

Fig. 12. Transversal intensity profiles of a simulated two-dimensional Layer beam at: (a) 1 m, (b) 1.5 m, (c) 2 m and (d) 2.5 m.

The generating wavefront of the two-dimensional beam, along with simulated and modeled line profiles according to Eq. (1), are depicted in Fig. 13. The coefficient values are K_1 = -1.32e-6 and K_2 = 2.20e-7 for the x-axis, and K_1 = -3.43e-7 and K_2 = 5.59e-9 for the y-axis. The modeled wavefront along the x-axis does not perfectly match the simulated one due to field distortion caused by the additional projection lens.



(a) (b) (c)

Fig. 13. (a) Simulated generating wavefront for the two-dimensional Layer beam. (b) Line profile of the generating wavefront along the x-axis, and (c) line profile along the y-axis, with modeled wavefronts according to Eq. (1).

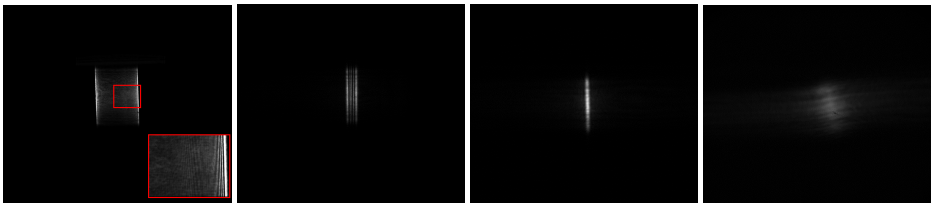
3.2. Measurements

Several Layer beams were generated in the laboratory using the generator with the same parameters as the ones used for the simulations. The phase lens with a focal length of 5.79 mm was used together with the projection lens with a focal length equal to 20 mm. The size of the CMOS sensor was 14.57 mm x 12.6 mm and the wavelength of the Gaussian beam was 532 nm. The wavefront was measured using a Shack-Hartman sensor and reconstructed using an in-house developed software [38]. The sensor was moved as close as possible to the generator, hence the measurement of the generating wavefront was done almost directly behind the projection lens. So-called zonal reconstruction was used which allows for reconstruction of the wavefront in the entire microlens array [38,39].

Transversal intensity profiles of the one-dimensional Layer beam propagating over a limited distance are shown in Fig. 14. The distance L_{PL} was equal to 26.15 mm. Initially, a fine structure

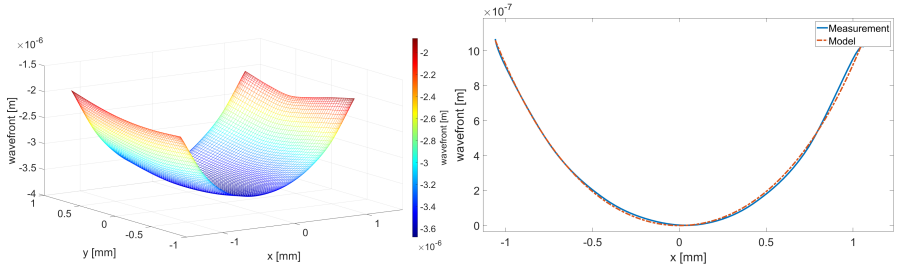
Optics EXPRESS

of lines is observed at a distance of 0.07 m (Fig. 14(a)). As the beam continues to propagate, the number of lines decreases (Figs. 14(b) and 14(c)) until a clear structure is not visible on the camera in 1.3 m (Fig. 14(d)), while only a low-intensity residual can be seen. The measured generating wavefront for the aforementioned beam can be seen in Fig. 15(a) along with the line profile together with the modeled wavefront according to Eq. (1) in Fig. 15(b). The coefficient values K_1 and K_2 are equal to 0.73e-6 and 1.89e-7 respectively. The finite beam exhibits a purely converging shape along this axis.



(a) (b) (c) (d)

Fig. 14. Transversal intensity profiles with an enhanced contrast of a one-dimensional Layer beam propagating over a limited distance of: (a) 0.07 m, (b) 0.35 m, (c) 0.70 m and (d) 1.3 m. The size of the image is 14.57 mm x 12.6 mm.



(a) (b)

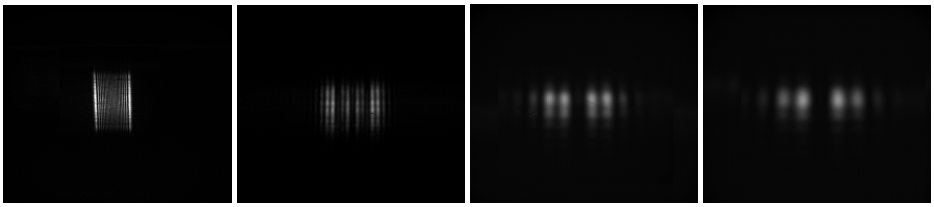
Fig. 15. (a) Generating wavefront measured using the Shack-Hartmann sensor for the finite Layer beam. (b) Line-profile of the generating wavefront with modeled wavefront according to Eq. (1).

The one-dimensional Layer beam propagating to infinity is depicted in Fig. 16. The distance L_{PL} was equal to 25.25 mm. The number of lines changes as the beam travels in the near zone (Figs. 16(a) and 16(b)). In the diverging zone, the pattern stabilizes, as can be seen for the distances of 4.1 and 5.3 m (Figs. 16(c) and 16(d)). The measured generating wavefront for the aforementioned beam can be seen in Fig. 17(a) and the line profile together with the modeled wavefront according to Eq. (1) in Fig. 17(b). The coefficient values K_1 and K_2 are equal to -0.63e-6 and 1.93e-7 respectively. The local minima in the line profile along the x-axis are evident, the beam propagates to infinity.

The value of K_1 for both one-dimensional beams is slightly outside the expected range obtained from simulations (Fig. 4). This discrepancy may be due to the physical difficulty of measuring the wavefront directly behind the projection lens, as there was a gap of several tens of millimeters between the projection lens surface and the Shack-Hartmann sensor. Alternatively, it could be due to spatial or wavefront differences between the Gaussian beam used in the simulations and the one in the measurements.

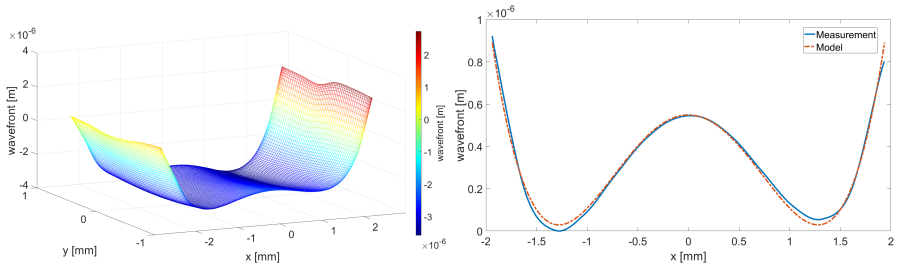
A two-dimensional Layer beam is depicted in Fig. 18. Similarly to the simulation, an additional phase lens with the same parameters was added, along with an extra projection lens with a focal

Optics EXPRESS



(a) (b) (c) (d)

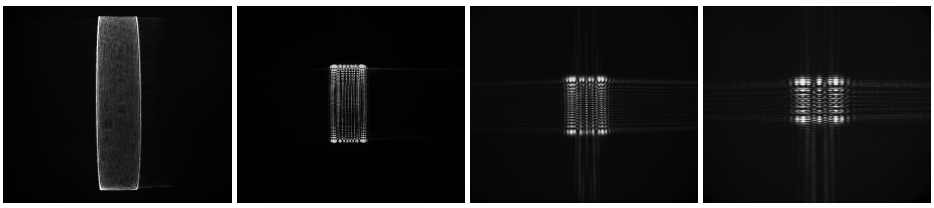
Fig. 16. Transversal intensity profiles with an enhanced contrast of a one-dimensional infinitely propagating Layer beam at: (a) 0.3 m, (b) 1.25 m, (c) 4.1 m, and (d) 5.3 m. The size of the image is 14.57 mm x 12.6 mm.



(a) (b)

Fig. 17. (a) Generating wavefront measured using the Shack-Hartmann sensor for the infinitely propagating Layer beam. (b) Line-profile of the generating wavefront with modeled wavefront according to Eq. (1).

length of 50 mm rotated 90 degrees around the optical axis (Fig. 3) with the distance L_{PL1} = 29 mm, and the distance L_{PL2} = 55.6 mm. At the distance of 0.15 m (Fig. 18(a)), noticeable field distortion occurs because the beam passes through an additional projection lens, which manifests itself as curved lines in the pattern. However, this effect diminishes as the beam travels further.

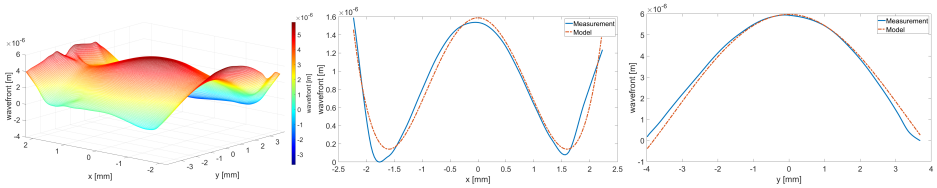


(a) (b) (c) (d)

Fig. 18. Transversal intensity profiles with an enhanced contrast of a two-dimensional Layer beam at: (a) 0.15 m, (b) 0.85 m, (c) 1.10 m and (d) 1.80 m. The size of the image is 14.57 mm x 12.6 mm.

The measured generating wavefront of the two-dimensional Layer beams is depicted in Fig. 19(a). The line profiles together with the modeled wavefront according to Eq. (1) with coefficients values K_1 = -1.14e-6 and K_2 = 2.23e-7 for the line-profile along the x-axis and K_1 = -5.34e-7 and K_2 = 8.43e-9 for the line-profile along the y-axis can be seen in Figs. 19(b) and 19(c) respectively. The distinctive sombrero shape of the line profile is observed along the x-axis while only the diverging part of the wavefront is visible along the y-axis.

Optics EXPRESS



(a) (b) (c)

Fig. 19. (a) Generating wavefront measured using the Shack-Hartmann sensor for the two-dimensional Layer beam. (b) Line-profile of the generating wavefront along the x-axis. (c) Line-profile of the generating wavefront along the y-axis with modeled wavefronts according to Eq. (1).

Generating the two-dimensional beams, using only a single optical element that can introduce a phase shift similar to the generating wavefront, or using a spatial light modulator would mitigate this distortion. Nevertheless, there will be a trade-off in the cost of the setup and the tunability of the beam parameters compared to the generation using cylindrical lenses. An alternative approach involves combining two orthogonal Layer beams using a beam splitter, however, this configuration imposes requirements on the precise alignment of the beams.

4. Discussion

In this study, pseudo-nondiffracting one-dimensional and two-dimensional Layer beams were successfully simulated and generated using various combinations of cylindrical lenses. The simulations confirmed that, depending on the generator parameters, a Layer beam can be tuned to propagate over finite or infinite distances based on the shape of the generating wavefront. The relationship between the generating wavefront shape and the beam's propagation characteristics was analyzed, revealing a connection to the propagation behavior of the two Airy-like beams that form the Layer beam.

Most of the simulations focused on the one-dimensional beam. For beams with finite propagation distances, the number of lines gradually decreased as the beam propagated, exhibiting pseudo-nondiffracting properties, such as regeneration behind obstacles throughout the entire propagation length. For beams propagating over infinite distances, the pattern stabilized after leaving the near zone and entering a so-called diverging zone. In this case, the infinitely propagating beam maintained a consistent transversal intensity distribution pattern that diverged further along the propagation path, losing its pseudo-nondiffracting properties. By adjusting the focal length of the projection lens, the beam's spatial dimensions can be tailored to a given distance.

The two-dimensional Layer beam, while demonstrating similar characteristics, showed initial shape distortions due to the additional projection lens. However, these distortions became negligible as the beam propagated further, indicating that initial aberrations introduced by optical elements can be mitigated with sufficient propagation distance. The ability to generate such beams with cylindrical lenses underscores the versatility and effectiveness of this approach while maintaining a low-cost, low-complexity setup.

The propagation characteristics of the Layer beams were confirmed through measurements. The generating wavefronts, measured using a Shack-Hartmann sensor, closely matched the simulated wavefronts. Discrepancies between measurements and simulations may have arisen due to spatial constraints that prevented direct wavefront measurement immediately behind the projection lens or differences between the Gaussian beams used in the simulations and those in the experiments.

Optics EXPRESS

Overall, this work demonstrates the feasibility of generating Layer beams using cylindrical lenses, providing a solid foundation for further exploration of these beams in various applications. Future research will focus on developing a system that utilizes Layer beams specifically for the alignment of accelerator components.

Funding. Technická Univerzita v Liberci (SGS-2024-3423); CERN.

Acknowledgments. The authors acknowledge the financial support provided by the Knowledge Transfer group at CERN through the KT Fund. Portions of this work were presented at the IPAC2024 conference, Optimization of Symmetrical Optical Caustic Beams for Long-Distance Alignment, and at the conference EUSPEN2024, Optimization of Symmetrical Layers of Optical Caustic Beams Generated Using Cylindrical Lenses. This work was partly supported by the Student Grant Scheme at the Technical University of Liberec through project SGS-2024-3423.

Disclosures. The authors declare no conflicts of interest.

Data availability. Data underlying the results presented in this paper are not publicly available at this time but may be obtained from the authors upon reasonable request.

References

1. Y. A. Kravtsov and Y. I. Orlov, *Caustics, Catastrophes and Wave Fields*, vol. 15 (Springer Science & Business Media, 2012).
2. J. F. Nye, *Natural Focusing and Fine Structure of Light: Caustics and Wave Dislocations* (CRC Press, 1999).
3. P. Vaveliuk, A. Lencina, J. A. Rodrigo, *et al.*, "Caustics, catastrophes, and symmetries in curved beams," Phys. Rev. A **92**(3), 033850 (2015).
4. G. A. Siviloglou and D. N. Christodoulides, "Accelerating finite energy airy beams," Opt. Lett. **32**(8), 979–981 (2007).
5. G. Siviloglou, J. Broky, A. Dogariu, *et al.*, "Observation of accelerating airy beams," Phys. Rev. Lett. **99**(21), 213901 (2007).
6. T. Vettenburg, H. I. Dalgarno, J. Nylk, *et al.*, "Light-sheet microscopy using an airy beam," Nat. Methods **11**(5), 541–544 (2014).
7. J. Baumgartl, M. Mazilu, and K. Dholakia, "Optically mediated particle clearing using airy wavepackets," Nat. Photonics **2**(11), 675–678 (2008).
8. P. Polynkin, M. Kolesik, J. V. Moloney, *et al.*, "Curved plasma channel generation using ultraintense airy beams," Science **324**(5924), 229–232 (2009).
9. N. K. Efremidis, Z. Chen, M. Segev, *et al.*, "Airy beams and accelerating waves: an overview of recent advances," Optica **6**(5), 686–701 (2019).
10. P. Vaveliuk, A. Lencina, J. A. Rodrigo, *et al.*, "Symmetric airy beams," Opt. Lett. **39**(8), 2370–2373 (2014).
11. P. Vaveliuk, A. Lencina, J. A. Rodrigo, *et al.*, "Intensity-symmetric airy beams," J. Opt. Soc. Am. A **32**(3), 443–446 (2015).
12. Y. Wu, J. Zhao, Z. Lin, *et al.*, "Symmetric pearcey gaussian beams," Opt. Lett. **46**(10), 2461–2464 (2021).
13. Q. Wei, J. Jiang, Z. Mo, *et al.*, "Symmetric swallowtail beams in the rectangle frame," Ann. Phys. **535**(3), 2200466 (2023).
14. J. Wang, J. Bu, M. Wang, *et al.*, "Generation of high quality airy beams with blazed micro-optical cubic phase plates," Appl. Opt. **50**(36), 6627–6631 (2011).
15. A. Benstiti, K. Ferria, and A. Bencheikh, "Generation of a variety of airy beams using a dynamic diffractive optical phase element," J. Opt. Soc. Am. B **37**(11), A45–A53 (2020).
16. B. Yalizay, B. Soylu, and S. Akturk, "Optical element for generation of accelerating airy beams," J. Opt. Soc. Am. A **27**(10), 2344–2346 (2010).
17. L. Begel and T. Galstian, "Dynamic generation of non-diffracting beams by using an electrically variable liquid crystal lens," Opt. Commun. **441**, 127–131 (2019).
18. J. Ma, Y. Li, Q. Yu, *et al.*, "Generation of high-quality tunable airy beams with an adaptive deformable mirror," Opt. Lett. **43**(15), 3634–3637 (2018).
19. B. Wu, B. Xu, X. Wang, *et al.*, "Generation of a polarization insensitive airy beam using an all-dielectric metasurface," Opt. Mater. Express **11**(3), 842–847 (2021).
20. B. Yu, J. Wen, L. Chen, *et al.*, "Polarization-independent highly efficient generation of airy optical beams with dielectric metasurfaces," Photonics Res. **8**(7), 1148–1154 (2020).
21. Z. Cai, Y. Liu, C. Zhang, *et al.*, "Continuous cubic phase microplates for generating high-quality airy beams with strong deflection," Opt. Lett. **42**(13), 2483–2486 (2017).
22. B.-Y. Wei, P. Chen, W. Hu, *et al.*, "Polarization-controllable airy beams generated via a photoaligned director-variant liquid crystal mask," Sci. Rep. **5**(1), 17484 (2015).
23. J. Zhou, Y. Liu, Y. Ke, *et al.*, "Generation of airy vortex and airy vector beams based on the modulation of dynamic and geometric phases," Opt. Lett. **40**(13), 3193–3196 (2015).
24. Z. Cao, C. Zhai, J. Li, *et al.*, "Light sheet based on one-dimensional airy beam generated by single cylindrical lens," Opt. Commun. **393**, 11–16 (2017).

Optics EXPRESS

25. D. Papazoglou, S. Suntsov, D. Abdollahpour, *et al.*, "Tunable intense airy beams and tailored femtosecond laser filaments," Phys. Rev. A **81**(6), 061807 (2010).
26. D. Abdollahpour, M. Lotfollahi, M. Yeganeh, *et al.*, "Generation and characterization of adjustable pure third-order spatial phase by tuning optical aberrations," J. Opt. **21**(8), 085602 (2019).
27. Z. Yang, M. Prokopas, J. Nylk, *et al.*, "A compact airy beam light sheet microscope with a tilted cylindrical lens," Biomed. Opt. Express **5**(10), 3434–3442 (2014).
28. W. Niewiem, K. Polak, M. Dusek, *et al.*, "Variation of structured laser beam pattern and optimization for an alignment reference line creation," Opt. Express **31**(26), 43307–43322 (2023).
29. M. Dusek, E. Roikova, D. Mergelkuhl, *et al.*, "Analysis of centroiding algorithms for non-diffracting structured and hollow structured laser beams," Appl. Opt. **63**(1), 263–274 (2024).
30. M. Dusek, J.-C. Gayde, and M. Sulc, "Wavefront reconstruction of a non-diffracting structured laser beam," Opt. Express **31**(25), 42099–42110 (2023).
31. K. Polak, M. Sulc, and J.-C. Gayde, "Structured laser beam in non-homogeneous environment," in *15th International Workshop on Accelerator Alignment* (2022).
32. K. Polak, J. Gayde, S. M. Sulc, *et al.*, "3D Polarisation of a Structured Laser Beam and Prospects for its Application to Charged Particle Acceleration," in *14th International Particle Accelerator Conference* (2023), pp. 1444–1445.
33. H. M. Durand, S. Bartolome-Jimenez, T. Dijoud, *et al.*, "HL-LHC Alignment Requirements and Associated Solutions," in *Proc. IPAC* (JACoW Publishing, 2017), pp. 1893–1896.
34. J. Gayde and M. Sulc, "An optical system for producing a structured beam," EP3564734 (2019).
35. J. W. Goodman, *Introduction to Fourier Optics* (Roberts and Company Publishers, 2005).
36. J. Durmin, "Exact solutions for nondiffracting beams," J. Opt. Soc. Am. A **4**(4), 651–654 (1987).
37. M. Born and E. Wolf, *Principles of Optics: Electromagnetic Theory of Propagation, Interference and Diffraction of Light* (Elsevier, 2013).
38. M. Dusek, "Advanced calibration and characterization of a Shack-Hartmann sensor," Master's thesis, Technical University of Liberec (2021).
39. W. H. Southwell, "Wave-front estimation from wave-front slope measurements," J. Opt. Soc. Am. **70**(8), 998–1006 (1980).

5.183.15.154 (8. 2025-01-30 14:17:17)

7.6 First Steps Toward the Development of a Straight-Line Reference Alignment System for Future Accelerators at CERN Using Pseudo-Nondiffracting Layer Beams

This paper presents the first experimental evaluation of a straight-line reference alignment system based on LBs, specifically developed for application in particle accelerator environments. The study introduces custom-designed hollow sensors, each equipped with four linear CMOS chips and a square aperture, enabling simultaneous multi-point measurements along the beam path without obstructing the optical reference. The hollow sensors were fiducialized using CMMs. Experimental results are compared against laser tracker measurements. Additionally, a proof-of-concept for a radiation-hard sensor employing an optical fiber matrix is demonstrated. The paper was published in Measurement Science and Technology (Q2, Impact Factor = 2.7). Note that the first conceptual ideas for LB-based alignment systems were presented in the proceedings of the International Workshop on Accelerator Alignment held in San Francisco, California, USA (IWAA2024): "Layer beams and their prospect for long-range alignment" [63].

Measurement Science
and Technology

100 year anniversary
Measurement Science and Technology

PURPOSE-LED
PUBLISHING™

PAPER • **OPEN ACCESS**

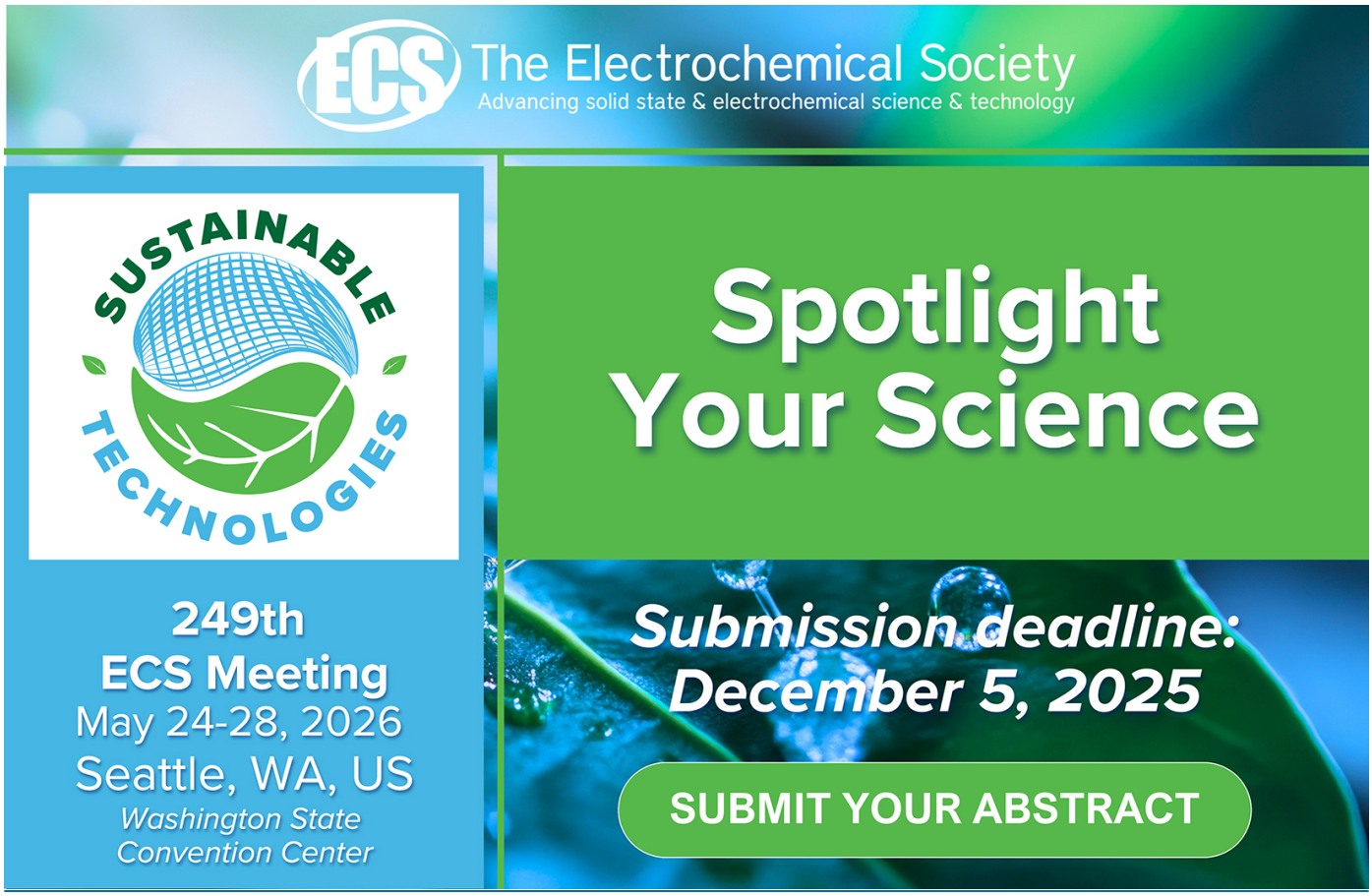
First steps toward the development of a straight-line reference alignment system for future accelerators at CERN using pseudo-nondiffracting Layer beams

To cite this article: Martin Dušek *et al* 2025 *Meas. Sci. Technol.* **36** 105009

View the article online for updates and enhancements.

You may also like

- Non-invasive, non-contact conductivity measurement using radiofrequency probe loading
Tashi Wangchuk, Andrés Ramírez Aguilera and Bruce J Balcom
- ADMA-YOLO: a lightweight strip steel surface defect detection network via adaptive dual-path and multi-branch aggregation
Liangbin Li, Shaolin Hu, Yandong Hou et al.
- Multimodal data fusion-driven fault diagnosis of aero-engine bearings using a pseudo-Siamese neural network
Guoxin Wu, Yuanqiu Dong, Xuanyu Chen et al.



This content was downloaded from IP address 46.135.79.87 on 16/10/2025 at 17:49

OPEN ACCESS
IOP Publishing
Measurement Science and Technology
Meas. Sci. Technol. **36** (2025) 105009 (13pp)
https://doi.org/10.1088/1361-6501/ae0ba0

First steps toward the development of a straight-line reference alignment system for future accelerators at CERN using pseudo-nondiffracting Layer beams

Martin Dušek[1,2,*], Sebastian Figura[1,3], Jakub Michal Polak[1], Solomon William Kamugasa[1], Dirk Mergelkuhl[1], Witold Niewiem[1,5], Štěpán Kunc[2], Jean-Christophe Gayde[1] and Miroslav Šulc[2,4]

[1] The European Organization for Nuclear Research (CERN), 1211 Geneva, Switzerland
[2] Technical University of Liberec (TUL), Studentská 1402/2, 461 17 Liberec, Czech Republic
[3] Cracow University of Technology (CUT), ul. Warszawska 24, 31-155 Kraków, Cracow, Poland
[4] Institute of Plasma Physics of the Czech Academy of Sciences (IPP CAS), U Slovanky 2525, 182 00 Prague, Czech Republic
[5] Eidgenössische Technische Hochschule Zürich (ETHZ), Rämistrasse 101, 8092 Zurich, Switzerland

E-mail: martin.dusek@cern.ch

Received 28 April 2025, revised 9 September 2025
Accepted for publication 25 September 2025
Published 13 October 2025

Abstract

This paper presents experimental results that allow for the performance evaluation of a straight-line reference alignment system based on pseudo-nondiffracting Layer beams (LBs). Sensors, developed specifically for this system, feature four linear CMOS chips and a square aperture. This allows for simultaneous measurements along the beam path without disrupting the laser reference. Measurements, conducted over a distance of 2 m from the first to the last sensor, were compared with state-of-the-art alignment techniques to assess the system performance. The alignment reference generated by the LBs exhibited a repeatability and reproducibility root-mean-square error (RMSE) of less than 30 µm. The relative alignment precision for a known displacement was validated with a standard deviation of 4.3 µm. The results demonstrate the potential for scaling the system to longer distances. The key sources of noise that must be addressed before such scaling can be realized are identified. Additionally, a proof-of-concept for future development of a radiation-hard sensor utilizing optical fiber matrices is demonstrated. The RMSE of the reference position detection introduced by the fiber matrix remained below 1.3 µm. This would allow the sensor to be used reliably in high-radiation environments typical for accelerator facilities. This study serves as a foundational step toward developing a straight-line reference alignment system based on pseudo-nondiffracting LBs intended for deployment in the accelerator facilities.

* Author to whom any correspondence should be addressed.

Original Content from this work may be used under the terms of the Creative Commons Attribution 4.0 licence. Any further distribution of this work must maintain attribution to the author(s) and the title of the work, journal citation and DOI.

© 2025 The Author(s). Published by IOP Publishing Ltd

Supplementary material for this article is available online

Keywords: accelerator subsystems and technologies, alignment technologies, straight-line reference, nondiffracting beams, caustic beams, Layer beams

1. Introduction

1.1. Straight-line alignment systems

Achieving precise geometric configurations of particle accelerator components is crucial for the optimal functioning of such complex machines. This process is known as alignment. Various measurement techniques, including polar measurements using laser trackers or leveling methods, are used to accurately determine the position of accelerator components [1–3].

So-called straight-line reference alignment systems are supplementary to the aforementioned methods and involve measuring offsets of individually aligned elements from a reference line. The key components of these systems include the alignment reference itself, reference points on the aligned objects, and sensors that measure offsets from the reference line. The requirement of modern accelerators on the straight-line reference system is to provide alignment accuracy and repeatability in the order of micrometers within a length of a sliding window that is in the order of hundreds of meters long [1, 4].

Wire positioning system (WPS) and hydrostatic leveling system (HLS) are used in alignment monitoring in accelerator facilities around the world (Fermilab [5, 6], SLAC [7]). At Conseil européen pour la recherche nucléaire (CERN), the straight-line alignment reference is given by the WPS's conductive wire. This gives the possibility to measure a vertical and horizontal offset from this reference using capacitive or optical sensors [8]. The vertical coordinate measurement, using capacitive or optical HLS sensors, is complementary and is used to calculate the catenary of the wire and link measurements to a geoid (local reference given by a gravitation field) [2, 9]. These systems can reach an accuracy of 5 µm in the local coordinate system [8]. The WPS is susceptible to environmental perturbations such as humidity, which requires correction by the HLS. The wire is fragile and prone to breaking under its own weight. These factors limit the length of the sliding window. To overcome this, the utilization of multiple overlapping reference lines can be used, however, this can limit the accuracy of the alignment procedure.

1.2. Optical-based straight-line reference systems

Optical-based straight-line reference systems are a viable alternative that could provide a straight-line reference over a longer distance than the WPS and HLS. Various optical references have been explored in other publications, including a Fresnel zone plate [10–12], Poisson spot [13–15], Airy pattern [16–18], and Gaussian beam [19, 20].

The optical-based methods typically suffer from the non-homogeneous refractive index of the propagation medium, which causes the beam trajectory (the alignment reference) to be non-straight. To meet the accuracy requirements, vacuum pipes are used to mitigate this effect [10, 17]. An additional limitation is beam divergence. For example, in the case of the Gaussian beam, the divergence causes a loss of contrast in the transversal laser profile imaged on a camera chip. This makes the accurate measurement of the straight-line reference challenging as the dynamic range of the signal decreases. Structured laser beams (SLBs) [21], characterized by pseudo-nondiffracting behavior similar to that of Bessel beams, have shown promise due to their low divergence and sharply defined inner core, which allows for accurate detection of the reference even after propagating for hundreds of meters. The main advantage, contrary to Bessel beams [22], is their theoretically infinite propagation distance [4].

Nevertheless, there are practical challenges when using SLB in a simultaneous multi-point straight-line reference system. The CMOS or CCD chip, which detects the position of the reference, obstructs the beam and prevents it from propagating further. This means that a system with mechanical moving shutters must be employed to move the chip in and out of the beam path. This can increase the cost and maintenance needs of the system. It also increases the time needed for the measurement. If the alignment reference is unstable during the measurement, the accuracy will be affected. This can be caused by an instability in the position of the SLB generator or due to a non-homogeneous distribution of the refractive index of the propagation medium. Both of these effects would lead to a change in the beam trajectory.

Pellicle beam splitters can be used to mitigate this problem. However, the non-parallelism of the beam splitter surfaces can cause significant angular deviation of the beam over distances of hundreds of meters [23]. This effect can spoil the straightness and quality of the reference line and necessitates careful calibration.

Layer beams (LBs) offer a promising alternative to overcome the limitation of simultaneous multi-point measurements. LBs are pseudo-nondiffracting optical beams generated using cylindrical lenses [24]. Unlike rotationally symmetric SLBs, LBs exhibit reflectional symmetry and produce parallel intensity lines. This allows for simultaneous multi-point measurements without fully obstructing the beam path. This capability significantly improves measurement efficiency and accuracy by enabling simultaneous detection of multiple points

along the beam path. The structured pattern of LBs allows for accurate detection of the reference even after propagating for hundreds of meters. The principle of the alignment system based on LBs will be described in greater detail in the following text.

1.3. Contribution of the study

This paper presents experimental results obtained from an LBs-based alignment system using specifically developed hollow sensors. The experiments evaluate the system performance over a relatively short distance of 2 m by comparing it to state-of-the-art alignment techniques. The paper aims to confirm that the system operates reliably over this distance, providing a necessary foundation for future scaling to the longer distances required by LBs-based straight-line reference systems in accelerator facilities. This study also aims to identify key problems that must be addressed prior to extending the system's operational range to hundreds of meters.

Furthermore, recognizing the harsh radiation environment typical for accelerator tunnels, a proof-of-concept for radiation-hard sensors is presented utilizing optical fiber matrices for signal transmission away from radiation zones. This innovation would ensure the long-term reliability of sensor electronics by protecting them from radiation-induced damage.

The presented work serves as an essential step toward developing a robust long-distance alignment system, intended for deployment in the accelerator facilities at CERN.

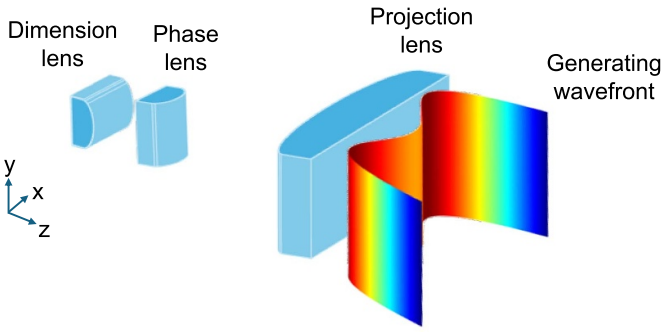


Figure 1. LB generator consisting of a dimension, phase, and projection lens with an illustration of a generating wavefront that dictates the caustic properties of the beam.

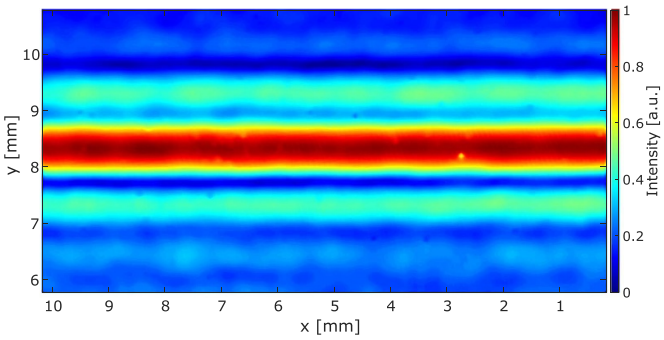


Figure 2. Horizontal LB imaged on a camera at the position of the first sensor - 1.7 m away from the generator. Diffraction patterns caused by dust on the CMOS chip were removed in post-processing.

2. Methodology

2.1. Layer beams

LBs belong to the family of so-called pseudo-nondiffracting optical beams. They are formed by the superposition of layers of two symmetrical Airy-like beams [25–28] propagating with opposing transversal acceleration directions. This results in a structured transversal intensity profile consisting of parallel lines. The structured pattern of the transversal intensity distribution and low divergence facilitates the accurate detection of the alignment reference even after propagation over a distance of 140 m [29].

The generator of the LBs used in this study consists of a dimensional, phase, and projection lens. This specific combination of lenses results in the creation of a so-called generating wavefront, which in turn leads to the formation of a caustic beam [30–34] that is responsible for the pseudo-nondiffracting properties of the beam as illustrated in figure 1. The dimension lens is rotated 90 degrees with respect to the other two around the optical axis, resulting in an elongation of the lines in the transversal intensity distribution caused by an increased divergence along the *y*-axis. The longitudinal propagation of the beam can be described by a so-called near zone and a diverging zone. In the near zone, the number of lines in the transversal intensity distribution changes with distance due to multiple overlapping and interfering contributions from different parts of the wavefront. In the diverging zone, the beam transversal pattern does not change with distance and only diverges. More about the generation principle and properties of the LBs can be found in our previous work [24].

The generator of the LBs used for experiments in this study was optimized for propagation over 3.7 m. It consisted of the dimension lens with a focal length of 50 mm, and of a phase lens and projection lens, both with a focal length of 10 mm. The lenses were made of NBK-7 glass. The distance between the phase and projection lenses was optimized so that the transversal intensity distribution in the diverging zone of the beam consisted of a single line with small side lobes as seen in figure 2.The input laser diode with a wavelength of 532 nm and a power output of 0.9 mW was used as a light source.

2.2. Layer beam-based alignment system

The LBs-based alignment reference relies on a reference plane rather than a reference line. This plane is generated leveraging the reflection symmetry of the transversal intensity distribution along the path of the LB, as illustrated in figure 3.

In the proposed alignment system, two LBs from independent generators, one of which was rotated around the optical axis with an angle close to 90 degrees, were combined using

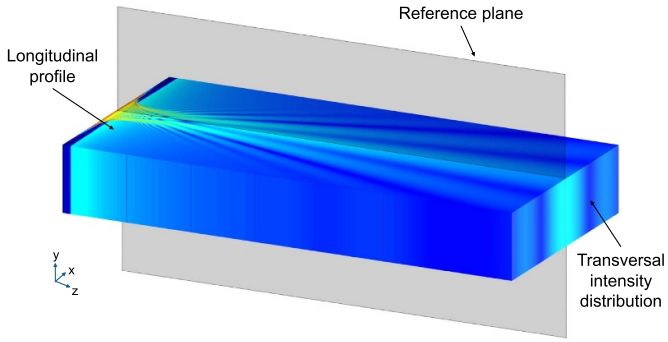


Figure 3. Illustration of an alignment reference plane created by an LB.

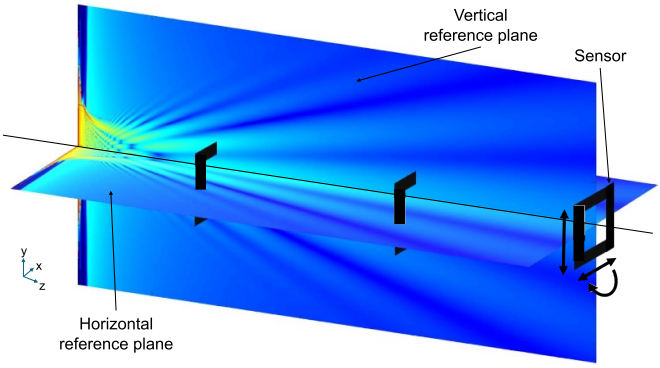


Figure 4. Illustration of an alignment system based on LBs.

a pellicle beam splitter. This approach simultaneously generates two reference planes, creating a cross pattern in the transversal intensity distribution, while their intersection creates the reference line. The detection is done using a hollow sensor, which consists of four linear image sensors and an aperture. The sensor intercepts only a small portion of the beam cross-section, allowing most of it to propagate further thanks to the aperture. This ensures, together with the divergence of the beam, that the signal can be detected on multiple measurement points along the optical axis at one point in time.

Two points per reference plane are detected at each hollow sensor. A minimum of two sensors is needed to define the reference plane, as by definition, the plane needs to be established using a minimum of three points in space. In the alignment configuration, the first and the last sensors define the reference planes, and the positions of sensors in between them are measured with respect to this reference. Translational misalignment in both horizontal and vertical directions can be measured. Additionally, a rotational misalignment around the beam propagation axis (the roll) can also be determined as illustrated in figure 4. This is an advantage compared to the state-of-the-art straight-line alignment systems that can usually measure only in the translational directions.

Hollow sensors consisting of four linear CMOS chips placed around a square aperture were developed for the experiment (figure 5). Hamamatsu S11639-01 CMOS chips with a quartz cover window and a protective film on the pixels

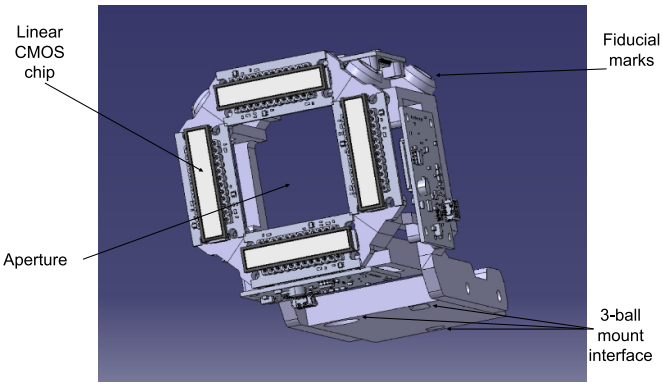


Figure 5. CAD model of the hollow sensor developed for the detection of LBs. A photo of the sensor can be found in the supplementary materials.

were used [35]. The sensor mount was 3D printed using stainless steel to minimize thermal expansion effects and increase mechanical stability compared to the materials used for plastic 3D printing. The coefficient of thermal expansion of the stainless steel can be 4–10 times lower, depending on the chosen plastic [36, 37]. The mount was equipped with laser tracker fiducial (reference) marks. A fiducialization is a process that links the reference geometry of the sensor to the fiducial marks [1]. Each sensor was placed on a three-ball kinematic mount [38].

A so-called symmetry-breaking effect refers to a non-straight alignment reference given by the laser beam caused by the diffraction effects on the aperture [39]. The aperture size of 75 mm was used for the first and second sensors. The last sensor had an aperture size of 40 mm. In the future, the sensors are intended for use on a 140 m long testing bench. The aperture sizes were chosen to minimize the symmetry-breaking effects over the 140 m while keeping the beam visible on all the sensors. Note that these effects are negligible on the setup presented in this study, as the distance is significantly shorter.

To experimentally validate the performance of the developed sensors, a dedicated measurement setup was established. Three sensors were arranged sequentially along the beam propagation path as illustrated in figure 6. The first one was positioned at a distance of 1.7 m from the LB generators. The spacing between the sensors was equal to 1 m, resulting in a total length of 3.7 m from the generator to the last sensor. To mitigate issues arising from beam propagation through a non-homogeneous medium, a non-reflecting black pipe was placed between the sensors. This minimized the refractive index fluctuation caused by the mixing of the air in the laboratory. In the future, we plan to propagate the LBs inside a vacuum pipe to minimize the disturbance caused by the non-homogeneous refractive index of the propagation medium.

2.3. Fiducialization

Before installation in the experimental setup, each sensor underwent a metrological characterization in a dedicated

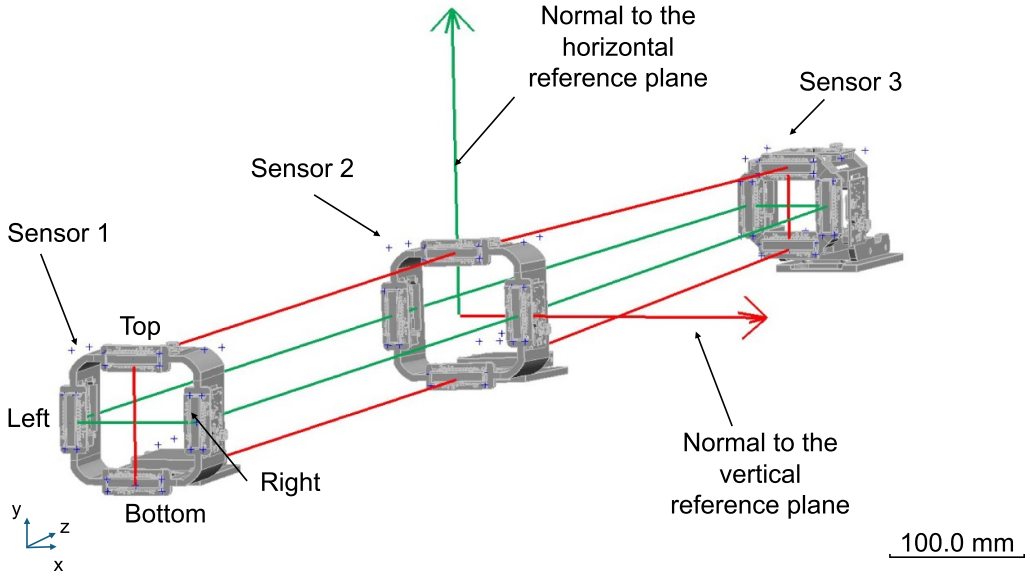


Figure 6. Layout of the experiment. Two LBs generate the horizontal and vertical reference planes based on the readings from the CMOS chips. A photo of the experimental setup can be found in the supplementary materials.

laboratory. The positions of the active parts of the CMOS chips, fiducial marks, and three-ball mount interface within a sensor's reference frame were precisely determined in the local Cartesian coordinate system. This characterization was done utilizing coordinate-measuring machines (CMM) [40]. Touch and optical probes were used, resulting in a measurement uncertainty of 2.5 µm. These measurements provided accurate coordinates of the pixel positions relative to the fiducial targets and to the standardized three-ball mount interface, ensuring the common local coordinate frame within each sensor.

After placing the sensors in the experimental setup, a total of 24 fiducial marks (8 on each sensor) were measured using a Leica AT401 laser tracker from three instrument stations. The measurements were linked using the unified spatial metrology network (USMN) module within the commercially available Spatial Analyzer metrological software. This allowed for the integration of all observations into a single measurement network. The network achieved an overall root-mean-square error (RMSE) of 0.004 mm, with a maximum point residual of 0.015 mm.

To relate the local sensor coordinate systems to the global coordinate system obtained from the laser tracker measurement, best-fit transformations were performed between the fiducial marks measured by the CMM and the laser tracker. This allowed us to determine the absolute position of all the active parts of the CMOS chips, fiducial marks, and three-ball mount interfaces within a common global coordinate system. The results are summarized in the table 1. The values of the RMSE for all the fits were under 0.013 mm with a largest point residual value equal to 0.017 mm. The global Cartesian coordinate system was chosen to be the same as the one used by the first laser tracker station, and the results presented are within this coordinate system.

Table 1. Best-fit transformation results between each sensor's local coordinate system and the global USMN frame.

Metric	Sensor 1 (mm)	Sensor 2 (mm)	Sensor 3 (mm)
RMSE	0.009	0.012	0.006
Maximum residual	0.011	0.017	0.008

2.4. Characterization of the alignment system

Ideally, the LB should create a perfect reference plane, ensuring that all 6 points measured on all 3 sensors lie precisely on this plane. In reality, measurement uncertainty from the ideal plane arises due to various factors such as the dark noise of the CMOS chips, atmospheric disturbances, and interference on both the CMOS cover glass and the protective film of the pixels. Assessing the quality of this reference plane is essential because it directly impacts the precision of alignment measurements.

Once the LB is incident on the sensors, the signal on each CMOS chip was analyzed using a weighted center of gravity algorithm (first moment weighted by intensity) with gamma correction [29, 41]. This allowed for a calculation of a centroid coordinate with a sub-pixel resolution. The gamma correction was applied to the intensity vector $I(x)$ before calculating the centroid coordinate:

$$G_{\mathrm{corr}}(x) = I_{\max}\left(\frac{I(x)}{I_{\max}}\right)^{\gamma} \tag{1}$$

where $I_{\max}$ is the maximum intensity value. The value of $\gamma = 8$ was used. The centroid coordinate $\bar{x}$ of the intensity vector was then calculated using the center of gravity algorithm as:

$$\bar{x} = \frac{\sum_{x=0}^{x_{\max}} G_{\mathrm{corr}}(x)\, x}{\sum_{x=0}^{x_{\max}} G_{\mathrm{corr}}(x)}. \tag{2}$$

This approach gave the absolute position of 6 points in the global coordinate system for both horizontal and vertical directions. A plane was fitted among these 6 points, and the error of the fit was analyzed. Several experiments were conducted on the performance of the system:

2.4.1. Temporal repeatability. The temporal repeatability of the quality of the alignment reference generated by the LBs was measured by performing twenty consecutive measurements for each plane spaced by one-second intervals, without altering any system parameters.

An offset for each point from the ideal fitted plane was calculated. The RMSE was determined from these offsets. This resulted in twenty values of the RMSE, one for each measurement. The mean value of the twenty RMSEs was calculated with a confidence interval of 2-sigma. Additionally, a maximum offset value of the point from the ideal reference plane was identified to illustrate the largest deviation. The same metrics for error evaluation were employed to analyze the results in the following sections 2.4.2 and 2.4.3.

2.4.2. Repeatability for different reference planes. A high-quality parallel optical window was introduced into the beam path and rotated between each of the twenty measurements, while the sensors were not moved. A single rotation induced a controlled lateral shift of 50 µm in the reference plane position. This allowed us to assess whether the quality of the alignment reference remained consistent for different reference plane positions.

Twenty measurements were taken for each position of the plane. The measurements were not taken simultaneously for both reference planes because the glass plate had to be rotated by 90 degrees around the optical axis between the measurements to shift the position of either the vertical or horizontal plane. It was ensured that the angle was not significantly changed with respect to the cover glass of the CMOS chips.

2.4.3. Reproducibility. An additional experiment was conducted to evaluate the robustness of the alignment system under different sensor orientations and reproducibility. The sensors were rotated by 90 degrees around the z-axis. This rotation effectively swapped the CMOS chips in detecting horizontal and vertical reference planes. The absolute sensor positions were remeasured using a Leica AT403 laser tracker with similar measurement errors of the USMN and of the best fit as presented in the section 2.3. Again, as in the case of the temporal repeatability experiment in the section 2.4.1, twenty consecutive measurements were spaced by one-second intervals without altering any parameters. This measurement was conducted several days after the aforementioned experiment.

2.4.4. Relative alignment. Finally, the relative alignment capabilities of the system were tested. The reference plane was defined based on the known positions of the first and last sensors (Sensors 1 and 3) obtained by the laser tracker measurement. The middle sensor (Sensor 2) was mounted on a motorized linear stage and displaced repeatedly by precisely 0.050 µm increments, twenty times in the horizontal direction. Each displacement of the middle sensor was measured relative to the reference planes defined by the points measured on the first and the last sensors. This allowed us to perform an analysis of the relative linear misalignment of the middle sensor with respect to the alignment reference given by the LBs. The mean detected displacement was calculated within a 2-sigma confidence interval, together with a standard deviation, and minimum and maximum detected misalignment.

This measurement aimed to simulate the foreseen LBs-based alignment system, where reference planes will be defined by the first and last sensors. The sensors in between will be aligned relative to these reference planes. Note that the orientation of the sensors was the same as in the experiments described in sections 2.4.1 and 2.4.2.

2.5. Radiation hard sensor

Electronic components like CMOS chips are susceptible to radiation damage when used in accelerator environments. To address this, we propose using a fiber matrix system to transmit the signal away from the radiation zone. This would protect the electronic components as they can be shielded away from the radiation. However, a key consideration is how the fiber matrix affects image quality and signal intensity, which can impact the detection accuracy of the reference plane.

A fiber matrix made by Schott, measuring 1050 mm in length, was used in this experiment. The shape of the matrix is round with a diameter of 3.175 mm. It consists of a matrix of individual fibers, each with a diameter of 12 µm. A LB was propagated over 8 m and then split by a beam splitter. A generator with a projection lens focal length of 100 mm was used for this experiment. On one side of the beam splitter, a camera, Basler a2A5328-15umPRO, was placed without any imaging optics. This camera features a CMOS chip with a resolution of 5328×4608 pixels and a pixel size of 2.74×2.74 µm. On the other side of the beam splitter, a fiber matrix was put with the same camera type behind it. The end of the fiber matrix was positioned close to the CMOS chip, and the signal from the matrix was incident directly on it. The experimental layout is illustrated in figure 7.

Two equally sized images (400×800 pixels) were extracted from the transversal intensity distribution captured directly by the CMOS chip (figures 7(b) and (c)). These images were compared using the peak signal-to-noise ratio (PSNR) method [42]. Since both images originated from the same intensity distribution, the PSNR value was relatively high, providing a baseline for quality assessment.

As a next step, an image from the camera placed behind the fiber matrix containing the LB signal (figure 7(d)), was

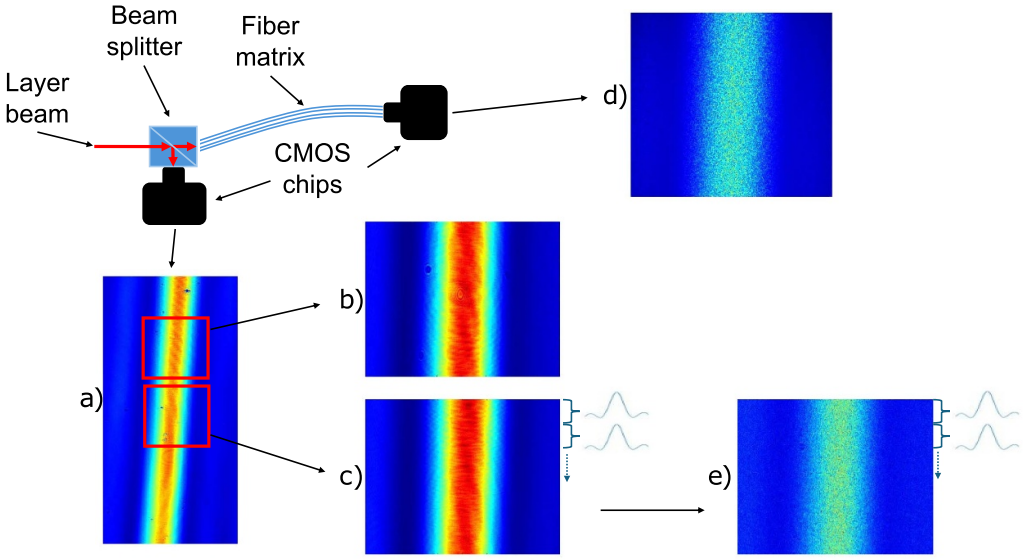


Figure 7. Top view of the measurement setup for the analysis of the influence of the optical fiber matrix on the signal. (a) Transversal intensity distribution seen on the CMOS without fiber matrix, (b) extracted images for PSNR baseline comparison, (c) extracted image for LB signal analysis, (d) Transversal intensity distribution after propagating through the fiber matrix, (e) [Image (c)] with induced noise for LB signal analysis.

compared to the image captured directly by the CMOS chip (figure 7(c)) using the PSNR. Since both images contain signals from the same LB, this comparison aimed to quantify the image quality and noise introduced by the transmission through the fiber matrix.

To simulate the insertion of the fiber matrix, the noise, which would result in the same PSNR value as after the transmission through the fiber matrix, was induced in the image detected directly behind the beam splitter (figures 7(c) and (e)). The corresponding standard deviation of the Gaussian was calculated using the formula using the PSNR value:

$$\sigma = \sqrt{\frac{I_{\max}^2}{10^{\frac{\mathrm{PSNR}}{10}}}} \tag{3}$$

where $I_{\max}$ is the maximum pixel intensity of the normalized grayscale image. A zero-mean Gaussian noise $N(0, \sigma^2)$ was introduced into the image. A scaling function was used to enhance the noise presence in bright regions. The dynamic range of the image was scaled. This allowed us to simulate an image (figure 7(e)) that would match the noise present in the image captured after propagating through the fiber matrix (figure 7(d)).

As illustrated in figures 7(c) and (e), from both the noise-induced and original image, twenty rows were summed up along the y-axis to simulate a larger pixel size of 27.2 µm. This was done to increase the signal-to-noise ratio and to simulate a linear CMOS chip with non-square pixels. This process was repeated and resulted in twenty signals of the LB from each image that were processed using the equation in equation (2). The differences in the coordinates between twenty signals from both images were compared using the RMSE with a 2-sigma confidence interval and maximum detected error.

3. Results

3.1. Layer beam-based alignment system

Several noise-induced effects were observed while conducting the experiments. If the LB direction of propagation was not perpendicular to the glass cover window of the CMOS chip, the signal was strongly distorted or asymmetrical.

The example of signals visible on each of the CMOS chips of every sensor can be seen in figure 8, while the asymmetric or noisy signals are indicated with red arrows. The signal on the CMOS of Sensor 3 – Right serves as an example of a symmetrical signal for reliable alignment reference detection using methods such as threshold-corrected center of gravity. In this case, the central lobe of the signal maintains its symmetry, which facilitates accurate analysis, even though the side lobes themselves may not be perfectly symmetrical. Applying a threshold effectively excludes the side lobes from the evaluation, allowing the algorithm to analyze the undistorted central portion of the signal. In contrast, the signal on the CMOS of Sensor 3 – Left displays a high-frequency noise, while the CMOS of Sensor 2 – Right exhibits a central lobe that is distinctly asymmetrical. Both cases can reduce the accuracy of reference position detection, as both types of noise in the signal can shift the calculated alignment reference away from its true position.

A time instability of the signal at each CMOS chip was evident. To characterize this behavior, the temporal stability of the detected centroid points, obtained from the signal on each individual CMOS chip, was assessed by performing twenty measurements spaced one second apart. The results, summarized in table 2, were analyzed using a standard deviation and

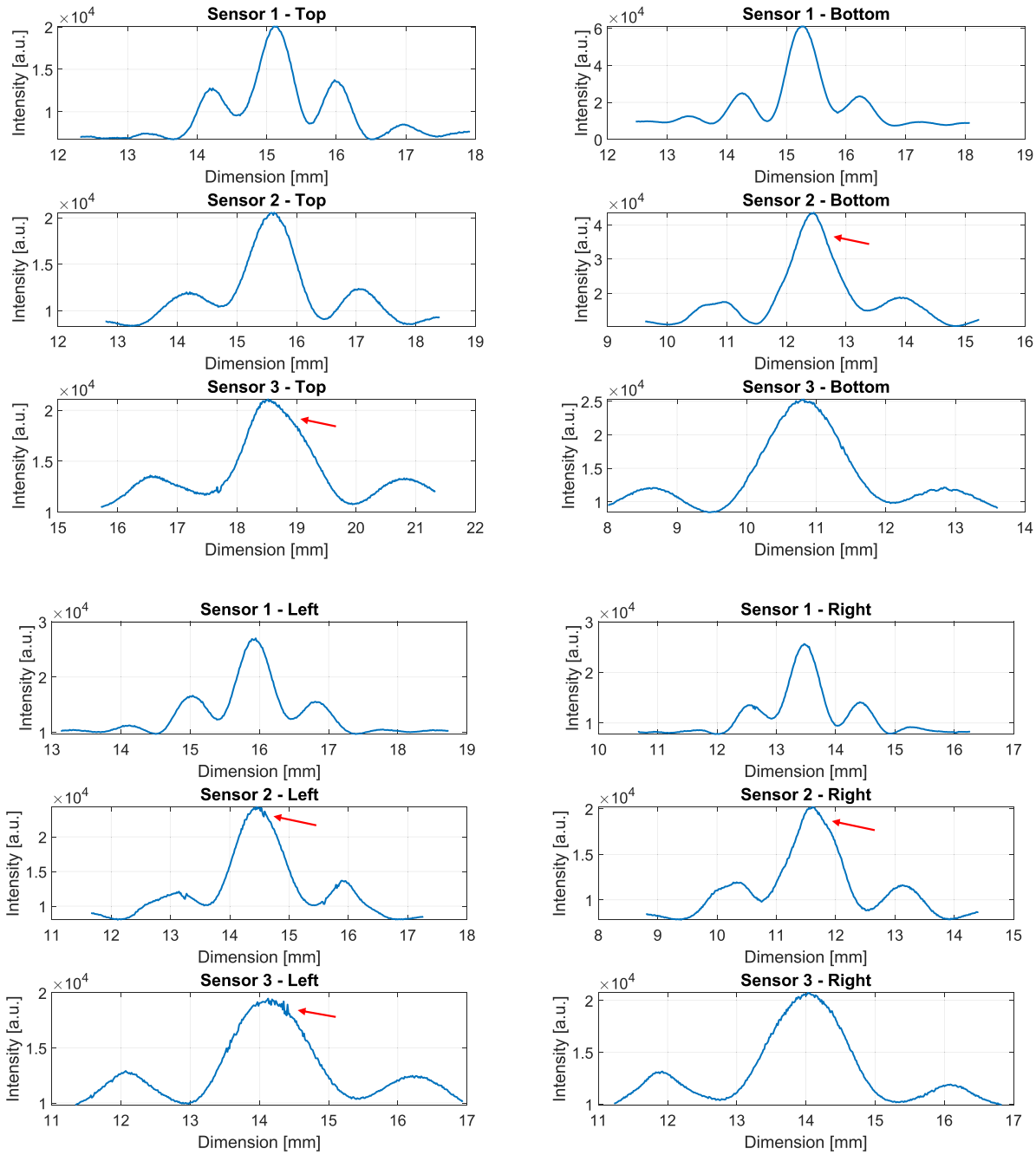


Figure 8. Signals visible on each CMOS chip. Red arrows are pointing at the regions of the signal significantly disturbed by noise.

minimum-maximum difference of the detected positions. The results indicate that the fluctuations are the lowest for Sensor 1, increase for Sensor 2, and are the highest for Sensor 3.

Measures, such as increased exposure time, background removal, and careful alignment of the reference plane with respect to the CMOS cover glass, were employed. However, none of these effects could be completely eliminated during measurement, necessitating post-processing of the signal using low-pass filtering.

3.1.1. Temporal repeatability. The results of the temporal stability experiment, presented in table 3, indicate a higher variability in the horizontal plane compared to the vertical plane. Specifically, the horizontal plane exhibited a mean RMSE of 0.025 ± 0.002 mm, while the vertical plane had a lower value of 0.017 ± 0.002 mm. The maximum offset value was also larger for the horizontal plane (0.050 mm) than for the vertical plane (0.045 mm).

3.1.2. Repeatability for shifted reference planes. The results of the repeatability analysis for different reference planes are presented in table 4. A higher variability in the horizontal plane compared to the vertical plane can be observed again. The values of the RMSE have increased compared to the

Table 2. Results of temporal repeatability of the centroid point position obtained from the LB signal at each CMOS chip.

	Sensor 1 (mm)	Sensor 2 (mm)	Sensor 3 (mm)
Top CMOS chip			
Standard deviation	0.0005	0.0020	0.0049
Min–Max	0.0020	0.0067	0.0149
Bottom CMOS chip			
Standard deviation	0.0004	0.0015	0.0038
Min–Max	0.0018	0.0054	0.0135
Left CMOS chip			
Standard deviation	0.0004	0.0012	0.0042
Min–Max	0.0019	0.0049	0.0143
Right CMOS chip			
Standard deviation	0.0005	0.0021	0.0033
Min–Max	0.0020	0.0070	0.0131

Table 3. Results of temporal repeatability.

Metric	Vertical plane (mm)	Horizontal plane (mm)
Mean RMSE	0.017 ± 0.002	0.025 ± 0.002
Mean RMSE interval	[0.008, 0.025]	[0.019, 0.029]
Maximum point offset	0.045	0.050

Table 4. Results of repeatability analysis for shifted reference planes.

Metric	Vertical plane (mm)	Horizontal plane (mm)
Mean RMSE	0.02 ± 0.002	0.027 ± 0.002
Mean RMSE interval	[0.016, 0.026]	[0.019, 0.030]
Maximum point offset	0.044	0.052

Table 5. Results of temporal repeatability for 90 degrees rotated sensors.

Metric	Vertical plane (mm)	Horizontal plane (mm)
Mean RMSE	0.024 ± 0.002	0.020 ± 0.002
Mean RMSE interval	[0.020, 0.026]	[0.016, 0.026]
Maximum point offset	0.048	0.043

temporal stability by 0.004 mm and 0.002 mm for the vertical and horizontal planes, respectively.

3.1.3. Reproducibility. The results of the temporal stability experiment after rotating the sensors by 90 degrees are presented in table 5. Compared to the aforementioned temporal stability measurement, a shift in variability between the horizontal and vertical planes can be observed. The mean RMS for the vertical plane increased to 0.024 ± 0.002 mm, while the value for the horizontal plane decreased to 0.020 ± 0.002 mm.

3.1.4. Relative alignment. The results of the relative alignment capability tests, presented in table 6, indicate that the mean detected displacement closely matched the known increment of 0.050 mm induced by the motorized linear stage. A mean value of 0.051 ± 0.002 resulting from the twenty measurements was detected. The relatively high standard deviation of 0.004 mm with the maximum and minimum detected misalignment of 0.056 mm and 0.042 mm respectively, suggests notable variability between the measurements.

Table 6. Results of the relative misalignment of the Sensor 2 for the known displacement of 50 µm.

Metric	Value (mm)
Mean detected displacement	0.051 ± 0.002
Standard deviation	0.004
Maximum detected displacement	0.056
Minimum detected displacement	0.042

3.2. Radiation-hard sensor

Tests were conducted on two beam patterns: one with a single line (figure 9) and the other with two lines (figure 10), with the results summarized in the table 7. The comparison showed that

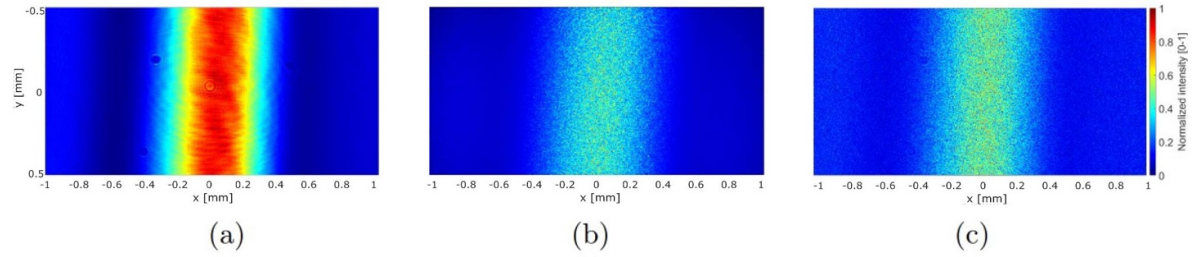


Figure 9. Measured transversal intensity distributions of a single line (a) without fiber matrix, (b) after the fiber matrix, (c) with induced noise.

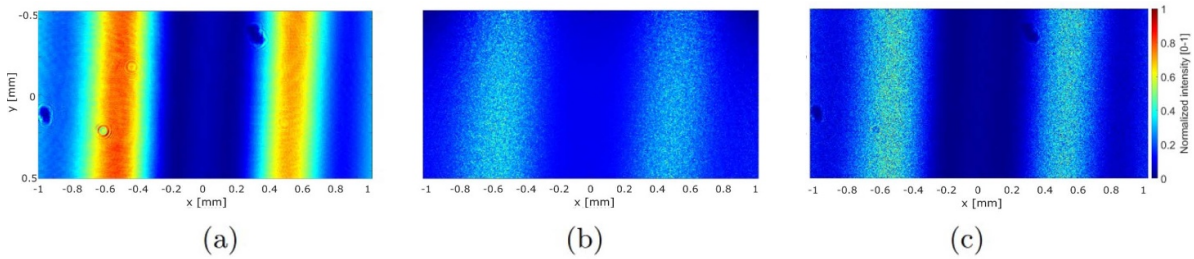


Figure 10. Measured transversal intensity distributions of two lines (a) without fiber matrix, (b) after the fiber matrix, (c) with induced noise.

Table 7. The results of how the fiber matrix influences the detection accuracy of the reference plane.

Metric	One line	Two lines
Baseline PSNR (dB)	33.46	34.87
PSNR (dB)	19.75	14.55
RMSE (μm)	1.24 ± 0.42	0.71 ± 0.25
Maximum error (μm)	2.72	2.19

the PSNR was notably affected by the fiber matrix, indicating a significant impact on the signal-to-noise ratio in the image.

For the single-line pattern, the PSNR decreased from the baseline value of 33.46 dB to 19.75 dB after fiber transmission. Analysis of the extracted LB signals showed corresponding values of RMSE equal to 1.24 ± 0.42 μm and of a maximum error of 2.72 μm. For the multi-line pattern, the PSNR decreased from 34.87 dB to 14.55 dB, with a corresponding RMSE of 0.71 ± 0.25 μm and a maximum error of 2.19 μm.

4. Discussion

4.1. Layer beam-based alignment system

Presented results suggest that the LBs-based alignment system could be a viable candidate for future alignment applications. However, the experimental results revealed deviations from ideal alignment reference planes. This was primarily caused by the analysis of the signals superimposed with noise. The dominant source of this noise originates from interference effects caused by multiple reflections within the quartz cover window and the protective pixel film of the sensor. These components create several partially reflective interfaces. When the incident beam is not perpendicular to the cover window, multiple internal reflections generate constructive and destructive interference patterns that manifest as spatial modulations superimposed upon the detected intensity profile, explaining the clear asymmetries observed in certain sensors or at particular positions throughout our measurements. This effect was evident during the experiments, where we made significant efforts to align the sensors as perpendicular as possible to the beam precisely to mitigate such interference-induced distortions.

Additional distortion was caused by the non-homogeneous refractive index of the propagation medium. The fluctuations of the centroid coordinate in time, detected at each individual sensor, increase with the distance from the LB generator. This is because the beam travels in the medium with a turbulent and non-homogeneous refractive index for a longer time. Additionally, the angular refraction effects causing the beam to deviate are more pronounced with increased distance.

The temporal stability experiment revealed differences in stability between the vertical and horizontal reference planes. The vertical plane demonstrated higher stability relative to the horizontal plane. To investigate this discrepancy further, the sensors were rotated by 90 degrees, effectively swapping the CMOS chips responsible for detecting each plane. This rotation inverted the observed trend, reinforcing the conclusion

that signal distortions arise predominantly from interactions with the cover glass and the protective pixel layer of the CMOS chips. Furthermore, this trend could also be partly caused by fiducialization, which can introduce errors that lead to systematic offsets in the reference plane and thus affect overall alignment accuracy.

High-frequency noise primarily originated from reflections within the pipe or from other incidental objects, resulting in speckle patterns. Although the use of non-reflective pipes helped to minimize these effects, the speckle noise can significantly degrade the signal-to-noise ratio, as we documented in our previous publication [43]. Additionally, dark noise inherent to the CMOS chip was consistently present, however, under the illumination conditions used, it remained relatively stationary and had a less significant influence on the measurement uncertainty.

Controlled shifts of the reference planes using the parallel plate window confirmed the system's repeatability but again emphasized the sensitivity to small variations in the beam angle relative to the cover window of the CMOS chip. Relative alignment tests showed that the system could successfully detect known displacements induced by a linear motor, with the mean detected displacement closely matching the expected 50 µm. This residual error can be attributed to the noise sources described above.

Currently, multiple noise sources act concurrently: interference from sensor windows and coatings, reflections causing speckle noise, intrinsic dark noise, as well as atmospheric disturbances from refractive index gradients and air turbulence. This superposition complicates the quantitative disentanglement of individual noise contributions, given the present hardware and environmental constraints. Planned system upgrades, including the use of CMOS chips with anti-reflective coated cover windows, removal of the protective pixel layer, and integrated dark noise correction, should mitigate sensor-related noise. Additionally, the LBs will be propagated through a vacuum pipe designed to reduce atmospheric-induced distortions. This pipe will feature a non-reflective internal surface treatment and include apertures aimed at suppressing internal reflections and limiting speckle noise. Once these measures are implemented, systematic quantification and prioritization of the individual noise sources will become feasible, enabling scaled deployment of the system over longer distances as envisioned for the future alignment system.

4.2. Radiation-hard sensor

The experimental results demonstrate the potential feasibility of using fiber matrix systems for radiation-hard sensors in accelerator environments. Integrating a fiber matrix system into the sensor design could effectively protect electronics from radiation-induced damage while maintaining alignment accuracy comparable to direct CMOS detection.

The fiber matrix successfully transmitted the LB signal while having a relatively low impact on the accuracy of the reference detection. Comparative analysis of the transversal intensity distributions before and after propagation through the fiber matrix revealed that the PSNR is strongly affected. However, it does not have a significant impact on the analysis of the LB signal. For both single-line and multi-line beam patterns, the RMSE remained below 1.30 µm, with a maximum error of 2.72 µm.

The comparison between the single-line and two-line beam patterns revealed that the two-line configuration provided a lower RMSE. The centroid calculation most likely becomes less sensitive to localized noise, leading to improved stability and precision in reference plane detection. Thus, employing a multi-line beam structure could enhance noise resilience.

5. Conclusion

The present study primarily focused on gaining insights from the experimental evaluation of the LB-based straight-line reference system over a short 2 m distance when propagating in free-air, laying the groundwork for future scaling to longer distances. The quality of the reference plane generated by the LBs remained stable, with repeatability and reproducibility RMSE values below 30 µm. The relative alignment measurements achieved repeatability with a standard deviation of 4 µm. The results demonstrate that the system provides a reliable level of accuracy and precision despite inherent limitations and imperfections in the current setup. The essential sources of noise that must be addressed before further scaling to longer distances can be realized, were identified. These include interference effects caused by the cover glass and the protective pixel film, speckle noise, non-homogeneous refractive index in the propagation medium, as well as the inherent dark noise of the CMOS chips.

The key advantage of the LBs-based alignment system is its ability to measure multiple points simultaneously along its propagation path without obstructing the beam. Compared to the state-of-the-art straight-line alignment systems, an additional degree of freedom (the roll) could be measured. The system could serve as a viable alternative to traditional straight-line reference alignment systems by eliminating the need for mechanical shutters, which are commonly required in many optical-based systems, while allowing for the scaling of the length of the reference line.

The radiation-hard sensor concept, which utilizes the fiber matrix, introduced an additional RMSE below 1.3 µm, confirming its potential for use in high-radiation environments. In the future, a sensor with integrated fiber matrices needs to be developed and employed in a real alignment scenario for further analysis. Additionally, effects such as fiber degradation over time caused by radiation need to be investigated [44].

Data availability statement

The data that support the findings of this study are available upon reasonable request from the authors.

Acknowledgments

The authors acknowledge the financial support provided by the Knowledge Transfer group at CERN through the KT Fund.

This work was partly supported by the Student Grant Scheme at the Technical University of Liberec through project SGS-2025-3583.

Conflict of interest

The authors declare that they have no known competing financial interests or personal relationships that could have appeared to influence the work reported in this study.

ORCID iDs

Martin Dušek 0000-0002-1832-9547
Dirk Mergelkuhl 0000-0002-3399-4289

References

[1] Gayde J-C, Polak K and Šulc M 2022 Introduction to structured laser beam for alignment and status of the r&d *Technical Report* CERN-BE-2023-013 CERN *Proc. 16th Int. Workshop on Accelerator Alignment (IWAA 2022)*
[2] Herty A, Jaros J, Kucel K, Durand H M, Marin A, Rude V, Sosin M and Zemanek A 2018 HL-LHC alignment requirements and associated solutions *Proc. 15th Int. Workshop on Accelerator Alignment*
[3] Durand H M, Watrelot L and Weyer B 2024 Geodetic, survey and alignment challenges of the FCC-ee *J. Instrum.* **19** T02006
[4] Niewiem W, Polak K, Dušek M, Mergelkuhl D, Gayde J-C, Wieser A and Šulc M 2023 Variation of Structured laser beam pattern and optimization for an alignment reference line creation *Opt. Express* **31** 43307–22
[5] Eddy N *et al* 2012 A wire position monitor system for the 1.3 GHz tesla-style cryomodule at the fermilab new-muon-lab accelerator *Technical Report* (arXiv:1209.4917)
[6] Volk J T, Fellenz B, Prieto P, Semenov A, Voy D C and Wendt M 2006 Hydro static water level systems at Fermilab *Proc. 9th Int. Workshop on Accelerator Alignment* pp 26–29
[7] Wang W 2010 *A Prototype Wire Position Monitoring System* (SLAC National Accelerator Laboratory) Technical Note SLAC-TN-10-073
[8] Durand H M, Bestmann P, Herty A, Marin A and Rude V 2012 oWPS versus cWPS *Proc. 12th Int. Workshop on Accelerator Alignment*, Number CERN-ATS-2012-271
[9] Biedrawa P *et al* 2022 Full remote alignment system for the high-luminosity large hadron collider HL-LHC *Proc. 16th Int. Workshop on Accelerator Alignment* pp 255–6
[10] Herrmannsfeldt W 1966 SLAC alignment system *Proc. 1966 Linear Accelerator Conf.* p 163
[11] Suwada T, Satoh M, Telada S and Minoshima K 2012 Experimental investigation on focusing characteristics of a He-Ne laser using circular Fresnel zone plate for high-precision alignment of linear accelerators *Rev. Sci. Instrum.* **83** 053302
[12] Luo T, Wang J, He Z, Wang Y and Chen J 2021 A new laser-based alignment method for the multi-slits VSANS in high precision *Nucl. Instrum. Methods Phys. Res. A* **1010** 165526
[13] Feier I 1998 The Poisson alignment reference system implementation at the advanced photon source *Technical Report* Argonne National Lab
[14] Griffith L, Schenz R and Sommargren G 1990 Magnetic alignment and the Poisson alignment reference system *Rev. Sci. Instrum.* **61** 2138–54
[15] Schwalm C 2012 Straight line reference system-status report on Poisson system calibration *Proc. 12th Int. Workshop on Accelerator Alignment (IWAA 2012)*
[16] Zhang C, Hasegawa M and Kanda K 2014 Performance of the iris diaphragm laser alignment system of the Spring-8 *Proc. 13th Int. Workshop on Accelerator Alignment*
[17] Suwada T 2013 Propagation and stability characteristics of a 500-m-long laser-based fiducial line for high-precision alignment of long-distance linear accelerators *Rev. Sci. Instrum.* **84** 093302
[18] Satoh M and Suwada T 2010 Design of collimated laser beam optics for the KEKB injector linac alignment system *Proc. 25th Linear Accelerator Conf. (LINAC 2010)*
[19] Stern G 2016 Study and development of a laser based alignment system for the compact linear collider *PhD Thesis* ETH Zurich
[20] Batusov V, Budagov J, Lyablin M, Gayde J-C, Di Girolamo B, Mergelkuhl D and Nessi M 2015 The laser fiducial line measurement precision in open air media determined in comparison with laser tracker AT-401 *Phys. Part. Nucl. Lett.* **12** 297–304
[21] Gayde J-C and Šulc M 2019 An optical system for producing a structured beam *Patent* EP3564734
[22] Durnin J 1987 Exact solutions for nondiffracting beams. I. the scalar theory *J. Opt. Soc. Am. A* **4** 651–4
[23] Reichold A 2006 The LiCAS-RTRS – a rapid and cost efficient survey system for the ILC *Proc. Int. Workshop on Accelerator Alignment*
[24] Dušek M, Figura S, Gayde J-C and Šulc M 2024 Generation of pseudo-nondiffracting symmetrical Layer beams using cylindrical lenses *Opt. Express* **32** 42368–82
[25] Siviloglou G A and Christodoulides D N 2007 Accelerating finite energy Airy beams *Opt. Lett.* **32** 979–81
[26] Siviloglou G A, Broky J, Dogariu A and Christodoulides D N 2007 Observation of accelerating Airy beams *Phys. Rev. Lett.* **99** 213901
[27] Vaveliuk P, Lencina A, Rodrigo J A and Matos O M 2014 Symmetric Airy beams *Opt. Lett.* **39** 2370–3
[28] Vaveliuk P, Lencina A, Rodrigo J A and Martnez-Matos Ó 2015 Intensity-symmetric Airy beams *J. Opt. Soc. Am. A* **32** 443–6
[29] Dušek M, Gayde J-C and Šulc M 2024 Generation of symmetrical optical caustic beams for precise alignment *Proc. IPAC'* vol 24 pp 3333–6
[30] Stavroudis O N 1972 *The Optics of Rays, Wavefronts and Caustics* (Academic)
[31] Wang C, Ouyang M and Hong W 2024 Propagation of intense catastrophe beams in air *J. Opt. Soc. Am. B* **41** 373–83
[32] Zannotti A, Diebel F, Boguslawski M and Denz C 2017 Optical catastrophes of the swallowtail and butterfly beams *New J. Phys.* **19** 053004
[33] Wu Y, Chen L, Li Y, Ding W and Yu S 2021 Symmetric pearcey gaussian beams *Opt. Lett.* **46** 2461–4
[34] Wei Q, Chen L, Wu Y, Ding W and Yu S 2023 Symmetric swallowtail beams in the rectangle frame *Ann. Phys.* **535** 2200466
[35] Photonics H CMOS linear image sensors (available at: www.hamamatsu.com/content/dam/hamamatsu-photonics/sites/documents/99_SALES_LIBRARY/ssd/cmos_linear_kmpd9017e.pdf)
[36] Callister W D and Rethwisch D G 2020 *Materials Science and Engineering: An Introduction* 10th edn (Wiley)
[37] Ivanova O, Halouski A, Martynenko D, Vitushkin S and Shutau A V 2022 Thermal expansion of plastics used for 3D printing *Polymers* **14** 3061
[38] Touzé T 2010 Feasibility of the CLIC metrological reference network *Proc. 11th Int. Workshop on Accelerator Alignment (IWAA 2010)*

[39] Polak K, Gayde J and Šulc M 2022 Structured laser beam for alignment and large-scale metrology *Proc. Euspen's 22nd Int. Conf. Exhibition* pp 301–4
[40] Hocken R J and Pereira P H 2012 *Coordinate Measuring Machines and Systems* (CRC Press)
[41] Dušek M, Roikova E, Mergelkuhl D, Gayde J-C, Polak K and Šulc M 2024 Analysis of centroiding algorithms for non-diffracting structured and hollow Structured laser beams *Appl. Opt.* **63** 263–74
[42] Korhonen J and You J 2012 Peak signal-to-noise ratio revisited: is simple beautiful? *Proc. 4th Int. Workshop on Quality of Multimedia Experience* pp 37–38
[43] Dušek M, Figura S, Gayde J-C and Šulc M 2024 Layer beams and their prospect for long-range alignment *Proc. 17th Int. Workshop on Accelerator Alignment (IWAA 2024)*
[44] Girard S *et al* 2019 Overview of radiation induced point defects in silica-based optical fibers *Opt. Fiber Technol.* **52** 101981

8 Conclusion

The thesis has successfully bridged the gap between advances in the field of pseudo-nondiffracting beams and their practical implementation for high precision alignment of particle accelerators. Throughout the thesis, the objectives have been systematically met, suggesting that optical-based systems employing SLBs and LBs could offer a promising alternative to the state-of-the-art straight-line alignment systems. This is enabled by structured beam profiles and low divergence of certain parts of these beams in the order of 10 µrad [45, 61, 62], which allows for a simple detection of the alignment reference position even at distances in the order of hundreds of meters. Unlike traditional wire-based alignment systems, optical-based systems eliminate concerns about wire fragility, length limitations, and sensitivity to gravity. The results, presented in a series of six interconnected publications, further underline the potential use of SLB-based and LB-based alignment systems and provide a strong baseline for future research and development of these systems. In summary, the core results of this thesis are:

- The development of a novel technique for wavefront reconstruction of SLBs, combining artificial intelligence with least-squares fitting to estimate the dominant symmetrical Zernike coefficients (defocus and spherical aberrations) from a single intensity distribution. This approach achieved the RMSE below 0.09λ, demonstrating high accuracy in both simulated and experimental conditions, and enabling precise characterization of beam properties critical for alignment applications [123]. The method was additionally tested for the detection of non-symmetrical aberrations [124].

- The systematic analysis of centroiding algorithms on simulated data of SLBs and HSLBs, benchmarking their accuracy, robustness to noise, and computational efficiency. The gamma-corrected center of gravity algorithm was found to provide the best performance for SLBs, with mean absolute errors below 10^{-2} pixels even under moderate noise, while correlation template matching was most robust for hollow beams. These results confirm that centroiding algorithm errors are not the limiting factor for alignment accuracy in controlled, relatively high signal-to-noise environments, as the induced error would be sub-micrometer for the common size of the pixel in units or tens of micrometers [113]. This is underlined by experimental verification, where the main precision limiting factors in the experiment were fluctuation and gradient of the refractive index of the propagation medium [62].

- The development of means for generating symmetrical LBs using plano-convex cylindrical lenses, enabling the production of pseudo-nondiffracting beams with tunable divergence and pattern shape. This approach was validated through simulations and experiments, demonstrating adaptability for long-distance alignment applications while maintaining cost-effectiveness compared to SLM-based generation methods [114]. The optimization for long-distance propagation on a 140 m experimental bench was conducted, and the precision of the detection algorithms of the alignment reference plane was experimentally validated with the standard deviation of 0.7 µm [119]. The reflections inside the metallic vacuum pipe can also be a limiting factor for the algorithms due to the creation of speckles, which interfere with the beam [63].

- The experimental demonstration of a straight-line reference alignment system based on LBs and custom hollow sensors, achieving repeatability and reproducibility with root-mean-square errors below 30.0 µm over a 2 m length and relative alignment precision with a standard deviation of 4.3 µm. The system has the ability to perform simultaneous multi-point measurements, and in addition to state-of-the-art straight-line reference systems, measure the additional degree of freedom - the roll. A proof-of-concept for a radiation-hard sensor using optical fiber matrices was validated, maintaining an RMSE of the alignment reference below 1.3 µm. Sensors equipped with a fiber matrix could be a suitable option for deployment in high-radiation areas, which are common in particle accelerator tunnels. The signal could be transferred out of these areas, so the electronics parts can be placed in a safe environment, limiting the radiation-induced damage [122].

Future research and development for a successful integration of an SLB or LB-based straight-line reference systems should focus on several areas:

- The LB-based alignment system with hollow sensors should be scaled up to longer distances. Based on our experience, the vacuum pipe is necessary to achieve the alignment requirements. Therefore, an experiment using a test bench with a 140 m vacuum pipe will be conducted. The system will be compared directly with state-of-the-art WPS and HLS systems. However, the CMOS sensors need to be upgraded first to limit the interference effects and dark noise. Additionally, the reflections from the inside surface of the metallic pipe must be further reduced by apertures that could absorb the reflected light, or by other means of noise mitigation.

- The way of upgrading the SLB-based system to be able to measure all the points simultaneously, using, for example, a careful calibration of beam splitters, should be explored and compared to the LB-based system.

- The fiber-based sensors must be further developed. Their robustness to the radiation-induced damage and fiber degradation must be systematically investigated. Successful overcoming of these challenges could lead to the deploy-

ment of the system in future accelerators at CERN, such as FCC, or other scientific facilities.

- Additionally, a preliminary alignment experiment utilizing an SLB-based system propagating the beam over 50 m was conducted at the SuperKEKB accelerator complex in Japan. Note that the results were not presented in this thesis. It is mentioned now, as it suggests an interesting future research topic. The results suggest that in order to achieve the required alignment accuracy, it is necessary to limit the influence of the atmosphere on the beam straightness. The vacuum pipe can not be installed in the SuperKEKB tunnel. Therefore, the development of a system that could be used when the beam propagates in the atmosphere, while compensating for the influence of refraction, is highly desirable. Potential strategies include spatially resolved measurements of the temperature (and potentially pressure or humidity) profile along the beam path to model the refractive index distribution, or the deployment of multiple overlapping beams with different wavelengths, exploiting the distinct refractive indices to compensate through differential analysis, as the refraction would be different for both beams.

In conclusion, the thesis has addressed the challenge of developing high-precision, scalable, and robust alignment systems for next-generation particle accelerators, based on the use of pseudo-nondiffracting optical beams as straight-line references. The development of such a system has the potential to meet the alignment requirements of future high-energy physics facilities.

Bibliography

[1] H. M. DURAND, L. WATRELOT, and B. WEYER. Geodetic, survey and alignment challenges of the FCC-ee. *Journal of Instrumentation*, 19(02): T02006, 2024. doi: 10.1088/1748-0221/19/02/T02006.

[2] S. ANDERSON and T. RAUBENHEIMER. Resolution and systematic limitations in beam-based alignment. *Phys. Rev. ST Accel. Beams*, 3(5):052801, 2000. doi: 10.1103/PhysRevSTAB.3.052801.

[3] J.-C. GAYDE. Survey and alignment of accelerators. In *Proceedings of the Joint Universities Accelerator School (JUAS) — Courses and Exercises*, volume 3 of *CERN Yellow Reports: School Proceedings*, pages 1601–1636. CERN, 2024. doi: 10.23730/CYRSP-2024-003.1601.

[4] L. W. JONES. Genesis of the Large Hadron Collider. *Philosophical Transactions: Mathematical, Physical and Engineering Sciences*, 370:995–1004, 2012. doi: 10.1098/rsta.2011.0468.

[5] R.-D. HEUER. CERN and 60 years of science for peace. In *AIP Conference Proceedings*, volume 1645, pages 430–436. American Institute of Physics, 2015. doi: 10.1063/1.4909616.

[6] D. MISSIAEN, J. QUESNEL, and R. STEINHAGEN. The alignment of the LHC. In *Proceedings of the Particle Accelerator Conference (PAC'09)*, pages 1973–1975, Vancouver, Canada, 2009. URL https://accelconf.web.cern.ch/pac2009/papers/we4grc04.pdf.

[7] Rudiger SCHMIDT. The CERN SPS proton–antiproton collider. *Challenges and Goals for Accelerators in the XXI Century*, pages 153–167, 2016. doi: 10.1142/9789814436403_0010.

[8] S. REDAELLI. Dynamic alignment in particle accelerators. 2009. doi: 10.5170/CERN-2009-005.535.

[9] V. BATUSOV, J. BUDAGOV, M. LYABLIN, J.-C. GAYDE, B. DI GIROLAMO, D. MERGELKUHL, and M. NESSI. The laser fiducial line measurement precision in open air media determined in comparison with laser tracker AT-401. *Physics of Particles and Nuclei Letters*, 12(2):297–304, 2015. doi: 10.1134/S1547477115020053.

[10] F. COLLABORATION. Fcc-ee: The lepton collider: Future Circular Collider conceptual design report volume 2. *European Physical Journal: Special Topics*, 228(2):261–623, 2019. doi: 10.1140/epjst/e2019-900045-4.

[11] Compact linear collider CLIC. https://home.cern/science/accelerators/compact-linear-collider.

[12] H. DURAND MAINAUD. The CLIC alignment studies: past, present and future. *Proceedings of IWAA2004*, 2004. URL https://cds.cern.ch/record/1350229.

[13] P. BIEDRAWA, E. BLANCO VINUELA, C. CALA FRANCO, J. GONZALEZ COBAS, M. DI CASTRO, M. DONZE, J. L. FALCAO MACHADO, S. FARGIER, B. FERNANDEZ ADIEGO, A. HERTY, J. KAMPP, F. KLUMB, W. JASONEK, M. M. LIPINSKI, H. MAINAUD DURAND, A. MASI, M. NOIR, P. PERONNARD, B. SCHOFIELD, P. SOLLANDER, M. SOSIN, and V. RUDE. Full remote alignment system for the high-luminosity large hadron collider HL-LHC. In *Proceedings of the 16th International Workshop on Accelerator Alignment*, volume 21, pages 255–256, CERN, Geneva, Switzerland, 2022. doi: 10.17181/CERN-BE-2023-007.

[14] M. SOSIN, V. BARBARROUX, P. BIEDRAWA, J. CALMELS, M. DANDEKAR, J. FALCAO MACHADO, R. FERNANDEZ BAUTISTA, C. CALA FRANCO, A. HERTY, J. KAMPP, W. JASONEK, H. MAINAUD DURAND, M. NOIR, B. PUDLO, V. RUDE, and P. SARVADE. Alignment system tests on the CERN remote alignment system mock-up. In *Proceedings of the 14th International Workshop on Accelerator Alignment (IWAA)*, 2024. URL https://cds.cern.ch/record/2938903.

[15] L. WATRELOT. *FCC-ee Machine Detector Interface Alignment System Concepts*. PhD Thesis, HESAM Université, 2023. URL https://cds.cern.ch/record/2894663. CERN-THESIS-2023-376.

[16] A. HERTY, J. JAROS, K. KUCEL, H. MAINAUD DURAND, A. MARIN, V. RUDE, M. SOSIN, and A. ZEMANEK. HL-LHC alignment requirements and associated solutions. In *Proc. 15th Int. Workshop on Accelerator Alignment*, FNAL, Batavia, IL, USA, 2018. doi: 10.18429/JACoW-IPAC2017-TUPIK085.

[17] J. GUTEKUNST, M. SOSIN, F. KLUMB, H. M. DURAND, and G. KAUTZMANN. Continuous position estimation for the full remote alignment system of the high luminosity LHC upgrade. *JACoW IPAC*, 2024:THPG36, 2024. doi: 10.18429/JACoW-IPAC2024-THPG36.

[18] Y. SHEN, S. PIDISHETY, I. NAPE, and A. DUDLEY. Self-healing of structured light: a review. *Journal of Optics*, 24(10):103001, 2022. doi: 10.1088/2040-8986/ac8888.

[19] H. ZHONG, Y. ZHANG, M. R. BELIĆ, C. LI, F. WEN, Z. ZHANG, and Y. ZHANG. Controllable circular Airy beams via dynamic linear potential. *Optics Express*, 24(7):7495–7506, Apr 2016. doi: 10.1364/OE.24.007495.

[20] J. DURNIN, J. J. Jr. MICELI, and J. H. EBERLY. Comparison of Bessel and Gaussian beams. *Optics Letters*, 13(2):79–80, 1988. doi: 10.1364/ol.13.000079.

[21] S. LI, L. LI, T. LIU, and X. DENG. Non-Diffracting Light Wave: Fundamentals and Biomedical Applications. *Frontiers in Physics*, 9:698343, 2021. doi: 10.3389/fphy.2021.698343.

[22] A. FORBES, M. DE OLIVEIRA, and M. R. DENNIS. Structured Light. *Nature Photonics*, 15(4):253–262, 2021. doi: 10.1038/s41566-021-00780-4.

[23] M. V. BERRY and C. UPSTILL. IV Catastrophe optics: Morphologies of caustics and their diffraction patterns. *Progress in optics*, 18:257–346, 1980. doi: 10.1016/S0079-6638(08)70215-4.

[24] M. A. BUTT and S. N. KHONINA. Non-Diffractive Beams for State-of-the-Art Applications. *Micromachines*, 15(6):771, 2024. doi: 10.3390/mi15060771.

[25] S. N. KHONINA, N. L. KAZANSKIY, and S. V. KARPEEV. Bessel beam: Significance and applications — A progressive review. *Micromachines*, 11(11): 997, 2020. doi: 10.3390/mi11110997.

[26] ISO, IEC, BIPM, OIML, IFCC, ILAC, IUPAC, and IUPAP. *Guide to the Expression of Uncertainty in Measurement, Part 1: Introduction*. International Organization for Standardization, Geneva, 2024. ISBN 978-9267101880.

[27] JCGM. *International Vocabulary of Metrology – Basic and General Concepts and Associated Terms (VIM)*. Joint Committee for Guides in Metrology, 2012. ISBN 978-92-67-10452-1.

[28] B. HOFMANN-WELLENHOF and H. MORITZ. *Physical Geodesy*. Springer, Vienna, 2 edition, 2006. ISBN 978-3-211-33544-4.

[29] R. E. RULAND. Accelerator and transport line survey and alignment. In *AIP Conference Proceedings*, volume 255, pages 112–130, 05 1992. doi: 10.1063/1.42311.

[30] A. LEICK, L. RAPOPORT, and D. TATARNIKOV. *GPS Satellite Surveying*. John Wiley & Sons, Hoboken, New Jersey, 2015. ISBN 9781119018612.

[31] C. JEKELI. *Geometric Reference Systems in Geodesy*. Ohio State University, Columbus, Ohio, 2012.

[32] H. MAINAUD DURAND, P. BESTMANN, A. HERTY, A. MARIN, and V. RUDE. oWPS versus cWPS. In *Proceedings 12th Int. Workshop on*

Accelerator Alignment, Fermilab, Batavia, IL, USA, number CERN-ATS-2012-271 in CERN Reports, Geneva, Switzerland, October 2012. URL https://cds.cern.ch/record/1493031.

[33] P. SAINVITU, P. DEWITTE, J.-C. GAYDE, D. MERGELKUHL, and D. MISSIAEN. Tsunami, an unified in-field measurement and alignment software for experiments and accelerators at CERN large scale metrology section. In *IWAA2016: 14th International Workshop on Accelerator Alignment*, Grenoble, France, 10 2016. URL https://cds.cern.ch/record/2680565.

[34] M. BARBIER. LGC: A new revised version. In *Proceedings of the 14th International Workshop on Accelerator Alignment (IWAA 2016)*, Grenoble, France, October 2016. URL https://indico.cern.ch/event/489498/contributions/2217518/.

[35] N. R. KINEMATICS. SpatialAnalyzer (SA). https://www.kinematics.com, 2025.

[36] R. J. HOCKEN and P. H. PEREIRA. *Coordinate measuring machines and systems*, volume 6. CRC press Boca Raton, FL, USA:, 2012. ISBN 978-1-57444-652-4. doi: 10.1201/b11022.

[37] J. A. SŁADEK. Coordinate metrology. *Springer Tracts in Mechanical Engineering*, pages 1–13, 2016. doi: 10.1007/978-3-662-48465-4.

[38] D. CAIAZZA, N. CATALAN LASHERAS, H. MAINAUD DURAND, M. MODENA, C. SANZ, D. TSHILUMBA, V. VLACHAKIS, M. WENDT, and S. ZORZETTI. New solution for the high accuracy alignment of accelerator components. *Physical Review Accelerators and Beams*, 20(8):083501, 2017. doi: 10.1103/PhysRevAccelBeams.20.083501.

[39] W. T. ESTLER, K. L. EDMUNDSON, G. N. PEGGS, and D. H. PARKER. Large-scale metrology–an update. *CIRP Annals*, 51(2):587–609, 2002. doi: 10.1016/S0007-8506(07)61702-8.

[40] N. EDDY, B. FELLENZ, P. PRIETO, A. SEMENOV, D. C. VOY, and M. WENDT. A wire position monitor system for the 1.3 GHz tesla-style cryomodule at the fermilab new-muon-lab accelerator. Technical report, 2012. URL https://arxiv.org/abs/1209.4917.

[41] J. T. VOLK, B. FELLENZ, P. PRIETO, A. SEMENOV, D. C. VOY, and M. WENDT. Hydro static water level systems at Fermilab. In *Proceedings 9th Int. Workshop on Accelerator Alignment, Stanford Univ., Palo Alto, CA*, pages 26–29, 2006. URL https://core.ac.uk/outputs/71313885/.

[42] W. WANG. A prototype wire position monitoring system. Technical Note SLAC-TN-10-073, SLAC National Accelerator Laboratory, Menlo Park, CA, USA, 2010. URL https://www.slac.stanford.edu/pubs/slactns/tn04/slac-tn-10-073.pdf.

[43] D. A. FELLOWES. Kinematic and quasi-kinematic constraints: What they are & how to design them. Technical report, University of Arizona, College of Optical Sciences, 2006. URL https://wp.optics.arizona.edu/optomech/wp-content/uploads/sites/53/2016/10/FellowesTutorial1.pdf.

[44] T. TOUZÉ. Feasibility of the clic metrological reference network. In *Proceedings of the 11th International Workshop on Accelerator Alignment (IWAA 2010)*, DESY, Hamburg, Germany, 2010. URL https://agenda.linearcollider.org/event/4507/contributions/17907/attachments/14446/23674/IWAA_2010_ttouze_article_corrected.pdf.pdf.

[45] W. NIEWIEM, K. POLAK, M. DUŠEK, D. MERGELKUHL, J.-C. GAYDE, A. WIESER, and M. ŠULC. Variation of Structured laser beam pattern and optimization for an alignment reference line creation. *Optics Express*, 31(26): 43307–43322, 2023. doi: 10.1364/OE.503016.

[46] G. STERN. *Study and development of a laser based alignment system for the compact linear collider*. PhD Thesis, ETH Zurich, 2016. CERN-THESIS-2016-030.

[47] M. BEKER, G. BOBBINK, B. BOUWENS, N. DEELEN, P. DUINKER, J. VAN ELDIK, N. DE GAAY FORTMAN, R. VAN DER GEER, H. VAN DER GRAAF, H. GROENSTEGE, R. HART, K. HASHEMI, J. VAN HEIJNINGEN, M. KEA, J. KOOPSTRA, X. LEIJTENS, F. LINDE, J. A. PARADISO, H. TOLSMA, and M. WOUDSTRA. The Rasnik 3-point optical alignment system. Technical Report 08, aug 2019.

[48] S. PALESTINI. The muon spectrometer of the ATLAS experiment. Technical report, CERN, 2003.

[49] N. DEELEN. Pre-Alignment of CLIC, Rasclic versus WPS. Master's thesis, Utrecht University, 2015. URL https://studenttheses.uu.nl/handle/20.500.12932/23801.

[50] C. ZHANG, M. HASEGAWA, and K. KANDA. Performance of the iris diaphragm laser alignment system of the Spring-8. In *Proceedings 13th Int. Workshop on Accelerator Alignment*, Beijing, China, 2014. URL https://www.slac.stanford.edu/econf/C1410132/papers/120.pdf.

[51] T. SUWADA. Propagation and stability characteristics of a 500-m-long laser-based fiducial line for high-precision alignment of long-distance linear accelerators. *Review of Scientific Instruments*, 84(9):093302, Sep 2013. doi: 10.1063/1.4819960.

[52] M. SATOH and T. SUWADA. Design of collimated laser beam optics for the KEKB injector linac alignment system. In *Proceedings of the 25th Linear Accelerator Conference (LINAC 2010)*, Tsukuba, Japan, 2010. URL https://accelconf.web.cern.ch/LINAC2010/papers/thp076.pdf.

[53] W. HERRMANNSFELDT. SLAC alignment System. In *Proceedings of the 1966 Linear Accelerator Conference*, page 163, 1966. URL https://accelconf.web.cern.ch/l66/papers/iv-05.pdf.

[54] T. SUWADA, M. SATOH, S. TELADA, and K. MINOSHIMA. Experimental investigation on focusing characteristics of a He-Ne laser using circular Fresnel zone plate for high-precision alignment of linear accelerators. *Review of scientific instruments*, 83(5), 2012. doi: 10.1063/1.4709497.

[55] T. LUO, J. WANG, Z. HE, Y. WANG, and J. CHEN. A new laser-based alignment method for the multi-slits VSANS in high precision. *Nuclear Instruments and Methods in Physics Research Section A: Accelerators, Spectrometers, Detectors and Associated Equipment*, 1010:165526, 2021. doi: 10.1016/j.nima.2021.165526.

[56] I. FEIER. The Poisson alignment reference system implementation at the advanced photon source. Technical report, Argonne National Lab., 09 1998. URL https://www.osti.gov/biblio/10970.

[57] L. GRIFFITH, R. SCHENZ, and G. SOMMARGREN. Magnetic alignment and the Poisson alignment reference system. *Review of scientific instruments*, 61(8):2138–2154, 1990. doi: 10.1063/1.1141381.

[58] C. SCHWALM. Straight line reference system-status report on Poisson system calibration. In *Proceedings of the 12th International Workshop on Accelerator Alignment (IWAA 2012)*, Batavia, IL, USA, 2012. Fermi National Accelerator Laboratory. URL https://www.slac.stanford.edu/econf/C1209102/papers/Paper_46-0-IWAA_2012_Schwalm.pdf.

[59] D. KÄMTNER and J. PRENTING. Straight line reference system (slrs) for the adjustment of the x-ray free-electron laser (xfel) at desy. In *9th International Workshop on Accelerator Alignment*, pages 26–29, Hamburg, Germany, Sep 2006. URL https://www.slac.stanford.edu/econf/C06092511/papers/TH008.PDF.

[60] W. NIEWIEM, S. FIGURA, M. DUŠEK, J. M. POLAK, J.-C. GAYDE, and A. WIESER. Shutter-type multi-point optical alignment using a structured laser beam in vacuum. *Journal of Instrumentation*, 20(07):P07001, jul 2025. doi: 10.1088/1748-0221/20/07/P07001.

[61] J.-C. GAYDE, M. DUŠEK, D. MERGELKUHL, K. POLAK, E. ROIKOVA, W. NIEWIEM, and M. ŠULC. The potential contribution of a Structured laser beam to accelerator alignment technology. In *Proceedings IPAC'23*, Venice, Italy, May 2023. JACoW Publishing. doi: 10.18429/JACOW-IPAC2023-THPA041.

[62] M. DUŠEK, K. POLAK, J.-C. GAYDE, M. ŠULC, D. MERGELKUHL, and W. G. NIEWIEM. Detection of Structured laser beam centroid and its use for

alignment. In *Proceedings of the 16th International Workshop on Accelerator Alignment (IWAA 2022)*, Geneva, Switzerland, 2022. CERN. URL https://cds.cern.ch/record/2849064.

[63] M. DUŠEK, S. FIGURA, J.-C. GAYDE, and M. ŠULC. Layer beams and their prospect for long-range alignment. In *17th International Workshop on Accelerator Alignment*, SLAC, San Francisco, California, USA, October 7.-11. 2024. URL https://indico.slac.stanford.edu/event/9126/contributions/10226/.

[64] P. FIALA and I. RICHTER. *Fyzikální optika*. ČVUT, Praha, 2., přepracované edition, 2005. ISBN 80-01-03183-7.

[65] M. BORN and E. WOLF. *Principles of Optics: Electromagnetic Theory of Propagation, Interference and Diffraction of Light*. Cambridge University Press, 7th (expanded) edition, 1999. ISBN 978-0521642224.

[66] A. ZANNOTTI, F. DIEBEL, M. BOGUSLAWSKI, and C. DENZ. Optical catastrophes of the Swallowtail and Butterfly beams. *New Journal of Physics*, 19(5):053004, 2017. doi: 10.1088/1367-2630/aa6ecd.

[67] C. WANG, M. OUYANG, and W. HONG. Propagation of intense catastrophe beams in air. *Journal of the Optical Society of America B*, 41(2):373–383, 2024. doi: 10.1364/JOSAB.507132.

[68] G. A. SIVILOGLOU and D. N. CHRISTODOULIDES. Accelerating finite energy Airy beams. *Optics Letters*, 32(8):979–981, 2007. doi: 10.1364/OL.32.000979.

[69] G. A. SIVILOGLOU, J. BROKY, A. DOGARIU, and D. N. CHRISTODOULIDES. Observation of accelerating Airy beams. *Phys. Rev. Lett.*, 99(21):213901, 2007. doi: 10.1103/PhysRevLett.99.213901.

[70] Y. WU, L. CHEN, Y. LI, W. DING, and S. YU. Symmetric Pearcey Gaussian beams. *Optics Letters*, 46(10):2461–2464, 2021. doi: 10.1364/OL.425889.

[71] Q. WEI, L. CHEN, Y. WU, W. DING, and S. YU. Symmetric Swallowtail beams in the rectangle frame. *Annalen der Physik*, 535(3):2200466, 2023. doi: 10.1002/andp.202200466.

[72] P. VAVELIUK, A. LENCINA, J. A. RODRIGO, and O. M. MATOS. Symmetric Airy beams. *Optics letters*, 39(8):2370–2373, 2014. doi: 10.1364/OL.39.002370.

[73] P. VAVELIUK, A. LENCINA, J. A. RODRIGO, and MARTNEZ-MATOS. Intensity-symmetric Airy beams. *JOSA A*, 32(3):443–446, 2015. doi: 10.1364/JOSAA.32.000443.

[74] J. WANG, J. BU, M. WANG, Y. YANG, and X. YUAN. Generation of high quality Airy beams with blazed micro-optical cubic phase plates. *Applied optics*, 50(36):6627–6631, 2011. doi: 10.1364/AO.50.006627.

[75] A. BENSTITI, K. FERRIA, and A. BENCHEIKH. Generation of a variety of Airy beams using a dynamic diffractive optical phase element. *J. Opt. Soc. Am. B*, 37(11):A45–A53, Nov 2020. doi: 10.1364/JOSAB.395935.

[76] B. YALIZAY, B. SOYLU, and S. AKTURK. Optical element for generation of accelerating Airy beams. *JOSA A*, 27(10):2344–2346, 2010. doi: 10.1364/JOSAA.27.002344.

[77] L. BEGEL and T. GALSTIAN. Dynamic generation of non-diffracting beams by using an electrically variable liquid crystal lens. *Optics Communications*, 441:127–131, 2019. doi: 10.1016/j.optcom.2019.02.053.

[78] J. MA, Y. LI, Q. YU, Z. YANG, Y. HU, and J. CHU. Generation of high-quality tunable Airy beams with an adaptive deformable mirror. *Optics Letters*, 43(15):3634–3637, 2018. doi: 10.1364/OL.43.003634.

[79] B. WU, B. XU, X. WANG, and H. YING. Generation of a polarization insensitive Airy beam using an all-dielectric metasurface. *Optical Materials Express*, 11(3):842–847, 2021. doi: 10.1364/OME.418910.

[80] B. YU, J. WEN, L. CHEN, L. ZHANG, Y. FAN, B. DAI, S. KANWAL, D. LEI, and D. ZHANG. Polarization-independent highly efficient generation of Airy optical beams with dielectric metasurfaces. *Photonics Research*, 8(7):1148–1154, 2020. doi: 10.1364/PRJ.390202.

[81] Z. CAI, Y. BELLOUARD, J. LOPEZ, J. SIEGEL, and K. SUGIOKA. Continuous cubic phase microplates for generating high-quality Airy beams with strong deflection. *Optics Letters*, 42(13):2483–2486, 2017. doi: 10.1364/OL.42.002483.

[82] B.-Y. WEI, P. CHEN, W. HU, W. JI, L.-Y. ZHENG, S.-J. GE, Y. MING, V. CHIGRINOV, and Y.-Q. LU. Polarization-controllable Airy beams generated via a photoaligned director-variant liquid crystal mask. *Scientific reports*, 5(1):17484, 2015. doi: 10.1038/srep17484.

[83] J. ZHOU, Y. LIU, Y. KE, H. LUO, and S. WEN. Generation of Airy vortex and Airy vector beams based on the modulation of dynamic and geometric phases. *Optics letters*, 40(13):3193–3196, 2015. doi: 10.1364/OL.40.003193.

[84] W. LIANG, W. DING, L. CHEN, and S. YU. Dual Airy beam. *Optics Letters*, 18(22):23504–23516, 2010. doi: 10.1364/OE.18.023504.

[85] N. K. EFREMIDIS and D. N. CHRISTODOULIDES. Abruptly autofocusing waves. *Optics Letters*, 35(23):4045–4047, 2010. doi: 10.1364/OL.35.004045.

[86] D. G. PAPAZOGLOU, N. K. EFREMIDIS, D. N. CHRISTODOULIDES, and S. TZORTZAKIS. Observation of abruptly autofocusing waves. *Optics Letters*, 36(10):1842–1844, 2011. doi: 10.1364/OL.36.001842.

[87] I. CHREMMOS, N. K. EFREMIDIS, and D. N. CHRISTODOULIDES. Pre-engineered abruptly autofocusing beams. *Optics Letters*, 36(10):1890–1892, 2011. doi: 10.1364/OL.36.001890.

[88] R. S. PENCIU, N. K. EFREMIDIS, and D. N. CHRISTODOULIDES. Abruptly autofocusing and autodefocusing optical beams with arbitrary caustics. *Physical Review A*, 85(2):023828, 2012. doi: 10.1103/PhysRevA.85.023828.

[89] P. ZHANG, J. PRAKASH, Z. ZHANG, M. S. MILLS, and N. K. EFREMIDIS. Trapping and guiding microparticles with morphing autofocusing Airy beams. *Optics Letters*, 36(15):2883–2885, 2011. doi: 10.1364/OL.36.002883.

[90] J. DUDUTIS, P. GEČYS, and G. RAČIUKAITIS. Non-ideal axicon-generated Bessel beam application for intra-volume glass modification. *Optics express*, 24(25):28433–28443, 2016. doi: 10.1364/OE.24.028433.

[91] S. N. KHONINA, V. V. KOTLYAR, M. V. SHINKARYEV, V. A. SOIFER, and G. V. USPLENIEV. Rotation of microparticles with Bessel beams generated by diffractive elements. *Journal of Modern optics*, 51(14):2167–2184, 2004. doi: 10.1080/09500340408232521.

[92] N. CHATTRAPIBAN, E. A. ROGERS, D. COFIELD, W. T. HILL III, and R. ROY. Generation of nondiffracting Bessel beams by use of a spatial light modulator. *Optics letters*, 28(22):2183–2185, 2003. doi: 10.1364/OL.28.002183.

[93] D. M. GALE. Visual alignment of mechanical structures using a Bessel beam datum: Practical implementation. In *Optical Measurement Systems for Industrial Inspection VII*, pages 1013–1024. SPIE, 2011. doi: 10.1117/12.889300.

[94] R. E. PARKS. Practical considerations for using grating produced Bessel beams for alignment purposes. In *Proceedings SPIE 11816*, pages 11–18, 2021. doi: 10.1117/12.2594653.

[95] R. E. PARKS. Aligning reflecting optics with Bessel beams. In *Optical System Alignment, Tolerancing, and Verification XIII*, volume 11488, page 114880J. SPIE, 2020. doi: 10.1117/12.2568569.

[96] R. E. PARKS. Rapid centering of optics. In *Optifab 2021*, volume 11488, page 118890V, 2021. doi: 10.1117/12.2601599.

[97] N. ZHANG, X. YUAN, R. E. BURGE, J. TENG, and Q. WANG. Generation of long-distance stably propagating Bessel beams. *OSA Continuum*, 4(4):1223–1233, 2021. doi: 10.1364/OSAC.420125.

[98] P. BIRCH, I. ITUEN, R. YOUNG, and C. CHATWIN. Long-distance Bessel beam propagation through Kolmogorov turbulence. *Journal of the Optical Society of America A*, 32(11):2066–2073, 2015. doi: 10.1364/JOSAA.32.002066.

[99] CH. LYU, R. M. BELIC, Y. LI, and Y. ZHANG. Generation of diffraction-free Bessel beams based on combined axicons. *Optics & Laser Technology*, 164: 109548, 2023. ISSN 0030-3992. doi: 10.1016/j.optlastec.2023.109548.

[100] Y. ZHANG and X. ZHANG. Robust propagation of pin-like optical beam through atmospheric turbulence. *APL Photonics*, 4(7):076103, 2019. doi: 10.1063/1.5095996.

[101] D. LI, D. BONGIOVANNI, M. GOUTSOULAS, S. XIA, Z. ZHANG, Y. HU, D. SONG, R. MORANDOTTI, K. N. EFREMIDIS, and Z. CHEN. Direct comparison of anti-diffracting optical pin beams and abruptly autofocusing beams. *OSA Continuum*, 3(6):1525–1535, Jun 2020. doi: 10.1364/OSAC.391878.

[102] D. LI, T. JIANG, Z. LI, Z. HUANG, X. XIA, J. GAO, J. XU, Y. LIANG, and H. DU. Demonstration of anti-diffracting optical pin-like beam enabled 5Gbit/s OFDM underwater wireless optical communication system. *Optics Communications*, 579:131582, 2025. doi: 10.1016/j.optcom.2025.131582.

[103] Z. CAO, C. ZHAI, J. LI, F. XIAN, and S. PEI. Light sheet based on one-dimensional Airy beam generated by single cylindrical lens. *Optics Communications*, 393:11–16, 2017. doi: 10.1016/j.optcom.2017.02.028.

[104] D. PAPAZOGLOU, S. SUNTSOV, D. ABDOLLAHPOUR, and S. TZORTZAKIS. Tunable intense Airy beams and tailored femtosecond laser filaments. *Physical Review A*, 81(6):061807, 2010. doi: 10.1103/PhysRevA.81.061807.

[105] D. ABDOLLAHPOUR, M. LOTFOLLAHI, M. YEGANEH, and S. RASOULI. Generation and characterization of adjustable pure third-order spatial phase by tuning optical aberrations. *Journal of Optics*, 21(8):085602, 2019. doi: 10.1088/2040-8986/ab2b82.

[106] Z. YANG, A. K. GLASER, S. W. TEITELBAUM, and A. H. VOIE. A compact Airy beam light sheet microscope with a tilted cylindrical lens. *Biomedical optics express*, 5(10):3434–3442, 2014. doi: 10.1364/BOE.5.003434.

[107] R. M. HERMAN and T. A. WIGGINS. Production and uses of diffractionless beams. *JOSA A*, 8(6):932–942, 1991. doi: 10.1364/JOSAA.8.000932.

[108] T. ARUGA. Generation of long-range nondiffracting narrow light beams. *Applied Optics*, 36(16):3762–3768, 1997. doi: 10.1364/AO.36.003762.

[109] T. ARUGA, S. W. LI, S. YOSHIKADO, M. TAKABE, and R. LI. Nondiffracting narrow light beam with small atmospheric turbulence-influenced propagation. *Applied Optics*, 38(15):3152–3156, 1999. doi: 10.1364/AO.38.003152.

[110] K. POLAK, M. DUSEK, M. ŠULC, and J.-C. GAYDE. Approximate analytical description of the Structured laser beam in the far zone. *Optics Express*, 32(27):47673–47705, 2024. doi: 10.1364/OE.531400.

[111] K. POLÁK. Optimization of the properties of structured optical beams. Master's thesis, Technical University of Liberec, 2018. URL https://dspace.tul.cz/handle/15240/32267.

[112] J.-C. GAYDE, K. POLAK, and M. ŠULC. Introduction to Structured laser beam for alignment and status of the R&D. Technical Report CERN-BE-2023-013, CERN, 2022. URL https://cds.cern.ch/record/2849065.

[113] M. DUŠEK, E. ROIKOVA, D. MERGELKUHL, J.-C. GAYDE, K. POLAK, and M. ŠULC. Analysis of centroiding algorithms for non-diffracting structured and hollow Structured laser beams. *Applied Optics*, 63(1):263–274, 2024. doi: 10.1364/AO.509927.

[114] M. DUŠEK, S. FIGURA, J.-C. GAYDE, and M. ŠULC. Generation of pseudo-nondiffracting symmetrical Layer beams using cylindrical lenses. *Optics Express*, 32(24):42368–42382, 2024. doi: 10.1364/OE.537554.

[115] M. DUŠEK, J.-C. GAYDE, and M. ŠULC. Optimization of symmetrical layers of Airy beams generated using cylindrical lenses. In *Proceedings of the 24th European Society for Precision Engineering and Nanotechnology Conference (EUSPEN24)*, Dublin, Ireland, June 2024. European Society for Precision Engineering and Nanotechnology. URL https://www.euspen.eu/knowledge-base/ICE24262.pdf.

[116] L. I. GMBH. VirtualLab Fusion. https://www.lighttrans.com, 2025.

[117] W. T. COCHRAN, J. W. COOLEY, D. L. FAVIN, H. D. HELMS, R. A. KAENEL, W. W. LANG, G. C. MALING, D. E. NELSON, C. M. RADER, and P. D. WELCH. What is the fast fourier transform? *Proceedings of the IEEE*, 55(10):1664–1674, oct 1967. doi: 10.1109/PROC.1967.5957.

[118] T. M. INC. Matlab R2025a. https://www.mathworks.com, 2025.

[119] M. DUŠEK, J.-C. GAYDE, and M. ŠULC. Generation of symmetrical optical caustic beams for precise alignment. In *Proceedings IPAC'24*, pages 3333–3336, Nashville, Tennessee, USA, May 2024. JACoW Publishing. URL https://accelconf.web.cern.ch/ipac2024/pdf/THPG35.pdf.

[120] H. NYQUIST. Certain topics in telegraph transmission theory. *Transactions of the American Institute of Electrical Engineers*, 47(2):617–644, 1928. doi: 10.1109/T-AIEE.1928.5055024.

[121] K. POLAK, J. GAYDE, and M. ŠULC. Structured laser beam for alignment and large-scale metrology. In *Euspen's 22nd International Conference and Exhibition*, pages 301–304, 2022. URL https://www.euspen.eu/knowledge-base/ICE22224.pdf.

[122] M. DUŠEK, S. FIGURA, J. M. POLAK, S. W. KAMUGASA, D. MERGELKUHL, W. NIEWIEM, Š. KUNC, J.-C. GAYDE, and M. ŠULC. First steps toward the development of a straight-line reference alignment system for future accelerators at CERN using pseudo-nondiffracting Layer beams. *Measurement Science and Technology*, 36(10):105009, 2025. doi: 10.1088/1361-6501/ae0ba0.

[123] M. DUŠEK, J.-C. GAYDE, and M. ŠULC. Wavefront reconstruction of a non-diffracting Structured laser beam. *Optics Express*, 31(25):42099–42110, 2023. doi: 10.1364/OE.502452.

[124] M. DUŠEK, J.-C. GAYDE, and M. ŠULC. Wavefront aberration detection of a Structured laser beam using artificial intelligence and its use for alignment. In *Optomechanical Engineering 2023*, volume 12669, pages 139–149, San Diego, California, USA, 2023. SPIE. doi: 10.1117/12.2676015.

[125] A. REICHOLD. The LiCAS-RTRS – A Rapid and Cost Efficient Survey System for the ILC. In *Proceedings Int. Workshop on Accelerator Alignment*, 2006. URL https://www.slac.stanford.edu/econf/C06092511/papers/WE008.PDF.

[126] M DUŠEK. Advanced calibration and characterization of a Shack-Hartmann sensor. Master's thesis, Technical University of Liberec, 2021. URL https://dspace.tul.cz/handle/15240/35483.

List of Author's Publications

Main Author

Papers in Peer-Reviewed Journals

[i] M. DUŠEK, J.-C. GAYDE, and M. SULC. Wavefront reconstruction of a non-diffracting Structured laser beam. *Optics Express*, 31(25):42099–42110, 2023. doi: 10.1364/OE.502452.

[ii] M. DUŠEK, E. ROIKOVA, D. MERGELKUHL, J.-C. GAYDE, K. POLAK, and M. SULC. Analysis of centroiding algorithms for non-diffracting Structured and Hollow Structured laser beams. *Applied Optics*, 63(1):263–274, 2024. doi: 10.1364/AO.509927.

[iii] M. DUŠEK, S. FIGURA, J.-C. GAYDE, and M. ŠULC. Generation of pseudo-nondiffracting symmetrical Layer beams using cylindrical lenses. *Optics Express*, 32(24):42368–42382, 2024. doi: 10.1364/OE.537554.

[iv] M. DUŠEK, S. FIGURA, J. M. POLAK, S. W. KAMUGASA, D. MERGELKUHL, W. NIEWIEM, Š. KUNC, J.-C. GAYDE, and M. ŠULC. First steps toward the development of a straight-line reference alignment system for future accelerators at CERN using pseudo-nondiffracting Layer beams. *Measurement Science and Technology*, 36(10):105009, 2025. doi: 10.1088/1361-6501/ae0ba0

Papers in Conference Proceedings

[i] M. DUŠEK, K. POLAK, J.-C. GAYDE, M. SULC, D. MERGELKUHL, and W. G. NIEWIEM. Detection of Structured laser beam centroid and its use for alignment. In *Proceedings of the 16th International Workshop on Accelerator Alignment (IWAA 2022)*, Geneva, Switzerland, 2022. CERN. URL https://cds.cern.ch/record/2849064.

[ii] M. DUŠEK, J.-C. GAYDE, and M. ŠULC. Wavefront aberration detection of a Structured laser beam using artificial intelligence and its use for alignment. In *Optomechanical Engineering 2023*, volume 12669, pages 139–149, San Diego, California, USA, 2023. SPIE. doi: 10.1117/12.2676015.

[iii] M. DUŠEK, J.-C. GAYDE, and M. ŠULC. Generation of symmetrical optical caustic beams for precise alignment. In *Proceedings IPAC'24*, pages 3333–3336, Nashville, Tennessee, USA, May 2024. JACoW Publishing. URL https://accelconf.web.cern.ch/ipac2024/pdf/THPG35.pdf.

[iv] M. DUŠEK, J.-C. GAYDE, and M. ŠULC. Optimization of symmetrical layers of Airy beams generated using cylindrical lenses. In *Proceedings of the 24th European Society for Precision Engineering and Nanotechnology Conference (EUSPEN24)*, Dublin, Ireland, June 2024. European Society for Precision Engineering and Nanotechnology. URL https://www.euspen.eu/knowledge-base/ICE24262.pdf.

[v] M. DUŠEK, S. FIGURA, J.-C. GAYDE, and M. ŠULC. Layer Beams and their prospect for long-range alignment. In *Proceedings of the 17th International Workshop on Accelerator Alignment (IWAA 2024)*, SLAC, San Francisco, California, USA, October 2024. URL https://indico.slac.stanford.edu/event/9126/contributions/10226/.

Theses

[i] M DUŠEK. Advanced calibration and characterization of a Shack-Hartmann sensor. Master's thesis, Technical University of Liberec, 2021. URL https://dspace.tul.cz/handle/15240/35483.

Co-Author

Papers in Peer-Reviewed Journals

[i] J. TOUS, J. PARIZEK, K. BLAZEK, M. SULC, R. MELICH, M. DUSEK, and T. VANEK. Resolution Limits of a Single Crystal Scintillator Based X-ray Micro-radiography Camera. *Journal of Instrumentation*, 15(02):C02014, 2020. doi: 10.1088/1748-0221/15/02/C02014.

[ii] W. NIEWIEM, K. POLAK, M. DUŠEK, D. MERGELKUHL, J.-C. GAYDE, A. WIESER, and M. SULC. Variation of Structured laser beam pattern and optimization for an alignment reference line creation. *Optics Express*, 31(26): 43307–43322, 2023. doi: 10.1364/OE.503016.

[iii] K. POLAK, M. DUSEK, M. ŠULC, and J.-C. GAYDE. Approximate analytical description of the Structured laser beam in the far zone. *Optics Express*, 32(27):47673–47705, 2024. doi: 10.1364/OE.531400.

[iv] W. NIEWIEM, S. FIGURA, M. DUŠEK, J. M. POLAK, J.-C. GAYDE, and A. WIESER. Shutter-type multi-point optical alignment using a structured laser beam in vacuum. *Journal of Instrumentation*, 20(07):P07001, jul 2025. doi: 10.1088/1748-0221/20/07/P07001.

Papers in Conference Proceedings

[i] J.-C. GAYDE, M. DUŠEK, D. MERGELKUHL, K. POLAK, E. ROIKOVA, W. NIEWIEM, and M. SULC. The potential contribution of a Structured laser beam to accelerator alignment technology. In *Proceedings IPAC'23*, Venice, Italy, May 2023. JACoW Publishing. doi: 10.18429/JACOW-IPAC2023-THPA041.